FCT
Fundação para a Ciência e a Tecnologia
MINISTÉRIO DA EDUCAÇÃO E CIÊNCIA

POPH
QUALIFICAR É CRESCER.

QREN
QUADRO DE REFERÊNCIA ESTRATÉGICO NACIONAL
PORTUGAL 2007.2013

Governo da República Portuguesa

UNIÃO EUROPEIA
Fundo Social Europeu

Optical Microsystem for Spectroscopy Signals Extraction Applied to Gastrointestinal Dysplasia Detection
Sara Filomena Ribeiro Pimenta
UMinho | 2016

Universidade do Minho
Escola de Engenharia

Sara Filomena Ribeiro Pimenta

Optical Microsystem for Spectroscopy Signals Extraction Applied to Gastrointestinal Dysplasia Detection

outubro de 2016

Universidade do Minho
Escola de Engenharia

Sara Filomena Ribeiro Pimenta

Optical Microsystem for Spectroscopy Signals Extraction Applied to Gastrointestinal Dysplasia Detection

Tese de Doutoramento em Engenharia Biomédica

Trabalho realizado sob a orientação da
Professora Doutora Graça Maria Henriques Minas
e da
Professora Doutora Elisabete M. S. Castanheira Coutinho

setembro de 2016

STATEMENT OF INTEGRITY

I hereby declare having conducted my thesis with integrity. I confirm that I have not used plagiarism or any form of falsification of results in the process of the thesis elaboration.

I further declare that I have fully acknowledged the code of ethical conduct of the University of Minho.

Universidade do Minho, 24 / 10 / 2016

Full name: Sara Filomena Ribeiro Pimenta

Signature: Sara Filomena Ribeiro Pimenta

Acknowledgements

This PhD was a long journey that has required hardwork. Finally, I can say that I am reaching my most significant professional achievement, thanks to several people that supported me during this amazing experience.

First of all, I would like to thank to my supervisors, Professor Graça Minas and Professor Elisabete Coutinho, for all the excellent support, friendship and encouragement during this work, especially in the most difficult moments. Our discussions contributed to the success of this project.

I would like to acknowledge Professor Susana Freitas, for having received me at INESC-MN and for all her guidance and advices during the optical filters fabrication and integration.

I would like to thank to Professor Paulo Mendes of the CMEMS group for all the advices given along these years and for the wirebonding of the dies.

Many thanks to all my colleagues of the CMEMS group who provided me a fantastic work environment and gave me valuable advices, during this challenging experience.

During this journey I was lucky for having the best friends in the world - Marino, Paulo, Liliana, Joana and Carla – who supported me in different situations.

Last but not least, I would like to thank my parents, Filomena and Fernando, my boyfriend, João, my brother, Luís, my sister in law, Daniela, and my little princess, my niece Maria Luís. Without their unconditional support and love I could not achieve this professional accomplishment. Thank you very much. You are the best!

The author, Sara Filomena Ribeiro Pimenta, was supported by the Portuguese Foundation for Science and Technology (in portuguese FCT – Fundação para a Ciência e a Tecnologia) with the PhD grant SFRH/BD/87605/2012.

This work is also funded by FEDER funds through the "Eixo I do Programa Operacional Fatores de Competitividade" (POFC) QREN, project reference COMPETE: FCOMP-01-0124-FEDER-020241 and by FCT, project reference PTDC/EBB-EBI/120334/2010. Finally, the author thanks to the PEst-C/FIS/UI0607/2013, UID/FIS/04650/2013, UID/EEA/04436/2013 and POCI-01-0145-FEDER-006941 for the use of equipment.

Abstract

The early detection of gastrointestinal cancer, in the dysplastic stage, is essential to increase the patient survival rate. Spectroscopic techniques, particularly diffuse reflectance and fluorescence, can improve the gastrointestinal dysplasia detection, since these techniques can be used to extract biochemical and morphologic information related with the status of a gastrointestinal tissue.

Several research groups have developed prototypes for the extraction of diffuse reflectance and fluorescence signals applied to gastrointestinal cancer detection. Despite their advantages associated with the gastrointestinal cancer identification, they have several disadvantages related with the use of complex, high-cost and sophisticate components such as xenon lamps, lasers, monochromators, optical fibers and high quantum efficiency detectors, which may hamper their wide use as well as their huge clinical value. Therefore, it is of utmost importance to develop a low-cost, miniaturized and minimal invasive microsystem for spectroscopic signals extraction.

As a result, in this work it is proposed the implementation of a microsystem, which comprises in a single chip, an optical filter system for selection and extraction of the diffuse reflectance and fluorescence signals in relevant spectral bands, a silicon photodiodes matrix (4×4) and its readout electronics, and miniaturized light emitting diodes. The main applications of this microsystem are: its use as a portable device in a surgery room for inspection of total removing of the cancerous or dysplastic tissue; and its integration with the standard endoscopes and colonoscopes using it as an auxiliary, to the physician, in early gastrointestinal cancer detection.

Along this thesis, important steps towards that microsystem implementation were achieved. In a first step experimental measurements were performed, with phantoms representative of the main absorbing, scattering and fluorescence properties of gastrointestinal tissues (containing hemoglobin, polystyrene microspheres to represent collagen fibers, and the fluorophores NADH and Carbostyril 124, the latter representing collagen), in order to study the diffuse reflectance and fluorescence typical spectra and their temperature dependence. Moreover, the viability of using only 16 spectral bands (between 350 and 750 nm) for signals extraction was discussed, proving the feasibility of an optical filter system implementation in the final microsystem.

Therefore, it were designed, fabricated and characterized 16 MgO/TiO_2 and SiO_2/TiO_2 based thin-film optical filters. Their characterization performed through optical transmittance,

selectivity, profilometry and scanning electron microscopy, allowed understanding the deviations between the simulated characteristics and the ones experimentally obtained. Moreover, the optical filters results showed transmittances ranging from 50% to 90% approximately, and a full width half maximum (FWHM) averaging from 11 nm to 20 nm, which fits the required application. The fabricated optical filters had some deviations considering their simulated characteristics, which can be explained by the complexity of the optical filters design, for example, the materials refractive index dependence with wavelength and thin-film thickness.

The diffuse reflectance and fluorescence signals that pass through the optical filters can be measured with an on-chip silicon photodetectors matrix (4×4), based on n+/p-epilayer junction photodiodes with an active area of 100 × 100 μm^2, and a light-to-frequency converter, per each photodiode, that enables producing a digital signal with a frequency proportional to the photodiode current. As a result, the design and implementation of a CMOS microsystem comprising these components were performed. The photodiodes characterization showed a responsivity of 200 mA/W at 550 nm, approximately, and the light-to-frequency converter connected to the photodiode showed a linear response (R^2>0.99) with a sensitivity of 25 Hz/nA at 550 nm, approximately. The behavior of the current-to-frequency converter, with an external current source directly injected in its input, was also studied allowing to confirm its linearity in the range of currents produced in this application, its power consumption of 1 mW, and its maximum input current, approximately 300 µA. This CMOS approach avoids the need of an expensive readout optical microsystem, since it is possible to integrate the photodiodes and the readout electronics in a small silicon area (275 × 100 μm^2 per photodiode and its respective converter).

The performance of the implemented microsystem and the fabricated optical filters was evaluated, using phantoms (also containing hemoglobin, polystyrene microspheres, NADH and Carbostyril 124). The obtained results have shown the viability of the microsystem (including the optical filter system) to extract diffuse reflectance and fluorescence signals. Some issues were noted on the sensitivity of the implemented optical setups for the on-chip measurements. However, some solutions were proposed for the remaining problems, specifically the future use of miniaturized light emitting diodes and the direct deposition of the optical filters on the top of the photodetection system. Finally, the direct integration of optical filters on top of the photodiodes was discussed and a new approach was tested.

Resumo

A deteção precoce do cancro gastrointestinal, na fase de displasia, é essencial para o aumento da taxa de sobrevivência do paciente. As técnicas de espetroscopia, particularmente a refletância difusa e a fluorescência, permitem melhorar a deteção de displasia gastrointestinal, ao poderem ser utilizadas para a extração de informação bioquímica e morfológica associada ao estado do tecido gastrointestinal.

Diversos grupos de investigação têm desenvolvido protótipos para a extração de sinais de refletância difusa e de fluorescência, para aplicação na deteção do cancro gastrointestinal. Apesar das vantagens associadas com a identificação do cancro gastrointestinal, esses sistemas apresentam várias desvantagens relacionadas com a utilização de componentes complexos, de elevado custo e sofisticados, como por exemplo, lâmpadas de xénon, lasers, monocromadores, fibras óticas e detetores de elevada eficiência, que podem dificultar a sua ampla utilização, bem como o seu elevado valor clínico. Portanto, é de extrema importância o desenvolvimento de um microssistema de baixo custo, miniaturizado e minimamente invasivo para a extração de sinais de espetroscopia.

Assim, neste trabalho é proposta a implementação de um microssistema, num único chip, compreendendo: um sistema de filtros óticos para a seleção dos sinais de refletância difusa e de fluorescência em bandas espetrais relevantes; uma matriz de fotodíodos de silício (4×4) e a respetiva eletrónica de leitura; e díodos emissores de luz miniaturizados. As principais aplicações deste microssistema são: a sua utilização como sistema portátil numa sala de cirurgia para inspeção da remoção total do tecido maligno ou displásico; ou a sua integração com os sistemas de endoscopia e colonoscopia, servindo como auxiliar de diagnóstico, na deteção precoce de cancro gastrointestinal.

Com a realização desta tese foram dados passos importantes para a implementação desse microssistema. Numa primeira fase, foram realizados testes experimentais, com um grupo de fantomas representativos das propriedades de absorção, difusão e de fluorescência dos tecidos gastrointestinais (contendo hemoglobina, microesferas de polistireno representando as fibras de colagénio, e os fluoróforos NADH e *Carbostyril* 124, este último para representar o colagénio), de forma a obter os espetros típicos de refletância difusa e de fluorescência e a influência da temperatura do fantoma nos mesmos. Para além disso, a viabilidade de usar apenas 16 bandas espetrais (entre 350 e 750 nm) para a extração dos sinais espetroscópicos foi discutida, provando a exequibilidade da implementação de um sistema de filtros óticos no microssistema final.

Assim, foram desenhados, fabricados e caracterizados 16 filtros óticos baseados em filmes finos de MgO/TiO_2 e SiO_2/TiO_2. A sua caracterização do ponto de vista da transmitância ótica, seletividade, profilometria e microscopia eletrónica de varrimento, permitiu perceber os desvios

verificados entre as características simuladas e as obtidas experimentalmente. Para além disso, os resultados da caracterização dos filtros óticos mostraram transmitâncias óticas que variam entre 50% e 90%, aproximadamente, e uma largura a meia-altura (FWHM) média entre 11 nm e 20 nm, o que é adequado para a aplicação pretendida. Os filtros óticos fabricados possuem alguns desvios das suas características simuladas, o que pode ser explicado pela complexidade no projeto de filtros óticos, por exemplo, a dependência dos índices de refração com o comprimento de onda e espessura do filme fino.

Os sinais de refletância difusa e fluorescência que atravessam os filtros óticos podem ser medidos através de uma matriz de fotodetetores de silício (4×4), baseada em fotodíodos do tipo *n+/p-epilayer* com uma área ativa de 100 × 100 μm^2, e um conversor luz-frequência, um por cada fotodíodo, que permite produzir um sinal digital com uma frequência proporcional à corrente gerada pelo fotodíodo. Assim, o projeto e a implementação de um microssistema CMOS incluindo esses componentes foram executados. A caracterização dos fotodíodos da matriz resultou num valor de responsividade de 200 mA/W a 550 nm, aproximadamente, e a do conversor luz-frequência, quando ligado a um fotodíodo, resultou numa resposta linear (R^2>0.99) com uma sensibilidade de 25 Hz/nA a 550 nm, aproximadamente. O comportamento do conversor corrente-frequência, com uma fonte de corrente externa diretamente injetada na sua entrada, foi também estudado, permitindo confirmar a sua linearidade na gama de correntes envolvidas nesta aplicação, a sua potência de consumo de 1 mW, e a sua corrente de entrada máxima, aproximadamente 300 µA. Esta abordagem em tecnologia CMOS evita a utilização de um microssistema ótico de leitura de elevado custo, uma vez que torna possível a integração dos fotodíodos e respetiva eletrónica de leitura numa área de silício pequena (275 × 100 μm^2 por fotodíodo e respetivo conversor).

Foi avaliado o desempenho do microssistema implementado e dos filtros óticos fabricados usando fantomas (mais uma vez contendo hemoglobina, microesferas de polistireno, NADH e *Carbostyril* 124). Os resultados obtidos provaram a viabilidade do microssistema (incluindo o sistema de filtros óticos) para a extração de sinais de refletância difusa e de fluorescência. Foram notados alguns problemas na sensibilidade dos *setups* óticos implementados para as medições *on-chip*. No entanto, foram também propostas algumas soluções para os respetivos problemas, especificamente o uso futuro de díodos emissores de luz miniaturizados e a deposição direta dos filtros óticos no sistema de fotodeteção. Finalmente, a integração dos filtros óticos depositados diretamente em cima dos fotodíodos foi discutida e uma nova abordagem foi testada.

Index

Index of Figures

Index of Tables

List of Symbols

Symbol	Description	Unit
μ_a	Absorption coefficient	m^{-1}
ρ_r	Amplitude reflection coefficient	-
ω	Angular frequency	$rad.s^{-1}$
g	Anisotropy factor	-
C_{MOS}	Capacitor capacitance	F
t_{MOS}	Capacitor charging time	s
L	Capacitor gate length	m
W	Capacitor gate width	m
C_i	Concentration of the main absorber molecule	$mol.\ L^{-1}$
ΔV_{MOS}	Difference between the highest and lowest potential in the capacitor	V
ρ	Electric charge density	$C.m^{-3}$
σ	Electric conductivity	$S.m^{-1}$
$\vec{J}$	Electric current density vector	$A.m^{-2}$
$\vec{D}$	Electric displacement vector	$C.m^{-2}$
$\vec{E}$	Electric field vector	$V.m^{-1}$
q_e	Electron charge	C
ΔEC	Energy stored in the capacitor	J
$\lambda_{excitation}$	Excitation wavelength	m
τ_F	Excited-state lifetime	s
k	Extinction coefficient	$m^2.kg^{-1}$
ε_i	Extinction coefficient of the main absorber molecule	$m^{-1}/mol.L^{-1}$
Φ_F	Fluorescence quantum yield	-
f	Frequency	Hz
HH	Half-wave layer with high refractive index	-

Symbol	Description	Unit
LL	Half-wave layer with low refractive index	-
q	Interference order of the *Fabry-Perot* interferometer	-
θ	Light incidence angle	rad
$\vec{H}$	Magnetic field vector	$A.m^{-1}$
$\vec{B}$	Magnetic induction vector	T
μ	Magnetic permeability of the medium	$H.m^{-1}$
Y	Optical admittance	S
OPL	Optical path length	m
OP	Optical power	W
C_p	Parasitic capacitance	F
$d_{silicon}$	Penetration depth of light in silicon	m
μ_0	Permeability of the free space	$H.m^{-1}$
ε_0	Permittivity of the free space	$F.m^{-1}$
ε	Permittivity of the medium	$F.m^{-1}$
ε_{0x}	Permittivity of the silicon dioxide	$F.m^{-1}$
ϕ	Phase of the wave	rad
δ	Phase thickness	rad
C_s	Photodiode capacitance	F
I	Photodiode current	A
R_{p1}	Photodiode resistance	Ω
d_t	Physical thickness of the quarter-wave layers (mirrors)	m
d_s	Physical thickness of the resonance cavity	m
d	Physical thickness of the thin-film	m
h	Planck constant	J.s
C_{0x}	PMOS gate capacitance per square meter	$F.m^{-2}$
$\vec{r}$	Position vector	m
η	Quantum efficiency	-
H	Quarter-wave layer with high refractive index	-

Symbol	Description	Unit
L	Quarter-wave layer with low refractive index	-
μ_s'	Reduced scattering coefficient	m^{-1}
R	Reflectance	-
n	Refractive index	-
n_t	Refractive index of the quarter-wave layer	-
n_s	Refractive index of the resonance cavity	-
n_m	Refractive index of the substrate	-
R_{Ph}	Responsivity	$A.W^{-1}$
μ_s	Scattering coefficient	m^{-1}
$\alpha_{silicon}$	Silicon absorption coefficient	m^{-1}
ρ_s	*Spearman's* correlation coefficient	-
c	Speed of light in free space	$m.s^{-1}$
t_{Ox}	Thickness of the gate oxide layer	m
t	time	s
T	Transmittance	-
v	Velocity of light in a medium	$m.s^{-1}$
$V(t_{MOS})$	Voltage in the capacitor gate	V
$\vec{k}$	Wave vector	$rad.m^{-1}$
λ	Wavelength	m
R_{p2}	Wire resistance from the photodiode to the St connection	Ω

List of Terms

Term	Designation
ADC	Adenocarcinoma
AC	Alternating current
BE	Barrett's esophagus
CCD	Charge couple device
CMOS	Complementary metal oxide semiconductor
IF	Current-to-frequency
DRS	Diffuse reflectance spectroscopy
DWL	Direct write laser
EDS	Energy-dispersive X-ray spectroscopy
FFD	Flip flop D
FRET	Fluorescence resonance energy transfer
FWHM	Full width half maximum
GI	Gastrointestinal
HMDS	Hexamethyldisilazane
IBD	Ion beam deposition
IPA	Isopropyl alcohol
LED	Light emitting diode
LF	Light-to-frequency
LDA	Linear discriminate analysis
NBI	Narrow-band imaging
NA	Numerical aperture
PMT	Photomultiplier tubes
PR	Photoresist
PCA	Principal component analysis
RF	Radio frequency
NADH	Reduced form of nicotinamide adenine dinucleotide
SEM	Scanning electron microscopy
St	Schmitt trigger

Term	Designation
SCC	Squamous-cell carcinoma
TPEF	Two-photon excitation fluorescence
UV	Ultraviolet
WHO	World health organization

1 Introduction

In this chapter, the global incidence of GI (gastrointestinal) cancer is discussed. The anatomy and functionality of GI tract and the changes that occur during cancer progression are described. Moreover, the most relevant studies performed in the last decades focusing the detection of GI cancers using spectroscopy signals measurements are presented. Finally, the motivation and the main objectives of this thesis are detailed, as well as the overall organization of this document.

1.1 Gastrointestinal cancer: global incidence

Cancer is referred as one of the main causes of death in the world, with approximately 8.2 million deaths in 2012, including the GI cancers (1817000 deaths), specifically stomach, colorectal and esophageal cancers [1, 2].

According to the WHO (world health organization), a cancer is a fast creation of abnormal cells that can invade adjacent parts of the body and spread to other organs. It is a multistage process, which begins as a pre-cancerous lesion and arises to a malignant tumor. The process is the result of the interaction between a person's genetic factors and three external agents: physical carcinogens (for example, UV (ultraviolet) and ionizing radiation); chemical carcinogens (such as components of tobacco smoke, food and water contaminants); and biological carcinogens (such as infections from viruses, bacteria or parasites) [1].

Table 1.1 to Table 1.3 represent the estimated incidence and mortality for three types of GI cancers in the world and in the European Union, in 2012 [3].

Table 1.1 Estimated numbers for the incidence (cases) and mortality (deaths) for stomach cancer in the world and in the European Union, in 2012 [3].

Stomach cancer			
World		European Union	
Cases	Deaths	Cases	Deaths
952	723	82	58

Estimated numbers (thousands).

Table 1.2 Estimated numbers for the incidence (cases) and mortality (deaths) for colorectal cancer in the world and in the European Union, in 2012 [3].

Colorectal cancer			
World		European Union	
Cases	Deaths	Cases	Deaths
1361	694	345	152

Estimated numbers (thousands).

Table 1.3 Estimated numbers for the incidence (cases) and mortality (deaths) for esophageal cancer in the world and in the European Union, in 2012 [3].

Esophageal cancer			
World		European Union	
Cases	Deaths	Cases	Deaths
456	400	35	30

Estimated numbers (thousands).

The incidence of stomach cancer varies around the world. More than 70% of the cases are in the developing countries and 50% of the world total cases are identified in Eastern Asia (especially in China). Concerning its mortality, the highest mortality rates are registered in Eastern Asia and the lowest are in Northern America. Moreover, high mortality rates also occur in Central and Eastern Europe and in Central and South America. It is also important to note that the worldwide incidence of the stomach cancer has been declining over the few decades. This may be due to the recognition of some risk factors, such as *Helicobacter Pylori* infection and some dietary and environmental risks [3, 4].

Colorectal cancer incidence also varies across the world. It is the third most common cancer in men and the second in women. The highest incidence rate is in Australia and New Zealand and the lowest in Western Africa. Regarding its mortality, the highest rate is registered in the Central and Eastern Europe and the lowest in Western Africa. Risk factors for the colorectal cancers include: low socioeconomic status (which can influence the colorectal cancer screening),

physical inactivity, unhealthy diet, smoking, obesity, tobacco, alcohol, family history of colorectal cancer and adenomatous polyps and personal history of inflammatory bowel disease [3, 5].

Concerning the esophageal cancers, around 80% of the cases in the world occur in less developed regions and the incidence rate in men are 2 times higher than in women. Esophageal cancer has a low survival rate and its mortality rates follow its geographical pattern for incidence. The highest mortality rates are in Eastern Asia and Southern Africa for men and in Eastern and Southern Africa for women. Usually, esophageal cancers occur in one of two different ways: SCC (squamous-cell carcinoma) arising from the stratified squamous epithelium that lines the esophagus; and ADC (adenocarcinoma) arising from columnar glandular cells that replace the squamous epithelium in the esophagus. Three decades ago, the majority of the esophageal cancers were SCCs. However, the incidence of the ADCs has been increasing. Regarding the main risk factors, tobacco, alcohol, red meat, opium consumption, hot tea drinking, poor oral health, low intake of fresh fruit and vegetables and low socioeconomic status are associated with a higher risk of SCC. On the other hand, obesity, reflux symptoms and BE (barrett's esophagus[1]) are recognized as risk factors for ADC [3, 6].

In Portugal, the most common GI cancer is the colorectal cancer (which is also the third most incident type of cancer), followed by the stomach and esophageal cancers. Table 1.4 to Table 1.6 represent the estimated incidence and mortality for these three types of GI cancers in Portugal, in 2012. It is also important to note that the esophageal cancer has the highest mortality rate, since approximately 89% of the patients with esophageal cancer die from this disease. The same happens taking into account the world and European Union incidences and mortalities (Table 1.1 to Table 1.3) [7].

Table 1.4 Estimated numbers for the incidence (cases) and mortality (deaths) for colorectal cancer in Portugal, in 2012 [7].

Colorectal cancer	
Cases	Deaths
7129	3797

[1] The barrett's esophagus is a condition that is characterized by the presence of metaplastic columnar epithelium in the esophagus replacing the stratified squamous epithelium. People with barrett's esophagus have a higher probability of developing esophagus cancer [6, 18].

Table 1.5 Estimated numbers for the incidence (cases) and mortality (deaths) for stomach cancer in Portugal, in 2012 [7].

Stomach cancer	
Cases	Deaths
3018	2285

Table 1.6 Estimated numbers for the incidence (cases) and mortality (deaths) for esophageal cancer in Portugal, in 2012 [7].

Esophageal cancer	
Cases	Deaths
608	540

Therefore, the cancer early detection is really important, since it gives to the patient a higher effective treatment chance, increasing the survival rate [8]. This is especially significant for the esophageal cancer, since it presents the highest mortality rate. A lot of efforts have been made to improve the diagnostic capabilities and this work is also an attempt to improve the GI cancer early detection.

1.2 Gastrointestinal tract: anatomy, functionality and cancer progression

The GI tract is a highly specialized organ system that acts as an interface between the body and the external environment [9]. In the GI tract, the food consumed by humans is converted to compounds (nutrients, water and electrolytes) that are absorbed into the body internal environment [9, 10]. Moreover, the GI tract has also the function of metabolizing and eliminating the non-nutrient and toxic compounds [9].

The organs included in the GI tract are the mouth, esophagus, stomach, small intestine and large intestine [9, 10] - Figure 1.1 . Moreover, the pancreas and the liver secrete into the small intestine [9]. Finally, the GI system is connected to the vascular, lymphatic and nervous systems

in order to facilitate the regulation of the digestive response, the delivery of compounds to the body organs and the regulation of food intake [9].

Epithelium or epithelial tissue lines the interior of the GI tract [12]. The epithelial tissue consists of closely packed sheets with a single or multiple layers of cells with important functions, such as: protection, sensory reception, and the secretion, absorption and transport of bioactive molecules [12, 13]. The epithelium is separated from the underlying connective tissue by the basement membrane [12, 13]. The connective tissue consists of structural proteins (for example, collagen and elastin), cells (such as fibroblasts and white blood cells) and blood vessels [13].

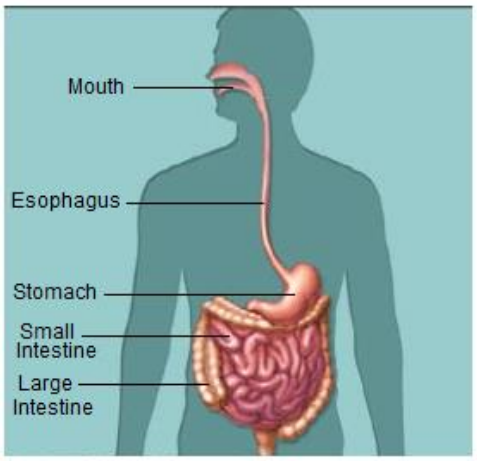

Figure 1.1 Representation of the GI tract organs (adapted from [11]).

The epithelial tissue is classified based on the cell shape and number of cell layers. A sheet that contains only one layer of cells is named simple epithelium. With two or more cells layers is called stratified epithelium. Both can be classified in squamous, cuboidal and columnar, according to the shape of cells comprising the simple and stratified epithelium. Finally, there is the pseudostratified epithelium and the transitional epithelium. In the first, there is only one layer of cells but with different heights, which gives the impression of a stratified epithelium. In the second one, the cells undergo a transition on shape, depending on the epithelium is distended or relaxed. As a result, there are eight categories of epithelia: simple squamous; simple cuboidal; simple columnar; stratified squamous; stratified cuboidal; stratified columnar; pseudostratified columnar; and transitional epithelium [12].

Concerning the type of epithelium that lines the surface of the GI tract, in the mouth and esophagus it is the stratified squamous epithelium; in the stomach, small intestine and large intestine it is the simple columnar epithelium [12].

In general, the wall of GI tract consists of four layers of cells: mucosa, submucosa, and muscularis propria. As an example, Figure 1.2 presents the structure organization of the esophageal wall [14].

The mucosa is arranged in longitudinal folds that disappear upon distention. It consists of three sublayers: epithelial layer; lamina propria (a thin layer of connective tissue); and muscularis mucosa (a thin layer of longitudinally, irregularly arranged smooth muscle fibers). The submucosa contains connective tissue as well as lymphocytes, plasma cells, nerve cells, vascular network and mucous glands (whose secretion is important in tissue resistance to acid). Finally, the muscularis propria is made of muscle layers with different orientations (such as circular and longitudinal orientations) and is responsible for motor function [14, 15].

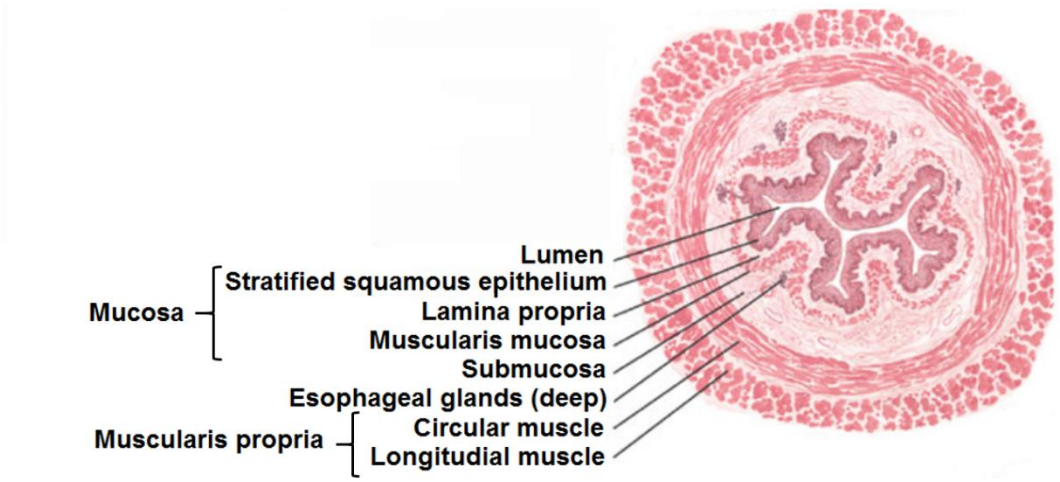

Figure 1.2 Structure organization of the esophageal wall (adapted from [14]).

A group of cells that escape the normal controls of growth and division can originate a neoplasm or tumor. If the growth does not spread, it is a benign tumor. Contrarily, if it spreads to other regions or metastasizes, it is called a malignant tumor or cancer [12]. Most common cancers begin in the epithelium [13]. When a malignant tumor is derived from epithelium, it is named carcinoma. If the carcinoma is derived from columnar glandular epithelium is named ADC and if it is derived from the stratified squamous epithelium it is named SCC [6, 12].

Figure 1.3 shows a white-light endoscopic image of a macroscopically invisible esophageal SCC (A) except for a slight reddish discoloration of the mucosa in the distal part of the esophagus, and it exposure to a violet-blue excitation light for fluorescence spectroscopy (B) [16]. The use of spectroscopy for GI cancer detection and its importance will be explored on the next section (section 1.3).

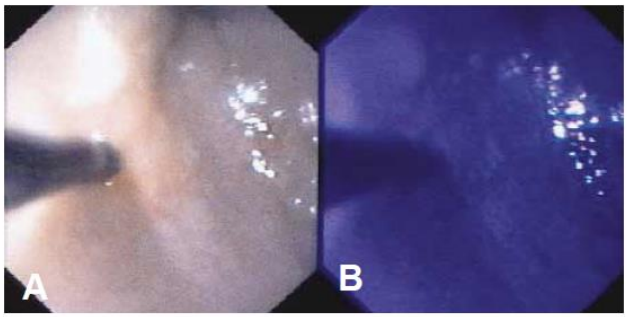

Figure 1.3 White-light endoscopic image of a SCC (A) and its exposure to violet-blue light (B), (reprinted from [16] with permission from Elsevier).

Figure 1.4 shows a BE lesion with suspicious dysplastic areas, at the nine o'clock position. As it can be seen, it is hard to detect the dysplastic lesions in the BE lesion with high-resolution endoscopy [17].

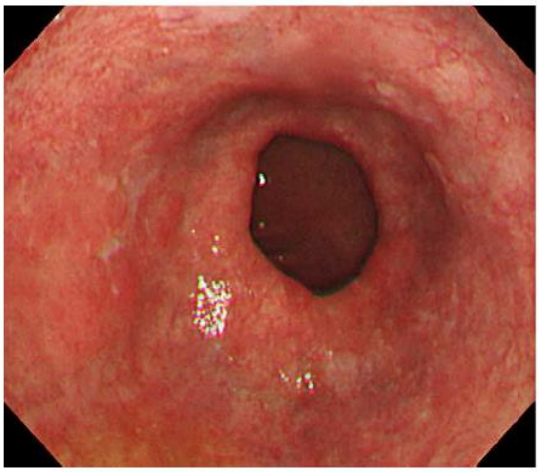

Figure 1.4 BE imaged with high-resolution endoscopy (adapted from [17] with permission from Elsevier).

The transformation of a normal epithelium in a cancerous lesion involves a group of gradual changes. In an initial stage, the level of expression of certain proteins is altered, followed by an increase in the epithelium thickness (hyperplasia) and changes in the morphology and organization

of cells, which extent throughout the epithelial layer. If the changes are only in the epithelial layer, the lesions are classified as dysplastic or pre-cancerous. Cancer appears when the underlying tissues are affected, i. e., the basement membrane is compromised and the transformed cells invade the connective tissue and can enter on the circulatory and lymphatic systems and metastasize to other organs [2, 13].

1.3 Optical spectroscopy for gastrointestinal cancer detection: state of the art

GI cancer detection in an early stage, i.e., in the dysplastic or pre-cancerous stage, is fundamental once it gives to the patient a higher effective treatment chance, increasing the survival rate [8, 13, 18]. However, GI dysplasia is difficult to detect taking into account the conventional visual inspection techniques (endoscopy and colonoscopy), due to the lack of gross morphological easily visible changes on the tissue in the early stage of cancer [2, 8, 13, 19, 20].

As a result, when a cancer suspicion appears, a biopsy or several ones are performed, in order to increase the detection probability of the invisible lesions [13]. Biopsies are invasive procedures that suffer from undersampling and their results are not immediately available, resulting on a delay of patient's treatment [8]. For all these reasons, it is increasingly important to develop new and minimally invasive techniques to guide physicians to the biopsy sites that are highly probable to be abnormal, or to eventually replace biopsies and detect early stages of GI cancers [2, 13, 19].

Optical spectroscopies, including diffuse reflectance and fluorescence spectroscopy, can overcome the limitations in the early detection of GI cancers, since they have exquisite sensitivity to some cancer biomarkers present on the tissues and they can detect the earliest change on the tissue at the morphological and biochemical level [8, 13, 18, 20, 21]. As a result, small changes in those biomarkers concentration or in the tissue morphology, due to the dysplasia progression, will affect the diffuse reflectance and fluorescence spectra signals of the malignant tissue. In order words, the spectroscopy signals shape and intensity will be different when compared with the signals from a normal tissue [2, 19, 22]. Figure 1.5 shows some stated results on the literature for the diffuse reflectance (A) and fluorescence (B) signals of different tissues.

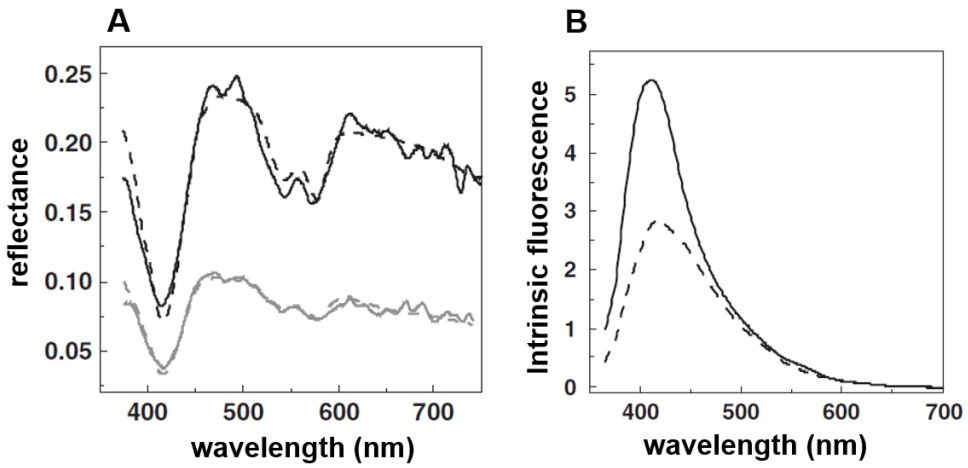

Figure 1.5 Diffuse reflectance signal (A) and intrinsic fluorescence signal (B) of different tissues. In (A) the higher intensity lines (in black) correspond to a reflectance spectrum of a non-dysplastic BE tissue site; the low intensity lines (in gray) correspond to a low-grade dysplastic BE tissue site. In (B) the solid lines correspond to a non-dysplastic BE tissue site and the dashed lines correspond to a high-grade dysplastic BE tissue site (adapted from [13] with permission from Elsevier).

In the next paragraphs, a brief description of the most relevant studies in the last decades, about the development of prototypes for spectroscopy signals extraction and characterization of GI tissues, will be presented.

Georgakoudi *et al.* [18] performed a study to assess the potential of fluorescence and reflectance signals for evaluating low- and high-grade dysplasia in patients with BE. The signals extraction was performed *in-vivo* during endoscopy and before biopsy to the same site at which the spectra were measured. For that purpose, the authors used a complex spectroscopic system based on a white light from a Xe (xenon) flash lamp for the reflectance measurements, a 337 nm N_2 (nitrogen) laser for the fluorescence measurements and an optical fiber probe (inserted into the accessory channel of the endoscope) – Figure 1.6. The signals were collected (between 350 and 750 nm) by the probe and coupled to a spectrograph and detector. The spectroscopic signals analysis, and their treatment with mathematical models, provided information about the biochemical and morphological changes that occur on the tissues during dysplasia progression, leading to distinguish the nondysplastic BE from the dysplastic BE (low-grade and high-grade) with a sensitivity of 79% and specificity of 88%. The authors showed different types of information that can be acquired by treating the extracted signals and the way this information can be used to assist a physician in classifying a particular tissue area. Moreover, the accuracy of these spectroscopy

techniques was proven since it was possible to distinguish not only high-grade but also low-grade dysplastic changes.

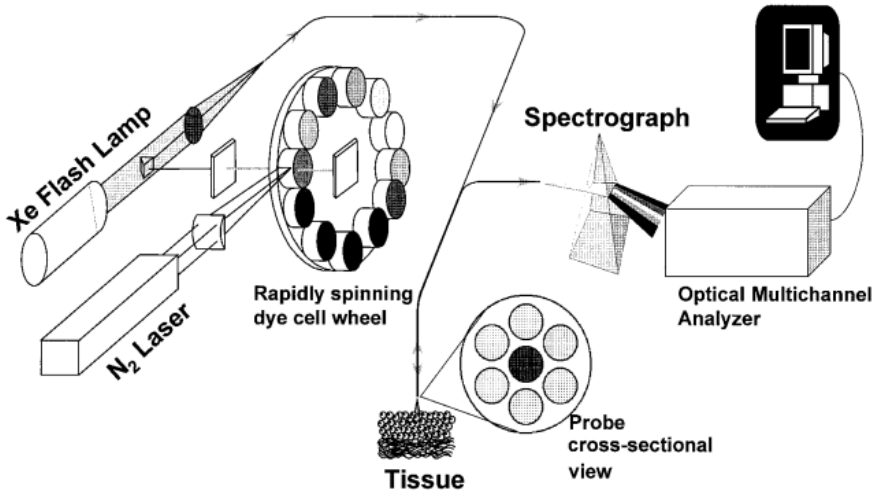

Figure 1.6 Spectroscopic system used by Georgakoudi *et al.* [18] for spectroscopy signals extraction. The optical probe was composed by 6 collection fibers surrounding a central light delivery fiber (reprinted from [18] with permission from Elsevier).

Tunnell *et al.* [23] developed an opto-mechanical system (Figure 1.7) to collect the white light reflectance and fluorescence spectra within a fraction of a second. The system was controlled by a computer with a custom software interface, making possible the real-time data analysis and diagnosis. The authors used a complex spectroscopic system based on a Xe flash lamp, a set of lasers and an optical fiber probe for light deliver and collection (that was small enough to be introduced into the accessory channel of an endoscope). The signals were collected by the probe and coupled to a spectrograph with an intensified CCD (charge couple device) detector. The short acquisition time was achieved using a set of rotation wheels driven by an AC (alternating current) motor. The authors evaluated the system performance collecting reflectance spectra (between 300 and 800 nm) from a set of tissue phantoms with well defined optical properties. Moreover, they collected fluorescence signals from a mixture of biochemicals (excitation between 300 and 500 nm and emission between 300 and 800 nm). The authors concluded that the system accurately acquires reflectance and fluorescence spectra (based on the known features of the used phantoms and mixtures of biochemicals) within a fraction of a second which is an acceptable time frame for clinical use. The authors also referred that in the future they can refine spectral analysis algorithms and implement diagnostic algorithms providing an instant feedback (to the physician) about the state of a tissue (normal, low-grade dysplasia, high-grade dysplasia or cancerous).

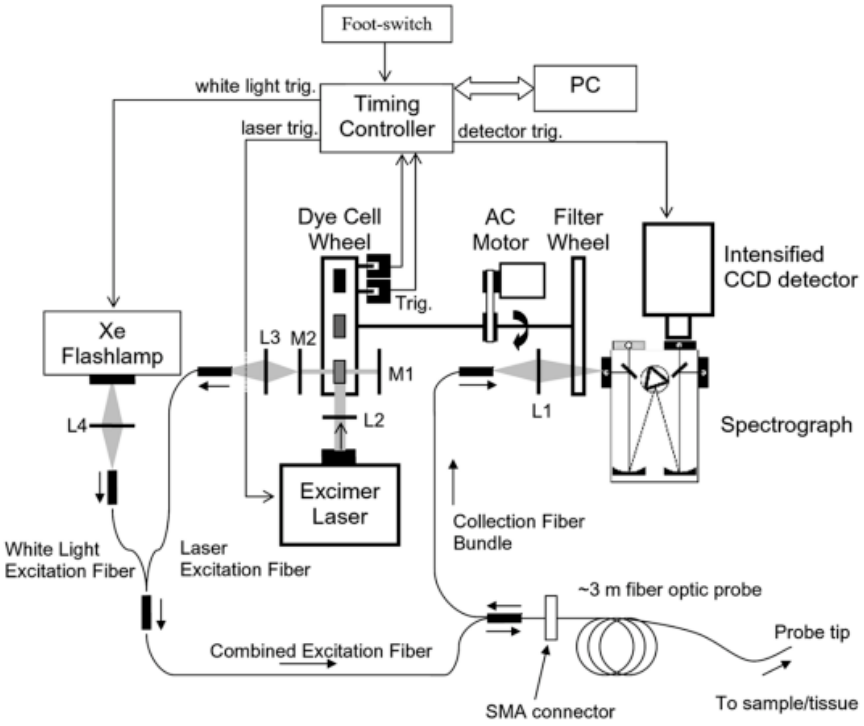

Figure 1.7 Opto-mechanical system used by Tunnell *et al.* [23] for spectroscopic signals extraction; trig. (trigger); SMA (SubMiniature version A); L (lenses); M (mirrors), (reprinted from [23] with permission from SAGE Ltd).

Mayinger *et al.* [24] performed a study to assess the potential of fluorescence spectroscopy, using violet-blue light excitation energy, for the *in-vivo* differentiation of normal, dysplastic adenomas and cancerous colorectal tissue, during colonoscopic examination and biopsy. The fluorescence extraction (between 450 and 750 nm) was performed using a system (Figure 1.8) based on a 300 W short-arc Xe lamp with a special switching bandpass filter (375 - 478 nm) for the light-induced fluorescence (the violet-blue emission light was fed directly into the light cable of the flexible endoscope), an optical fiber probe to extract the fluorescence emission spectra (passed down the biopsy channel of the mucosa colonoscope) and a spectrograph. The spectra were transferred to a computer for further processing. A biopsy was performed at the same site of the fluorescence collection. The authors developed an algorithm for the fluorescence spectral analysis based on the ratio of the fluorescence intensity in two spectral regions, green and red. This algorithm allowed the diagnosis of colorectal cancer with a sensitivity of 96% and a specificity of 93% and the diagnosis of dysplastic adenomas with a sensitivity of 98% and a specificity of 89%.

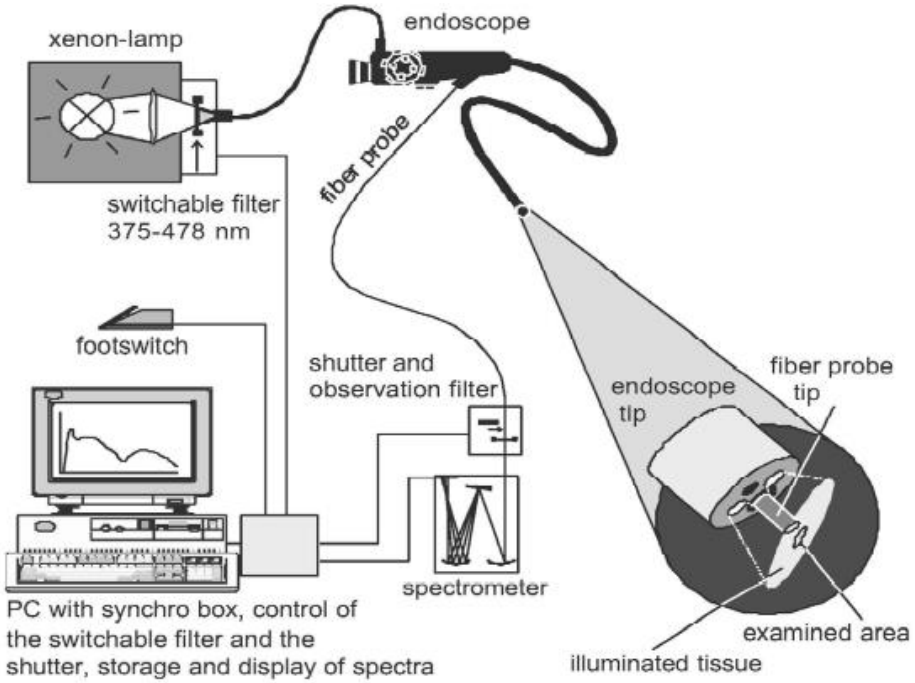

Figure 1.8 Spectroscopic system used by Mayinger *et al.* [24] for fluorescence signal extraction (reprinted from [24] with permission from Elsevier).

Lovat *et al.* [25] performed a study to assess the potential of the elastic scattering spectroscopy (also known as diffuse reflectance spectroscopy) to detect high-grade dysplasia or cancer in patients with BE. The diffuse reflectance spectroscopy measurements were performed *in-vivo,* during routine endoscopy and biopsy at the same tissue site, and using a system based on a pulsed Xe arc lamp, two optical fibers for light delivery and collection (passed into the esophagus via the biopsy channel of an endoscope), a spectrometer and a computer to control these components and record the spectra – Figure 1.9. The extracted diffuse reflectance spectra were treated statistically (between 370 and 890 nm), leading to differentiate low risk sites (normal and low grade dysplasia) from high risk sites (high grade dysplasia and cancer) with a sensitivity of 92% and a specificity of 60%. The authors also concluded that if the measurement of diffuse reflectance spectra was used to target biopsies during endoscopy, the number of low risk biopsies taken will decrease 60% with minimal loss of accuracy.

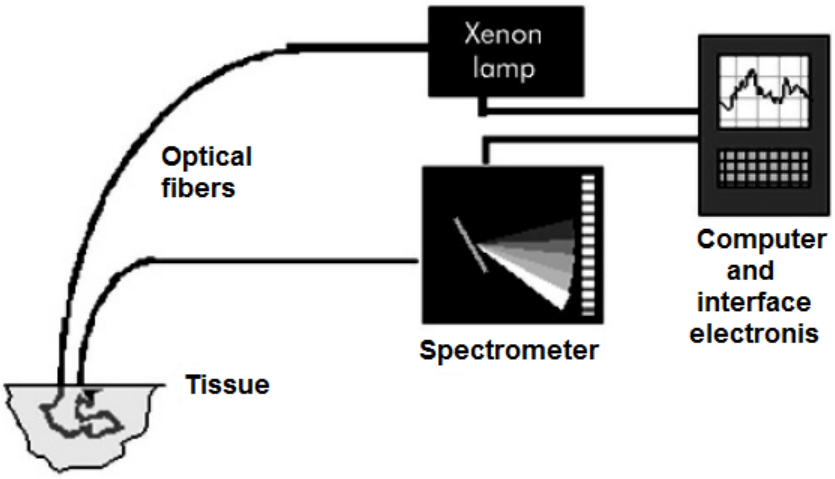

Figure 1.9 Spectroscopic system used by Lovat *et al.* [25] for diffuse reflectance measurements (reprinted from [25] with permission from BMJ publishing group Ltd).

Dhar *et al.* [26] performed a study to assess the diagnostic potential of the elastic scattering spectroscopy in the colon, to differentiate normal mucosa from benign and malignant pathologies, specifically, to differentiate normal colonic mucosa, chronic colitis, hyperplastic polyps, adenomatous polyps (with dysplasia) and ADC. The spectra were measured *in-vivo* (between 300 and 800 nm) during colonoscopy and biopsy at the same site, using a system based on a pulsed Xe arc lamp, a spectrometer, two optical fibers (one for transmitting and another to receiving the light, passed down the biopsy channel of the colonoscope) and a computer for spectral analysis - Figure 1.10. The diffuse reflectance spectra were compared, based on attributes such as light intensity ratios at various wavelengths, by using statistical computational analysis methods, specifically PCA (principal component analysis) and LDA (linear discriminate analysis). These analyses allow to differentiate the normal mucosa from all pathologies with a sensitivity of 92% and a specificity of 82%. Moreover, the authors could differentiate the different pathologies between them with high sensitivities and specificities.

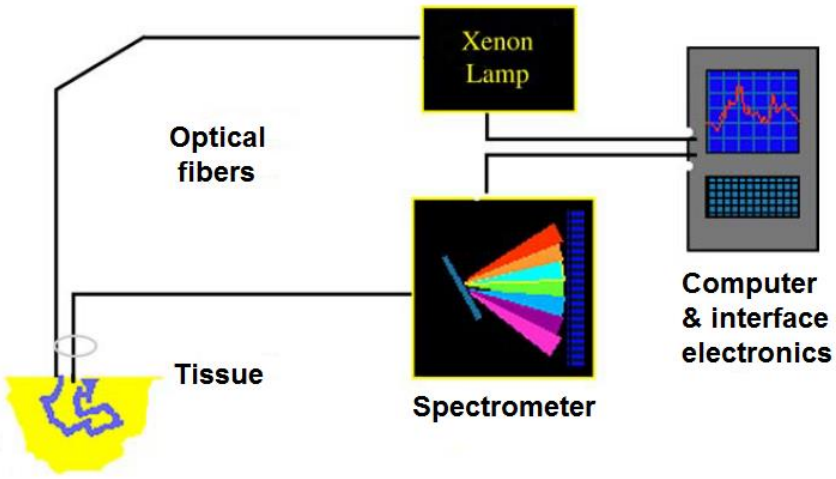

Figure 1.10 Spectroscopic system used by Dhar *et al.* [26] for diffuse reflectance measurements (adapted from [26] with permission from Elsevier).

Bing Yu *et al.* [27] developed a hybrid optical system to quantify the absorption and scattering coefficients of phantoms based on the measurement of diffuse reflectance spectra (between 400 and 600 nm). The optical system was based in a 450 W Xe lamp, a monochromator, an optical fiber for illumination, a silicon photodiode with a low-noise current amplifier and a computer for spectra analysis - Figure 1.11. The main advantage of using a photodiode was the improvement of light collection efficiency because of the larger NA (numerical aperture) of the silicon photodiode and its direct contact with the sample. Moreover, the use of the photodiode and current amplifier replaced the collection fibers, spectrographs and sophisticated detectors with high sensitivity (such as a CCD detector), reducing the system final cost. In order to evaluate the system performance, the authors performed diffuse reflectance measurements with homogeneous tissue phantoms (mixtures of an absorber [hemoglobin] and a scatterer [1 μm polystyrene spheres]). The authors used an inverse Monte Carlo model to accurately extract the absorption and reduced scattering coefficients, for each phantom, based on the measured diffuse reflectance spectra. The authors also concluded that this hybrid optical device can be expanded into a quantitative spectral system for mapping tissue optical properties and that there is a large number of applications for which this technology can be suited, such as epithelial precancer and cancer detection.

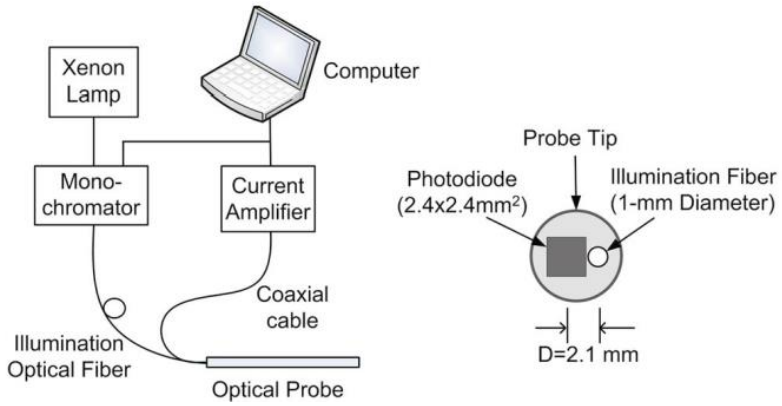

Figure 1.11 Hybrid optical system developed by Bing Yu *et al.* [27] for absorption and scattering coefficients quantification in phantoms (reprinted from [27] with permission from SPIE publications).

Chung-Chieh Yu *et al.* [8] developed a quantitative spectroscopic imaging system for wide area detection of early cancer, by acquiring diffuse reflectance and fluorescence signals. The use of diffuse reflectance and fluorescence signals, in combination, allowed extracting quantitative information about morphological and biochemical tissue constituents. The developed system was divided in 4 modules: module 1 was the light source module, based on a 75 W white light arc lamp and a 337 nm nitrogen laser; module 2 was based on a spectrograph/CCD unit; module 3 was a computer for data acquisition control and data analysis; and module 4 was the optical head comprising optical fibers for light illumination and collection and a 2D scanning mirror, achieving wide area coverage - Figure 1.12. At each mirror position, a reflectance and a fluorescence measurement was performed. The authors conducted experiments with phantoms in order to determine the optimal working distance (22.5 cm, in Figure 1.12). Moreover, for calibrating the system and establish its accuracy, the authors performed diffuse reflectance and fluorescence measurements (between 387 and 707 nm) with phantoms (mixtures of an absorber [hemoglobin], a scatterer [intralipid] and a fluorophore representative of collagen emission [the dye furan 2]). The diffuse reflectance signal of each phantom and for each particular position was analyzed with a stated model (analytical light diffusion model) to extract the absorption and reduced scattering coefficients. These coefficients were used with the respective fluorescence signal (also in a stated model) to extract the intrinsic fluorescence of each phantom at a particular position (fluorescence only due to the fluorophore, without absorption and scattering distortions). In addition, the authors performed *ex-vivo* measurements with a colon cancer specimen demonstrating the ability of the optical system to diagnose malignant lesions, established by the development of an algorithm based on the statistical analysis of spectral parameters, to distinguish normal and cancer tissue

sites. Finally, the authors demonstrated the clinical applicability of the system presenting *in-vivo* spectral characterization of a hyperkeratotic (hyperplastic) lesion on the ventral tongue of a patient. Different diffuse reflectance and fluorescence parameters were acquired and noted between the hyperkeratotic region and the surrounding normal mucosa. The authors concluded that the developed system was able to provide spectral contrasts (based on tissue parameters) and it was designed for openly accessible sites, such as the oral cavity.

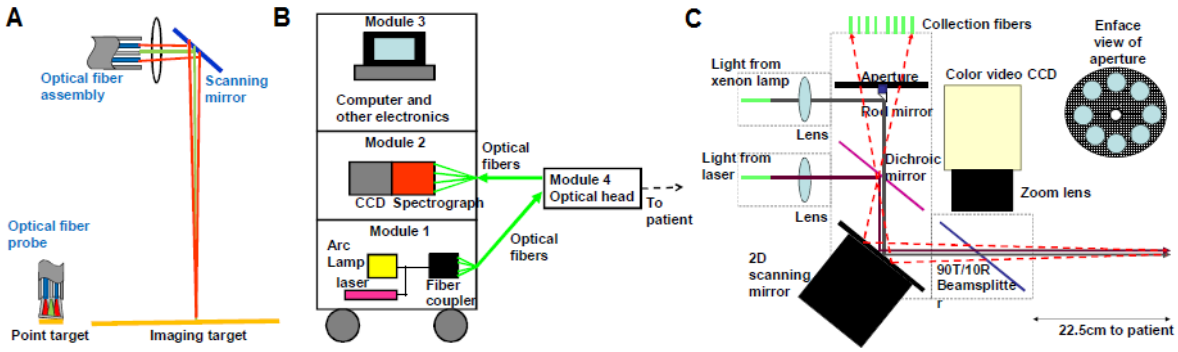

Figure 1.12 Quantitative spectroscopic imaging system developed by Chung-Chieh Yu *et al.* [8] for diffuse reflectance and fluorescence measurements: (A) instrumentation principle, green beams are illumination and red beams are collection; (B) block diagram of the system; (C) schematic diagram of the optical head (reprinted from [8] with permission from OSA).

Lo *et al.* [28] designed and validated a system for absorption and scattering coefficients quantification of tissue phantoms. The system was based on the use of a 450 W Xe lamp, a monochromator, an illumination optical fiber, a commercial silicone photodiode for signals detection, replacing the costly detection equipment usually used (such as a CCD detector), a current amplifier and a computer - Figure 1.13. A hole was done at the center of photodiode for the illumination fiber, minimizing the separation between illumination and detection areas and maximizing the light collection efficiency. The implemented system was used to extract diffuse reflectance signals from tissue phantoms (mixtures of an absorber [hemoglobin] and a scatterer [1 µm polystyrene spheres]) between 400 and 600 nm. The signals were treated with an inverse Monte Carlo model in order to extract the absorption and scattering coefficients. The results showed the system good performance in extracting optical properties of tissue phantoms. Moreover, the authors investigated the potential of replacing the Xe lamp and monochromator by five commercially available LEDs (light emitting diodes) in the 400-600 nm spectral range. Despite this great advance for the system miniaturization and low cost, the authors only proved the good

performance of the LEDs and photodiode to extract information about phantoms absorption and scattering properties, since only the diffuse reflectance signal was extracted.

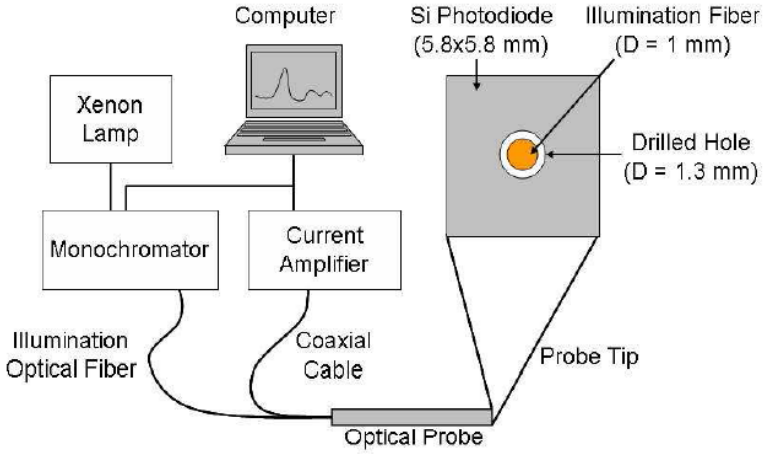

Figure 1.13 Optical system implemented by Lo *et al.* [28] for diffuse reflectance signal extraction (reprinted from [28] with permission of OSA).

Mallia *et al.* [29] performed a clinical study to evaluate the potential of fluorescence and diffuse reflectance signals extraction for the differentiation of various tissue types in the oral cavity, such as normal, hyperplastic/hyperkeratotic (benign), dysplastic and different stages of SCCs. For the spectroscopy measurements, the authors used a system based on a diode laser and a tungsten halogen lamp, for fluorescence and for diffuse reflectance measurements, respectively; an optical fiber probe that delivers the light to the oral tissue and collect the spectroscopy signals; a spectrometer; and a laptop computer - Figure 1.14. The spectrophotometric measurements were taken *in-vivo* (between 420 and 720 nm) from a group of volunteers and biopsies or visual inspection were performed from the same sites of the measurements. The fluorescence and diffuse reflectance signals were used to extract the intrinsic fluorescence signals. After that, the intrinsic fluorescence signals were fitted using Gaussian spectral functions, in order to determine constituent emission peaks. The Gaussian peak intensities and area ratios at 500, 635 and 685 nm were used to discerning different tissue types with high sensitivities and specificities.

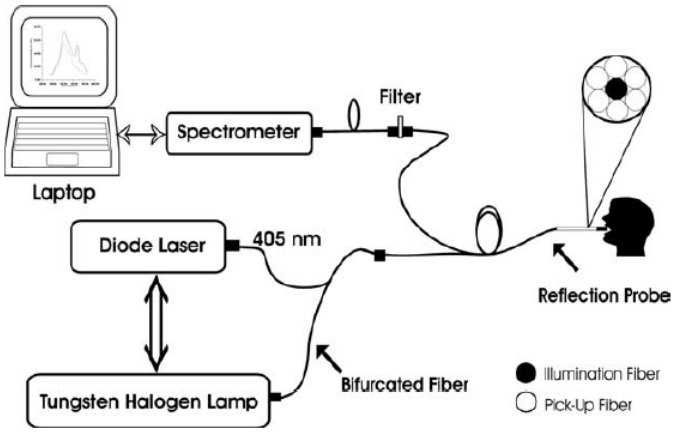

Figure 1.14 Optical system used by Mallia *et al.* [29] for spectroscopy signals extraction (reprinted from [29] with permission from John Wiley and Sons).

Jayanthi *et al.* [30] performed a study to access the potential of fluorescence and diffuse reflectance spectroscopies in the noninvasive detection of oral cavity cancer. For the *in-vivo* measurements, the authors used a system similar to the one used by Mallia *et al.* [29], that consists in two light sources (a tungsten-halogen lamp to record the diffuse reflectance spectra and a 404 nm diode laser for the fluorescence measurements), an optical probe for light deliver and collection, a spectrometer and a laptop computer - Figure 1.15. The spectra were recorded between 420 nm and 720 nm. The data was analyzed using PCA and LDA, leading to distinguish different oral cavity lesions from normal tissues, with high sensitivities and specificities. The effectiveness of the diffuse reflectance and fluorescence techniques was accessed by comparison with gold standard techniques, biopsies and visual inspection.

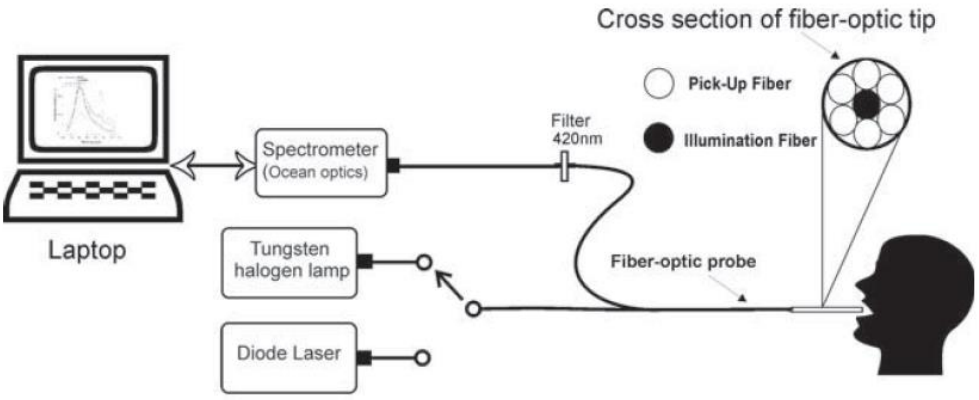

Figure 1.15 Optical system used by Jayanthi *et al.* [30] for spectroscopy signals extraction (reprinted from [30] with permission from Wiley).

Imaizumi *et al.* [31] performed an *ex-vivo* study about the potential of the fluorescence imaging technique for detection of colonic adenomas, using a CCD camera to acquire the fluorescence images. The fluorescence images from tumor and normal slices were acquired between 450 and 490 nm, with excitation at 365 nm (F_{365ex}) and at 405 nm (F_{405ex}), optimized for NADH (reduced form of nicotinamide adenine dinucleotide) fluorescence and reference fluorescence, respectively. The same slices were subjected to histopathological examination by two pathologists that made histopathological diagnoses. Ratio images were created by dividing F_{365ex} by F_{405ex}. The results obtained by the authors show that the average signal intensity in F_{365ex}/F_{405ex} in adenomas is different from that in the adjacent normal mucosa, which proves the potential of the fluorescence imaging as a promising technique for endoscopic detection of early colonic adenomas.

Angelova *et al.* [20] developed a study about the fluorescence potential for detection of gastrointestinal pathologies. The authors performed measurements of biological tissues *in-vitro* and *in-vivo*. For the *in-vitro* measurements (excitation between 280 and 440 nm; and emission between 300 and 800 nm), the authors used a system based on a Xe lamp, monochromators, a fiber optic probe and a PMT (photomultiplier tube) detector with high performance. For the *in-vivo* measurements (excitation at 405 nm; and emission between 450 and 900 nm), the authors used an optical fiber probe inserted through the instrumental channel of the endoscope for light deliver and collection, a high-power LED as excitation source, a microspectrometer and a computer. The tissues sites analyzed with fluorescence measurements during endoscopic procedures were also histological analyzed for the results verification. Concerning the *in-vitro* measurements, the fluorescence intensity of a tumor area was much lower than that for the normal mucosa (detected from one sample from a patient with colon carcinoma surgically removed). Different spectral shapes were also reported from the *in-vitro* study. In the *in-vivo* study, the authors used an exogenous fluorophore (5-ALA/PpIX) as fluorescent marker for dysplasia and tumor detection in esophagus, stomach and colon. The results obtained with the use of an exogenous fluorophore showed a very good differentiation between normal and abnormal tissues, leading to conclude the usefulness for the clinical practice of the exogenous fluorescence diagnosis.

Liu *et al.* [32] performed a study to assess the potential of the multiphoton imaging technique, including TPEF (two-photon excitation fluorescence), to investigate the esophageal cancer. The authors performed *ex-vivo* measurements using human normal and cancerous

esophagus tissues and were mainly focused on the spectral characteristics of human normal and cancerous esophageal submucosa. The imaging system used by the authors was a laser scanning confocal microscope, with a spectro-grating and a 32 channel high-sensitivity PMT detector, combined with a Ti:sapphire mode-locked femtosecond laser. The results obtained by the authors showed distinct TPEF signals between the normal and cancer esophagus tissues, in part due to the changes in collagen concentration on tissues. The authors demonstrated the potential of the multiphoton imaging technique for minimally invasive esophagus cancer diagnosis.

Finally, NBI (narrow-band imaging) is an optical image-enhanced technology that can be used in the early detection of gastric cancers. This technique uses narrow bandwidth filters in the red-green-blue sequential illumination system. The filters can be enabled during conventional endoscopy. The blue and green lights penetrate less deeply in the gastric mucosa and are mainly absorbed by hemoglobin and, that way, vessels appear dark colored. The signals obtained with the blue and green filters can be combined to form an image that highlights the vasculature on the superficial mucosa, improving the detection of irregular microvascular and microsurface patterns. Figure 1.16 shows an example of an image enhanced endoscopy appearance of early gastric cancer. On the other hand, the red light penetrates more deeply and, as a result, the deep layers of the mucosa (large collecting vessels) can also be observed. One of the limitations of the NBI, which is a technique that relies on improved anatomic resolution and contrast, is the fact that requires magnification for an ideal use [33-37]. Moreover, comparing with optical spectroscopy, with this image technology it is not possible to extract quantitative information about morphological and biochemical tissue constituents that provides an objective diagnosis, as happens with diffuse reflectance and fluorescence spectroscopies.

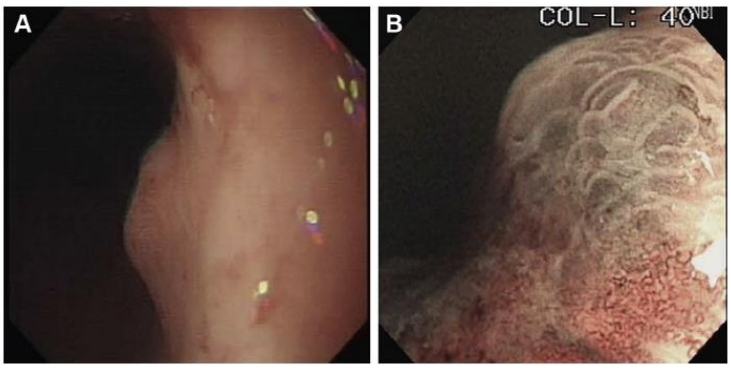

Figure 1.16 (A) White light endoscopy image of early gastric cancer. (B) Narrow band magnifying image of early gastric cancer showing irregular microvascular and microsurface patterns (reprinted from [33] with permission from GII Editorial Office).

1.4 Motivation and objectives

As previously described on section 1.3, several authors have performed studies and developed prototypes for spectroscopy signals extraction and detection of GI cancers. However, most of the authors use complex and bulky spectroscopy systems, such as Xe lamps, lasers, monochromators, optical fibers and high quantum efficiency detectors. Other authors have tried to miniaturize their systems, replacing some of the components with photodiodes or LEDs. However, they still use some macroscopic equipment and none of the studies integrate, in a single chip, all the optical detectors and the readout electronics for digital output signal [2, 38].

Taking advantage of the powerful tool, e.g., system on chip integration provided by the microtechnology, the development of a spectroscopy microsystem on a chip, without the need of regular optical fibers, monochromators or high quantum efficiency detectors, that can be used *in-loco*, will have a high clinical value. This is the main innovation of the work under this thesis. This microsystem can be used as a portable system in a surgery room, for inspecting total removing of the cancerous tissue during surgery. Moreover, it can also be integrated with the conventional endoscopic equipment and be used as an auxiliary in early GI dysplasia detection or to mark possible biopsy sites [2, 19, 38].

Such microsystem would comprise miniaturized LEDs for spectroscopy illumination and an array of silicon photodiodes and its readout electronics for further signal processing. Each photodiode has a thin-film optical filter deposited on its top, tuned for each of the relevant spectral bands (selected for signals extraction in [39]), therefore allowing the detection of both diffuse reflectance and fluorescence signals. Finally, a communication mode can also be considered, all integrated in a single chip, for data transmission and its analysis – Figure 1.17 [2, 19, 38].

This thesis focuses on that microsystem implementation for extraction of the spectroscopic signals, using high selective optical filters especially developed for this purpose, photodiodes and its readout electronics. The use of an integrated optical filtering system, will allow the extraction of diffuse reflectance and fluorescence signals without the use of heavy and complex equipment, such as monochromators, featuring system miniaturization and on-chip integration. With all the optics integrated on a chip, especially the optical filters deposited on the top of the photodetection system (photodiodes), the distances between elements are reduced, allowing a better coupling of light from one element to the next. Moreover, the number of optical interfaces is also reduced by contacting the various optical components, reducing interfaces at which optical losses can occur [2, 19, 40].

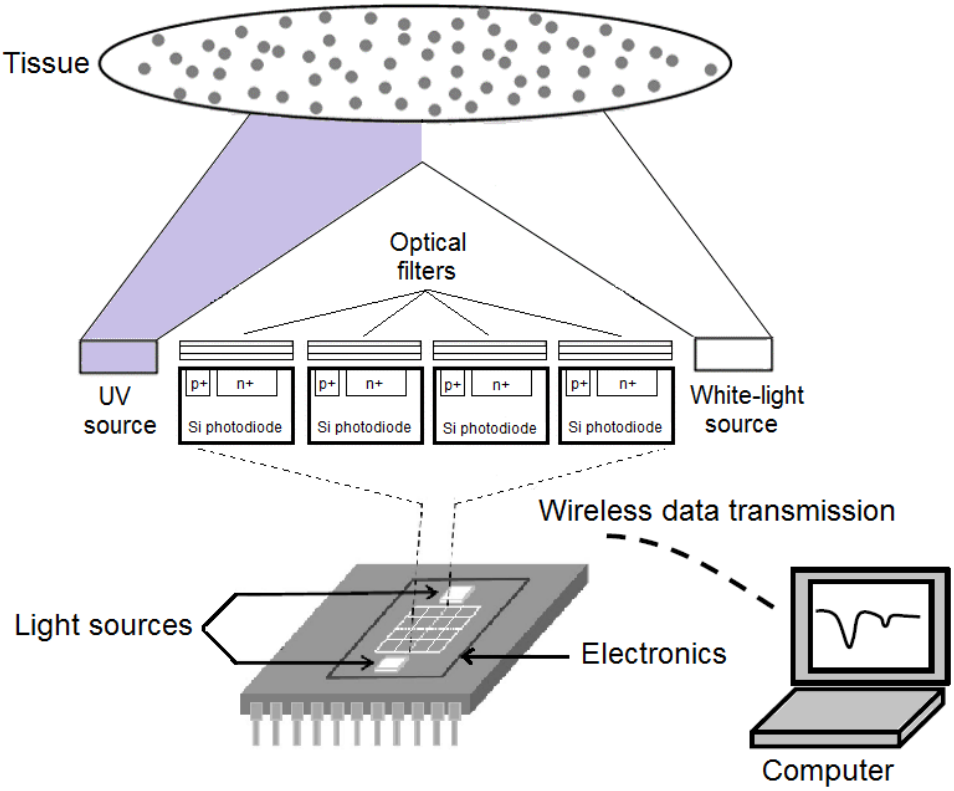

Figure 1.17 Spectroscopy microsystem for diffuse reflectance and fluorescence signals extraction. The optical filters select the signals in the relevant spectral bands (the number of layers in the optical filters in only representative). The UV and white-light sources are used for tissue illumination, featuring the fluorescence and diffuse reflectance measurements, respectively (not scaled, adapted from [39] with permission from OSA).

1.5 Organization of the thesis

This document is divided in six chapters, covering theoretical sections, development, simulation and implementation, as well as the results obtained and their respective discussion. Chapter 1 presents the global incidence of GI cancer, as well as a discussion of the anatomy, functionality and cancer progression in the GI tract. Moreover, the most significant studies using optical spectroscopies for GI cancer detection or GI tissue characterization are described. Finally, the motivation for this thesis and its main objectives are also presented. Chapter 2 describes the diffuse reflectance and fluorescence spectroscopy techniques, their main features and some of the experimental tests performed for signals study. Moreover, the spectroscopic signals analysis and their reconstruction with a discrete number of wavelengths is discussed. Chapter 3 deals with the design, fabrication and characterization of thin-film optical filters, featuring the miniaturized spectroscopy system implementation. Chapter 4 presents the microsystem implementation on CMOS (complementary metal oxide semiconductor) technology, including the photodiodes and its

readout electronics based on the implementation of LF (light-to-frequency) converters. Chapter 5 describes the experimental results in the extraction of diffuse reflectance and fluorescence signals with the use of the fabricated thin-film optical filters and the CMOS microsystem. Moreover, the integration of the optical filters on the top of the CMOS photodiodes is discussed. Finally, the main conclusions and future work are presented in Chapter 6.

References

[1] W. H. Organization. (2015, February, 2016). *Key factors about cancer: Fact sheet N°297.* Available: http://www.who.int/mediacentre/factsheets/fs297/en/

[2] S. Pimenta, S. Cardoso, E. M. S. Castanheira and G. Minas, "Advances towards a miniaturized optical system for gastrointestinal cancer detection using diffuse reflectance and fluorescence spectroscopies", in *Gastrointestinal Cancers: Prevention, Detection and Treatment*, Volume 1, Chapter 13, A. K. Tyagi and S. Prasad (Editors), Nova Publishers, New York, 1 Dec. 2016; ISBN: 978-1-53610-168-3.

[3] W. H. Organization. (2015, February, 2016). *Globocan 2012: Estimated Cancer Incidence, Mortality and Prevalence Worldwide in 2012*. Available: http://globocan.iarc.fr/Pages/fact_sheets_cancer.aspx

[4] A. O. O. Chan and B. Wong. (2015, February, 2016). *Epidemiology of gastric cancer*. Available: http://www.uptodate.com/contents/epidemiology-of-gastric-cancer

[5] F. A. Macrae. (2015, February, 2016). *Colorectal cancer: Epidemiology, risk factors, and protective factors*. Available: http://www.uptodate.com/contents/colorectal-cancer-epidemiology-risk-factors-and-protective-factors#H90629946

[6] Y. Zhang, "Epidemiology of esophageal cancer", *World Journal of Gastroenterology,* vol. 19, pp. 5598-5606, 2013.

[7] I. A. R. C. - WHO. (February, 2016). *EUCAN - Country factsheets: Portugal*. Available: http://eco.iarc.fr/eucan/Country.aspx?ISOCountryCd=620#block-table-a

[8] C.-C. Yu, C. Lau, G. O'Donoghue, J. Mirkovic, S. McGee, L. Galindo*, et al.*, "Quantitative Spectroscopic Imaging for Non-invasive Early Cancer Detection", *Optics Express,* vol. 16, pp. 16227-16239, 2008.

[9] B. O. Schneeman, "Gastrointestinal physiology and functions", *British Journal of Nutrition,* vol. 88, pp. 159-163, 2002.

[10] L. Sherwood, *Human Physiology: From Cells to Systems*, 7 ed. Belmont, USA: Brooks/Cole, 2010.

[11] WebMD. (2005-2016, June, 2016). *The Digestive System*. Available: http://www.webmd.com/digestive-disorders/digestive-system

[12] R. G. Kessel, *Basic Medical Histology: The Biology of Cells, Tissues, and Organs*. New York: Oxford University Press, 1998.

[13] I. Georgakoudi, "The Color of Cancer", *Journal of Luminescence,* vol. 119-120, pp. 75-83, 2006.

[14] H. Mashimo and R. K. Goyal. (2006, January, 2016). *Physiology of esophageal motility*. Available: http://www.nature.com/gimo/contents/pt1/full/gimo3.html

[15] B. Kuo and D. Urma. (2006, January, 2016). *Esophagus - anatomy and development*. Available: http://www.nature.com/gimo/contents/pt1/full/gimo6.html

[16] B. Mayinger, P. Horner, M. Jordan, C. Gerlach, T. Horbach, W. Hohenberger*, et al.*, "Light-induced autofluorescence spectroscopy for tissue diagnosis of GI lesions", *Gastrointestinal Endoscopy,* vol. 52, pp. 395-400, 2000.

[17] J. J. Bergman, "The endoscopic diagnosis and staging of oesophageal adenocarcinoma", *Best Practice & Research Clinical Gastroenterology,* vol. 20, pp. 843-866, 2006.

[18] I. Georgakoudi, B. C. Jacobson, J. V. Dam, V. Backman, M. B. Wallace, M. G. Mueller*, et al.*, "Fluorescence, Reflectance, and Light-Scattering Spectroscopy for Evaluating Dysplasia in Patients With Barrett's Esophagus", *Gastroenterology,* vol. 120, pp. 1620-1629, 2001.

[19] S. Pimenta, S. Cardoso, A. Miranda, P. De Beule, E. Castanheira and G. Minas, "Design and fabrication of SiO_2/TiO_2 and MgO/TiO_2 based high selective optical filters for diffuse reflectance and fluorescence signals extraction", *Biomedical Optics Express,* vol. 6, pp. 3084-3098, 2015.

[20] L. Angelova, E. Borisova, A. Zhelyazkova, M. Keremedchiev, B. Vladimirov and L. Avramov, "Fluorescence spectroscopy of gastrointestinal tumors: in vitro studies and in vivo clinical applications", in *1st International Conference*, 2013, pp. 903209-903209-11.

[21] J. Q. Brown, K. Vishwanath, G. M. Palmer and N. Ramanujam, "Advances in Quantitative UV-Visible Spectroscopy for Clinical and Pre-clinical Application in Cancer", *Current Opinion in Biotechnology,* vol. 20, pp. 119–131, 2009.

[22] D. S. Ferreira, V. C. Pinto, J. H.Correia and G. Minas, "Spectroscopic Detection of Gastrointestinal Dysplasia Using Optical Microsensors", *IEEE Transactions on Biomedical Engineering,* vol. 58, pp. 2633-2639, 2011.

[23] J. W. Tunnell, A. E. Desjardins, L. Galindo, I. Georgakoudi, S. A. McGee, J. Mirkovic*, et al.*, "Instrumentation for Multi-modal Spectroscopic Diagnosis of Epithelial Dysplasia", *Technology in Cancer Research & Treatment,* vol. 2, pp. 505-514, 2003.

[24] B. Mayinger, M. Jordan, P. Horner, C. Gerlach, S. Muehldorfer, B. R. Bittorf*, et al.*, "Endoscopic Light-induced Autofluorescence Spectroscopy for the Diagnosis of Colorectal Cancer and Adenoma", *Journal of Photochemistry and Photobiology B: Biology,* vol. 70, pp. 13-20, 2003.

[25] L. B. Lovat, K. Johnson, G. D. Mackenzie, B. R. Clark, M. R. Novelli, S. Davies*, et al.*, "Elastic scattering spectroscopy accurately detects high grade dysplasia and cancer in Barrett's oesophagus", *Gut,* vol. 55, pp. 1078-1083, 2006.

[26] A. Dhar, K. S. Johnson, M. R. Novelli, S. G. Bown, I. J. Bigio, L. B. Lovat*, et al.*, "Elastic scattering spectroscopy for the diagnosis of colonic lesions: initial results of a novel optical biopsy technique", *Gastrointestinal Endoscopy,* vol. 63, pp. 257-261, 2006.

[27] B. Yu, J. Y. Lo, T. F. Kuech, G. M. Palmer, J. E. Bender and N. Ramanujam, "Cost-effective Diffuse Reflectance Spectroscopy Device for Quantifying Tissue Absorption and Scattering In-vivo", *Journal of Biomedical Optics,* vol. 13, p. 060505 (3pp), 2008.

[28] J. Y. Lo, B. Yu, H. L. Fu, J. E. Bender, G. M. Palmer, T. F. Kuech*, et al.*, "A Strategy for Quantitative Spectral Imaging of Tissue Absorption and Scattering Using Light Emitting Diodes and Photodiodes", *Optics Express,* vol. 17, pp. 1372-1384, 2009.

[29] R. J. Mallia, N. Subhash, A. Mathews, R. Kumar, S. S. Thomas, P. Sebastian*, et al.*, "Clinical grading of oral mucosa by curve-fitting of corrected autofluorescence using diffuse reflectance spectra", *Head & Neck,* vol. 32, pp. 763-779, 2010.

[30] J. L. Jayanthi, N. Subhash, M. Stephen, E. K. Philip and V. T. Beena, "Comparative evaluation of the diagnostic performance of autofluorescence and diffuse reflectance in oral cancer detection: a clinical study", *Journal of Biophotonics,* vol. 4, pp. 696-706, 2011.

[31] K. Imaizumi, Y. Harada, N. Wakabayashi, Y. Yamaoka, H. Konishi, P. Dai*, et al.*, "Dual-wavelength excitation of mucosal autofluorescence for precise detection of diminutive colonic adenomas", *Gastrointestinal Endoscopy,* vol. 75, pp. 110-117, 2012.

[32] N. Liu, G. Chen, S. Wu and R. Chen, "Distinguishing human normal or cancerous esophagus tissue ex vivo using multiphoton microscopy", *Journal of Optics,* vol. 16, p. 025301, 2014.

[33] M. Song and T. L. Ang, "Early detection of early gastric cancer using image-enhanced endoscopy: Current trends", *Gastrointestinal Intervention,* vol. 3, pp. 1-7, 2014.

[34] Y. Ezoe, M. Muto, N. Uedo, H. Doyama, K. Yao, I. Oda*, et al.*, "Magnifying narrowband imaging is more accurate than conventional white-light imaging in diagnosis of gastric mucosal cancer", *Gastroenterology,* vol. 141, pp. 2017-2025. e3, 2011.

[35] K. Kuznetsov, R. Lambert and J. Rey, "Narrow-band imaging: potential and limitations", *Endoscopy,* vol. 38, pp. 76-81, 2006.

[36] K. Yao, H. Doyama, T. Gotoda, H. Ishikawa, T. Nagahama, C. Yokoi*, et al.*, "Diagnostic performance and limitations of magnifying narrow-band imaging in screening endoscopy of early gastric cancer: a prospective multicenter feasibility study", *Gastric Cancer,* vol. 17, pp. 669-679, 2014.

[37] A. M. Buchner and M. B. Wallace, "Future expectations in digestive endoscopy: competition with other novel imaging techniques", *Best Practice & Research Clinical Gastroenterology,* vol. 22, pp. 971-987, 2008.

[38] S. Pimenta, J. Carmo, R. Correia, G. Minas and E. Castanheira, "Characterization of silicon photodiodes for diffuse reflectance signal extraction", in *IEEE 4th Portuguese Meeting on Bioengineering (ENBENG),* 2015, pp. 1-4.

[39] D. S. Ferreira, J. Mirkovic, R. F. Wolffenbuttel, J. H. Correia, M. S. Feld and G. Minas, "Narrow-band Pass Filter Array for Integrated Opto-Electronic Spectroscopy Detectors to Assess Esophageal Tissue", *Biomedical Optics Express,* vol. 2, pp. 1703-1716, 2011.

[40] G. Minas and S. O. Catarino, "Lab-on-a-chip devices for chemical analysis", *Encyclopedia of Microfluidics and Nanofluidics,* pp. 1511-1531, 2015.

2 Optical spectroscopy techniques

As previously referred, the final microsystem must be able to measure diffuse reflectance and fluorescence signals, whose changes in intensity and shape can be related with GI cancer progression. This chapter describes in detail the main characteristics of diffuse reflectance and fluorescence spectroscopy techniques, specifically, their typical spectral intensity and shape and their dependence with temperature. Moreover, it is discussed the use of some models for analysis of the spectroscopic signals, which allows to extract quantitative information related with the morphology and biochemistry of a tissue. Finally, the reconstruction of the spectroscopic signals with a discrete number of wavelengths is discussed, featuring the final microsystem implementation with a narrow-band optical filtering system.

2.1 Diffuse reflectance spectroscopy: basic theory

DRS (diffuse reflectance spectroscopy) is a technique that measures the light that is diffusely reflected from the tissues. When a light beam reaches a target tissue, it interacts with the biomolecules present in the tissue through absorption and scattering events. Thus, the diffuse reflected signal is the light that returns to a tissue surface after the incident light beam get either scattered and/or absorbed in the tissue – Figure 2.1 [1, 2].

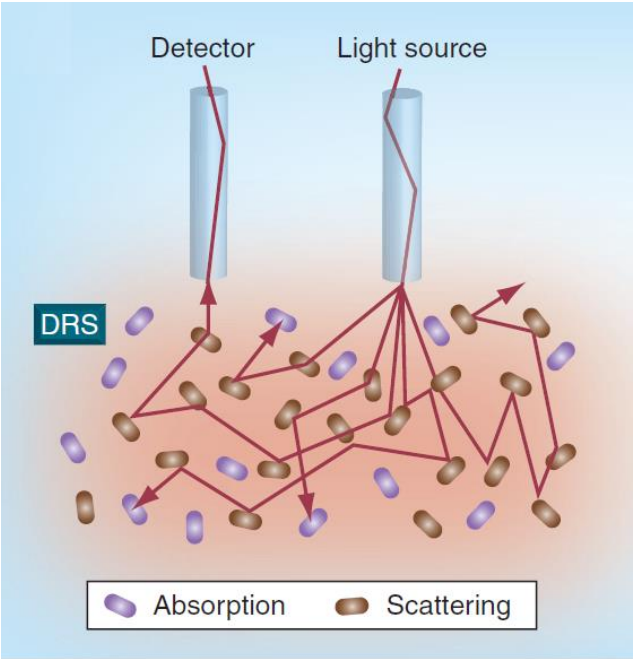

Figure 2.1 Schematic overview of DRS (adapted from [2] with permission from Future Medicine Ltd).

The absorption occurs when the frequency of the incident photon in a molecule is equal or exceeds the frequency associated with the molecule transition energy. This leads to a reduction of the light beam intensity, since the photon energy is transferred to the absorbing molecule [3].

Taking into account the epithelial tissues from the GI tract, the hemoglobin is the main absorber molecule (in the light spectral range of the reported application – 350 nm to 750 nm). It is present in both oxygenated (HbO_2) and deoxygenated (Hb) forms, which have slightly different absorption properties. The major absorption peaks are in the 350-450 nm and 520-590 nm spectral regions [1]. As a result, the hemoglobin concentration can be directly quantified from the absorption component of the diffuse reflectance spectrum of a GI tissue.

The absorption coefficient ($\mu_a(\lambda)$) is a wavelength (λ) dependent parameter which reflects the probability that a photon (with a specific wavelength) will be absorbed by the tissue when it traverses an infinitesimal step within the medium. It is dependent of the concentration of the main absorber molecule (C_i) and its extinction coefficient ($\varepsilon_i(\lambda)$) through Equation 2.1 [2, 4, 5]. $\varepsilon_i(\lambda)$ represents the absorbing light molecule capacity as a function of wavelength [6].

$$\mu_a(\lambda) = \ln(10) \times C_i \times \varepsilon_i(\lambda)$$

Equation 2.1

Figure 2.2 shows the molar extinction coefficient for HbO_2 and Hb between 350 nm and 750 nm. The main absorption peaks for both forms of hemoglobin are clearly visible.

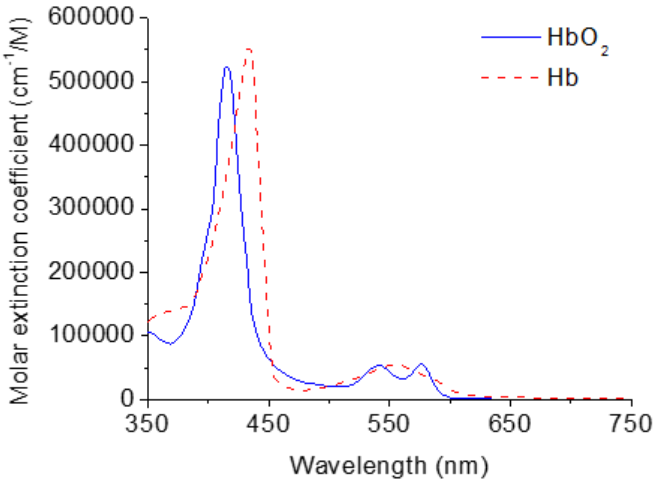

Figure 2.2 Molar extinction coefficient for HbO_2 and Hb (data extracted from [7]).

The photons can also be scattered when impinge on a molecule. The scattering in biological tissues in caused by the microscopic variations in the refractive index. In scattering, the propagation direction of a light beam changes but its intensity is maintained [3].

DRS takes into account the photons that get scattered multiple times in the tissue before being detected at the tissue surface. Generally, a photon travels between 0.05 and 0.2 mm before it gets scattered by some tissue molecule. There are multiple cellular organelles that cause light scattering. However, since the tissue scattering occurs predominantly in the forward direction, the scattered photons finish traveling most of their time in the connective tissue. As a result, the information of the scattering component of the diffuse reflectance signal is related mainly with the underlying connective tissue, where the collagen fibers are the major scattering components [1].

The parameter that is used to describe tissue scattering is the scattering coefficient ($\mu_s(\lambda)$), which is also wavelength dependent. $\mu_s(\lambda)$ describes the fraction of scattered light per unit distance in a scattering medium. It is dependent on the average distance travelled by a photon before it gets scattered and on the scatterer concentration. Another important parameter is the reduced scattering coefficient ($\mu_s'(\lambda)$) which is related with $\mu_s(\lambda)$ by Equation 2.2. The $g(\lambda)$ is the anisotropy factor that takes into account the angular dependence of the scattering events [1, 3, 4].

$$\mu_s'(\lambda) = \mu_s(\lambda) \times (1 - g(\lambda))$$

Equation 2.2

The parameter $g(\lambda)$ is usually used to indicate how strongly forward directed the scattering is [8]. For $g(\lambda) = 0$, there is an isotropic scattering; and for $g(\lambda) = 1$, there is a complete forward scattering of the incident light. Biological tissues are systems where strongly forward scattering occurs and the anisotropy factor varies approximately between 0.69 and 0.99 [3].

Thus, when a light beam reaches a biological tissue, it interacts with the biomolecules existent in the tissue through absorption and scattering events, before returning to the tissue surface. As a consequence, the diffuse reflectance signal carries information about the absorption and scattering properties of the tissue, i. e. carries morphological and biochemical information which can characterize the state of the tissue: normal or with some degree of

malignancy [2, 9, 10]. Accordingly, a decrease of the scattering component and, consequently, a reduction on the diffuse reflectance signal intensity can be associated with the presence of GI dysplasia, since the quantity of light that reaches the collagen fibers from the connective tissues is reduced with cancer progression (due to an increase of the epithelium tissue thickness [1]). Moreover, an increase of hemoglobin concentration (associated with the angiogenesis [growth of new blood vessels] during dysplasia progression [4, 11]) may also result in a reduction of the diffuse reflectance signal intensity, due to a higher absorption of the light beam that reaches the tissue [12].

2.2 Fluorescence spectroscopy: basic theory

The fluorescence emission is a physical phenomenon that occurs after a molecule has absorbed energy, when illuminated by a light beam with a specific wavelength (named excitation wavelength - $\lambda_{excitation}$) in the UV/visible spectral region. In that case, the molecule absorbs the light energy and is activated from the electronic ground state to reach an electronic excited state. However, since the electronic excited states are unstable, the molecule tends to emit the excess energy and return to its initial state, the ground state. The process is usually accompanied by photons emission [2, 3, 13].

The fluorescence of a molecule (also named fluorophore) is characterized by the excited-state lifetime (τ_F) and the fluorescence quantum yield (Φ_F). The lifetime is the average time the molecule spends in the excited state. The quantum yield measures the fraction of absorbed energy that is converted into fluorescence [3].

The shape and intensity of a fluorescence spectrum is related with the fluorophores concentrations in the target tissue and their fluorescence properties, such as the molecules absorption power at the excitation wavelength, their quantum yield and the fraction of light emitted at the emission wavelength [2, 3]. Moreover, it is important to note that during the electronic excitation of the molecules or fluorophores, the excess absorbed energy is spent by collisions between the molecules that form the target tissue, a process known as vibrational relaxation (Figure 2.3). It is an efficient process that occurs after the electronic excitation during some picoseconds. As a consequence of this efficiency, the fluorescence emission is shifted to a higher wavelength (lower energy) when compared to the absorption spectrum – *Stokes* deviation (Figure 2.4) [13].

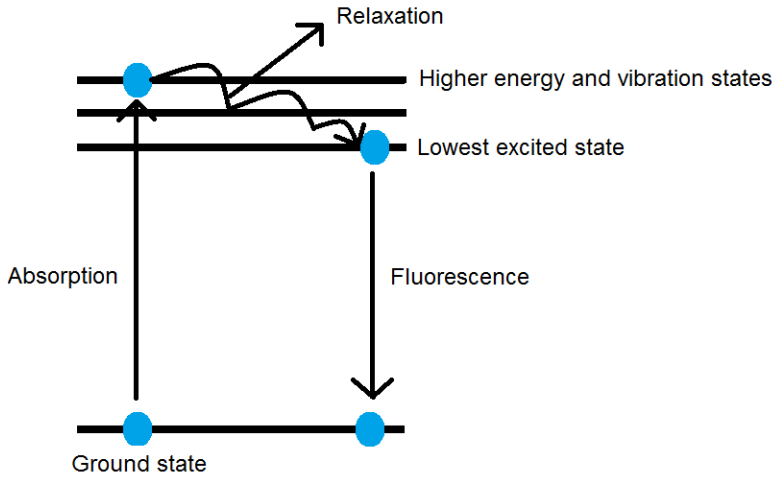

Figure 2.3 Diagram of the fluorescence emission phenomenon, including the vibrational relaxation (adapted from [14]).

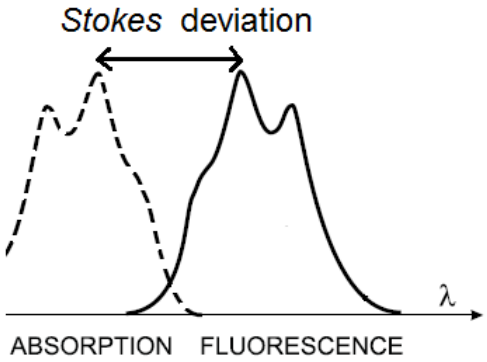

Figure 2.4 Relative positions of absorption and fluorescence (the curves shape and intensity is merely representative), (adapted from [13] with permission from Wiley).

It is also important to note that, in the fluorescence process, an emitted photon can be scattered before returning to the tissue surface (Figure 2.5), or even absorbed. Thus, the fluorescence spectrum of a tissue suffers some distortions introduced by absorption and scattering events on the tissue. As a result, nowadays there are several models/methods capable of removing such distortions, improving the quantification and identification of the tissue fluorophores and their excitation and emission properties. The fluorescence spectrum without distortion of absorption and scattering events is known as intrinsic fluorescence spectrum [1, 2, 15].

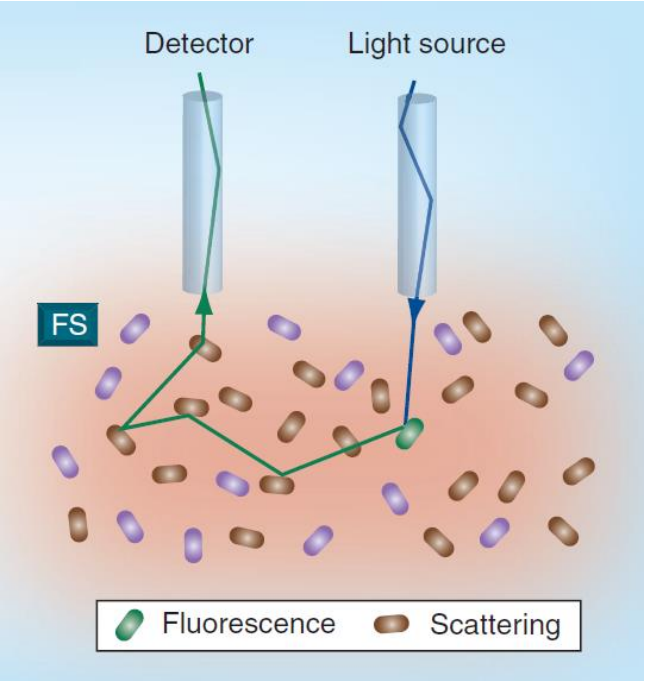

Figure 2.5 Schematic overview of the FS (fluorescence spectroscopy) technique with distortions introduced by a scattering event (adapted from [2] with permission from Future Medicine Ltd).

There are several endogenous tissue fluorophores with different excitation and emission characteristics that are involved in the transformations occurring in the neoplastic process and carry different information about tissue biochemical composition. For example, fluorescence from NADH is a sensitive indicator of tissue metabolic activity, with excitation/emission maxima at 340/450 nm approximately. Moreover, fluorescence from collagen can be an indicator of structural integrity, with excitation/emission maxima at 330/390 nm approximately [1, 2, 4]. Thus, a decrease in collagen (as a result of the cellular integrity loss) and an increase in NADH (associated with an increase in the metabolic cellular activity), both related with dysplasia progression [1, 16], leads to a change in the shape and intensity of the fluorescence spectrum of a tissue [12].

2.3 Diffuse reflectance signal study: temperature dependence and typical spectra intensity and shape

The study of the dependence with temperature of the diffuse reflectance signal is essential to confirm if some changes in the signal can be related with the tissue temperature and not with the dysplasia progression.

In order to evaluate the temperature dependence of the diffuse reflectance signal, experimental measurements were performed with a set of phantoms, representative of the absorption and scattering phenomena that affects the diffuse reflectance signal. The prepared phantoms were mixtures of hemoglobin, intralipid (a scatterer representative of the collagen fibers) with variable concentrations and water. The used hemoglobin is water soluble and was obtained from *Sigma-Aldrich* (*H0267*). The used intralipid is a 20% emulsion and was also obtained from *Sigma Aldrich* (*I141*). With these phantoms, the absorption and scattering properties of the GI tissues are represented.

The diffuse reflectance spectra at different temperatures, Tr (room temperature, 22°C), T1 (37 °C), T2 (40 °C) and T3 (42 °C) approximately, were measured between 350 nm and 750 nm using a UV-Vis-NIR spectrophotometer (*Shimadzu UV-3101PC*) equipped with an integrating sphere. It was used a standard $BaSO_4$ (barium sulfate) as reference for the 100% of diffuse reflectance. Moreover, the diffuse reflectance of a quartz cuvette with water was subtracted from the total diffuse reflectance in order to remove its effect from the diffuse reflectance signal.

Table 2.1 shows three phantoms prepared with a variable concentration of hemoglobin and intralipid. Figure 2.6 shows the diffuse reflectance spectra for phantom (b) of Table 2.1 at the four temperatures tested (Tr, T1, T2 and T3).

Table 2.1 Phantoms prepared for temperature tests of the diffuse reflectance signal.

Phantoms	Hemoglobin concentration (mg/mL)	Intralipid mass concentration (%)
(a)	0.25	2.00
(b)	0.50	1.00
(c)	1.00	0.50

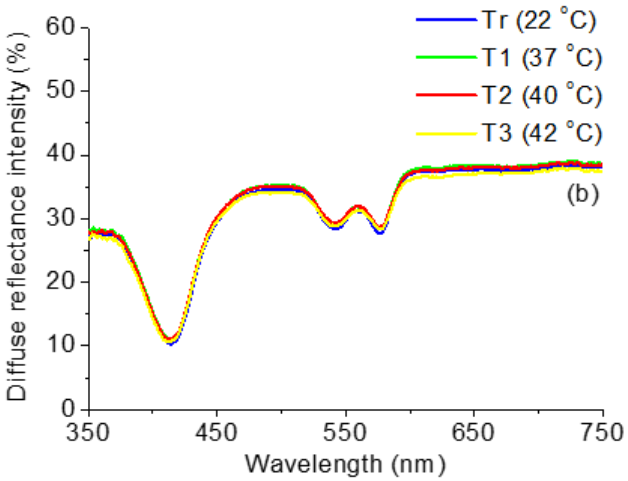

Figure 2.6 Diffuse reflectance spectra for phantom (b) of Table 2.1 at four temperatures.

As it can be seen, the diffuse reflectance signal is similar for all the temperatures tested. For the remaining phantoms similar results were obtained. However, for precisely checking the relation between temperature and diffuse reflectance signal intensity, the results obtained with the three phantoms were analyzed in *SPSS* software, through a partial correlation, controlling for wavelength and consequently for components concentration. The partial correlation coefficients were used in this statistical analysis and a *p-value* < 0.05 was considered statistically significant. The *SPSS* output is shown on Figure 2.7. The results allow concluding that the temperature does not have a statistically significant affectation ($r_{4809} = -0.001$, $p > 0.05$) in the diffuse reflectance spectra, in the range of tested temperatures (22 °C to 42 °C, approximately).

Correlations

Control Variables			Temperature	DR_Intensity
Wavelength	Temperature	Correlation	1.000	-.001
		Significance (2-tailed)	.	.949
		df	0	4809
	DR_Intensity	Correlation	-.001	1.000
		Significance (2-tailed)	.949	.
		df	4809	0

Figure 2.7 *SPSS* output for the partial correlation performed with the three phantoms of Table 2.1 at the four temperatures (DR – Diffuse reflectance).

Figure 2.8 shows the diffuse reflectance spectra of phantoms (a), (b) and (c) of Table 2.1 at room temperature. Concerning the spectral intensity, it is in agreement with the expected, which is a decrease of the diffuse reflectance signal intensity (from (a) to (c)) with the increase of hemoglobin concentration (due to a higher absorption of the light beam, especially in the hemoglobin absorption peaks: 417, 547 and 575 nm [17]) and the decrease of intralipid concentration (less scattering of the light beam).

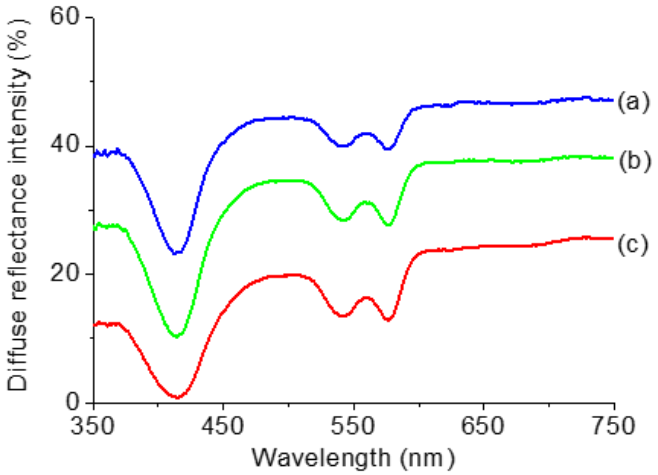

Figure 2.8 Diffuse reflectance spectra of phantoms (a), (b) and (c) of Table 2.1, at room temperature.

2.4 Fluorescence signal study

2.4.1 Temperature dependence and typical spectra intensity and shape

As previously performed for diffuse reflectance signal, the temperature dependence of the fluorescence signal was also investigated, in order to conclude if some changes in the fluorescence signal can be related with the tissue temperature and not with dysplasia progression. As a result, a more representative set of phantoms was considered, since it is necessary to represent their fluorescence properties, in addition to the absorption and scattering properties of the GI tissues.

A set of liquid homogeneous phantoms were prepared, with variable concentrations of an absorber (hemoglobin, *H0267* from *Sigma-Aldrich*), a scatterer (1 μm diameter polystyrene microspheres, *07310* from *Polysciences*) and two fluorophores – NADH (*N6005* from *Sigma-Aldrich*) and Carbostyril 124 (7-amino-4-methyl-2(1*H*)-quinolinone, *363308* from *Sigma-Aldrich*), a hydroxyquinoline derivative that represents the emission from collagen. The structures of both fluorophores are shown in Figure 2.9. The fluorophores NADH and Carbostyril 124 are soluble in

a 0.01 M NaOH solution (*35262* from *Fluka*) and in absolute ethanol (spectroscopic grade, from *Merck Millipore*), respectively.

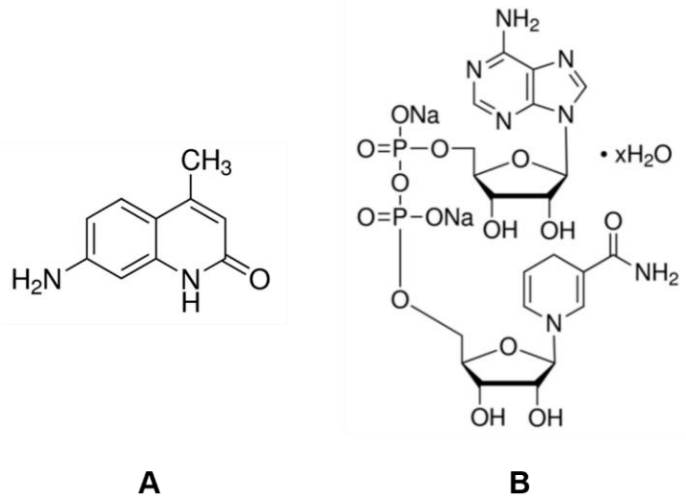

Figure 2.9 Structures of the fluorophores (A) Carbostyril 124 (reprinted from [18]) and (B) NADH (reprinted from [19]).

In this phase, it was decided to use a different scatterer, the polystyrene microspheres (to represent the collagen fibers of GI tissues), since it was observed (in the experimental tests performed) that intralipid exhibits fluorescence emission when excited with UV or blue wavelength visible light, which will hamper the interpretation of fluorescence spectra.

Table 2.2 presents the three phantoms prepared for the tests of the temperature dependence. For each phantom, the fluorescence signal, between 380 nm and 600 nm, was obtained at four temperatures – Tr (room temperature, 22 °C), T1 (37 °C), T2 (40 °C) and T3 (42 °C), approximately. It was used an excitation wavelength of 350 nm and a commercial spectrofluorometer (*SPEX® FluoroLog® 2*) [20]. The spectrofluorometer uses as reference a solution of Rhodamine B in ethylene glycol (8 g/L), avoiding fluctuations in the light source and detector systems.

Table 2.2 Phantoms prepared for temperature tests of the fluorescence signal.

Phantom	Hemoglobin concentration (mg/mL)	Polystyrene mass concentration (%)	NADH concentration (μg/mL)	Carbostyril concentration (μg/mL)
(a)	0.25	0.50	0.50	1.50
(b)	0.50	0.25	1.00	1.00
(c)	1.00	0.15	1.50	0.50

Figure 2.10 shows the fluorescence spectra for phantom (b) of Table 2.2 at the four temperatures tested (Tr, T1, T2 and T3). It is important to note that the fluorescence signal is only represented between 380 and 600 nm, since that range is representative of the fluorescence emission properties of the fluorophores NADH and Carbostyril 124 [21-23].

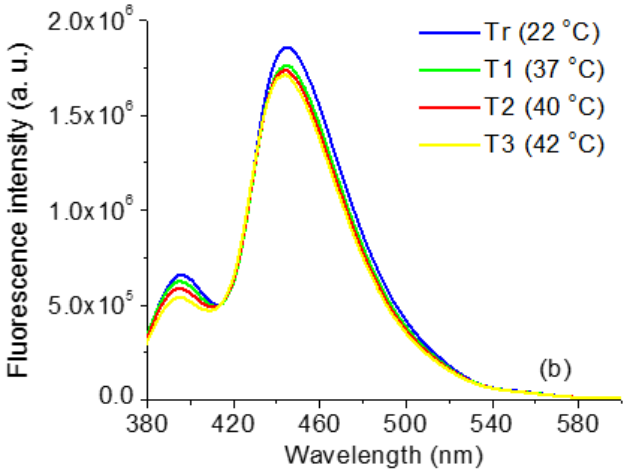

Figure 2.10 Fluorescence spectra ($\lambda_{excitation}$ = 350 nm) for phantom (b) of Table 2.2 at four temperatures.

As it can be observed, there are slight differences between the fluorescence signals at different temperatures, which are in accordance with the expected. Generally, an increase in temperature results in a decrease in the fluorescence quantum yield and excited-state lifetime, because the non-radiative processes related with thermal agitation (collisions with solvent molecules, intramolecular vibrations and rotations, etc.) are more efficient at higher temperatures, leading to a decrease in the fluorescence intensity [13]. Similar results were obtained for the remaining phantoms [20].

The obtained results were also analyzed with the *SPSS* software, through a partial correlation, for checking the relation between temperature and fluorescence signal intensity, controlling for wavelength and, consequently, for components concentration. The partial correlation coefficients were used in this statistical analysis and a *p-value* < 0.05 was considered statistically significant. Figure 2.11 shows the *SPSS* output. As it can be seen, the results allow concluding that despite the slight differences between the fluorescence signal intensities at different temperatures (negative correlation coefficient), they are not statistically significant (r_{3009} = -0.007, p > 0.05), in the temperature range tested (22 °C to 42 °C, approximately) [20].

Correlations

Control Variables			Temperature	F_Intensity
Wavelength	Temperature	Correlation	1.000	-.007
		Significance (2-tailed)	.	.718
		df	0	3009
	F_Intensity	Correlation	-.007	1.000
		Significance (2-tailed)	.718	.
		df	3009	0

Figure 2.11 *SPSS* output for the partial correlation performed with the three phantoms of Table 2.2 at the four temperatures (F - Fluorescence).

The fluorescence signal of a tissue (named bulk fluorescence) is affected by absorption and scattering events, which introduces distortions in the fluorescence spectra, hampering the identification and quantification of tissue fluorophores [1, 15].

The fluorophore NADH has a maximum fluorescence emission around 450-460 nm with a quantum efficiency of approximately 2% [21, 23, 24]. The fluorophore Carbostyril 124 has a maximum fluorescence emission at 417 nm with a quantum efficiency of 97% [22]. Moreover, as the Carbostyril concentration increases, a second fluorescence emission peak arises close to 440 nm, probably due to the formation of Carbostyril aggregates (see Figure 2.12B). Finally, both fluorophores can be excited at 350 nm.

Figure 2.12 shows a comparison between the spectrum of each fluorophore in a diluted solution and in a phantom (containing hemoglobin and polystyrene microspheres), obtained experimentally. It can be noted that, despite the same fluorophore concentration, the spectra in

phantoms (turbid media) are very different from the ones in homogeneous dilute solution, as the fluorescence emitted from the surface of a turbid medium may change from isotropic to anisotropic [25]. In addition to the differences in intensity, due to the absorption and scattering effects in phantoms, the spectral shape is also affected, especially in the case of Carbostyril 124. Moreover, it is also important to note that the spectrum in phantom (B) is very similar to the one reported for an arterial tissue sample [25], evidencing that the tissues fluorescence is dominated by collagen, due to the low quantum efficiency of NADH (only 2%). The valley near 420 nm corresponds to the main absorption band of hemoglobin (the Soret band) [25].

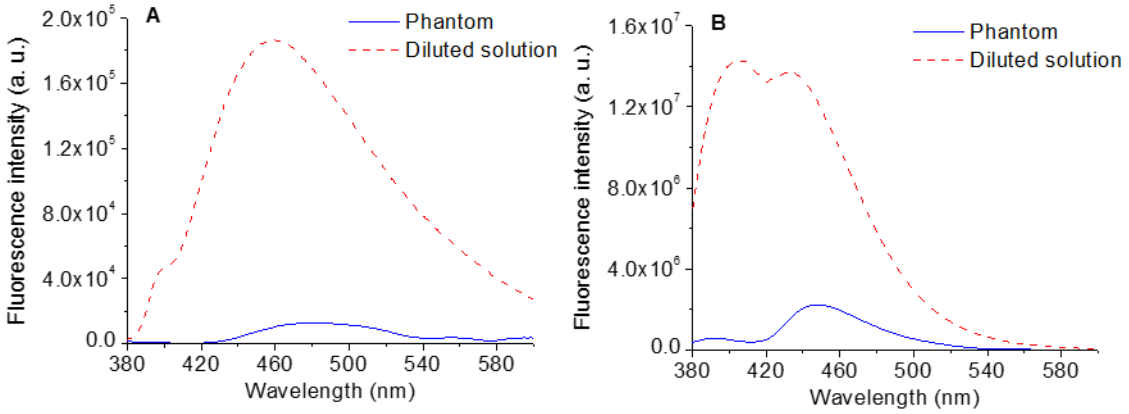

Figure 2.12 Fluorescence emission spectra ($\lambda_{excitation}$ = 350 nm) of NADH 1.5 µg/mL (A) and Carbostyril 124 1.5 µg/mL (B) in a diluted solution and in a phantom (with 1 mg/mL of hemoglobin and 0.15% of polystyrene microspheres).

Figure 2.13 shows the bulk fluorescence spectra of each phantom ((a), (b) and (c)) presented in Table 2.2, at room temperature. It can be observed that, as the NADH concentration increases and the Carbostyril 124 decreases (from (a) to (c) on Table 2.2), the global fluorescence intensity decreases (especially the first peak close to 400 nm) due to a lower Carbostyril 124 concentration, which is the fluorophore with a higher contribution to the fluorescence intensity, due to the high quantum efficiency (97%). In addition, the second fluorescence peak becomes larger and with a slight shift to higher wavelengths, which is the typical NADH affectation in the fluorescence spectra [26]. Moreover, the three fluorescence spectra are similar (in shape) to the phantom spectrum of Figure 2.12B, as expected. However, the ration between the two emission peaks (near 450 nm and 400 nm) is higher, due to the presence of the fluorophore NADH. Considering the three phantoms of Table 2.2, the ratio between the two emission peaks is 3.02, 4.08 and 5.64 (from (a) to (c) on Table 2.2, respectively), due to an increase in the NADH

concentration along these phantoms. However, the increase in the ratio between the two bands is not proportional to the NADH concentration, since the fluorescence intensity and, consequently, the ratio values are affected by absorption and scattering events, which will be discussed in the next section – section 2.4.2.

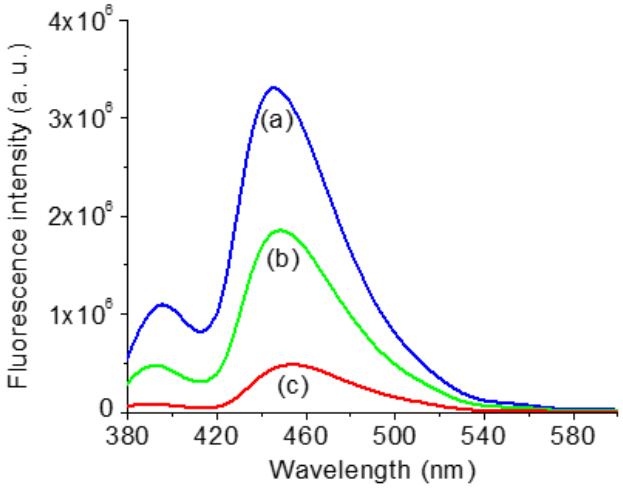

Figure 2.13 Bulk fluorescence spectra ($\lambda_{excitation} = 350$ nm) for phantoms (a) to (c) of Table 2.2 at room temperature.

Finally, Figure 2.14 shows the diffuse reflectance spectra of the three phantoms presented on Table 2.2 (phantoms with all the components representing the absorption, scattering and fluorescence properties of the GI tissues, which were not considered previously on Figure 2.8), measured between 350 nm and 750 nm using an UV-Vis-NIR spectrophotometer (*Shimadzu UV-3101PC*) equipped with an integrating sphere. It was used a standard $BaSO_4$ as reference for the 100% of diffuse reflectance. As before, the diffuse reflectance of a quartz cuvette with water was subtracted from the total diffuse reflectance, in order to remove its effect from the diffuse reflectance signal. As expected, the diffuse reflectance signal intensity decreases (from (a) to (c)) with the increase of hemoglobin concentration (due to a higher absorption of the light beam, especially in the hemoglobin absorption peaks) and the decrease of polystyrene spheres concentration (less scattering of the light beam).

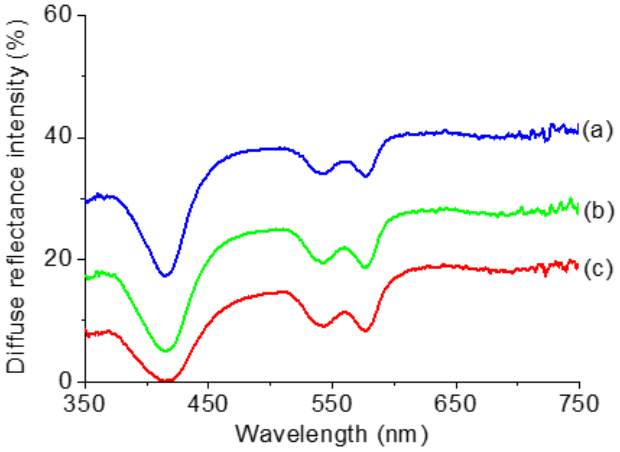

Figure 2.14 Diffuse reflectance spectra of phantoms (a), (b) and (c) of Table 2.2, at room temperature.

2.4.2 Absorption and scattering distortions in the fluorescence spectra

The fluorescence signal of a tissue is affected by absorption and scattering events, which introduce distortions in the fluorescence spectrum of a tissue.

In order to observe those distortions, based on phantom (b) of Table 2.2, two more phantoms were prepared, with the same fluorophores concentrations, but with different hemoglobin and polystyrene microspheres concentrations – Table 2.3. The Figure 2.15 shows their fluorescence spectra at room temperature.

Table 2.3 Phantoms prepared to better observe the absorption and scattering distortions on the fluorescence spectra.

Phantom	Hemoglobin concentration (mg/mL)	Polystyrene mass concentration (%)	NADH concentration (μg/mL)	Carbostyril concentration (μg/mL)
(b)	0.50	0.25	1.00	1.00
(d)	0.50	0.50	1.00	1.00
(e)	1.00	0.25	1.00	1.00

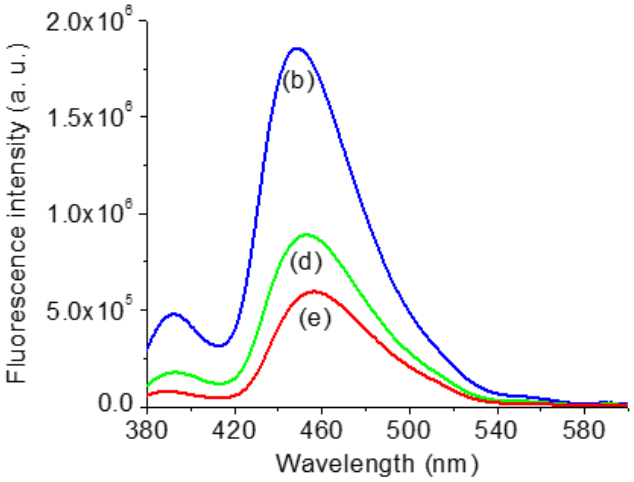

Figure 2.15 Bulk fluorescence spectra ($\lambda_{excitation} = 350$ nm) for phantoms (b), (d) and (e) of Table 2.3 at room temperature.

Comparing the fluorescence spectra of phantoms (b), (d) and (e) of Table 2.3, in spite of having the same fluorophores concentration, they have distinct spectra. As expected, the fluorescence intensity decreases as the hemoglobin concentration increases (phantoms (b) and (e) of Table 2.3), due to an increase in absorption. The same happens when the concentration of polystyrene beads is increased, due to the enhancement of scattering (Phantoms (b) and (d) of Table 2.3).

Those results show that it is important the implementation of a model to extract the intrinsic fluorescence (fluorescence without absorption and/or scattering distortions, only due to tissue fluorophores) from the bulk fluorescence (measured in a turbid media such as a phantom), in order to identify and quantify the tissue fluorophores and their concentration changes that may occur during GI cancer progression.

Figure 2.16 shows the experimental intrinsic fluorescence for the three phantoms (b), (d) and (e) of Table 2.3 and for the phantoms (a) and (c) of Table 2.2. The experimental intrinsic fluorescence was obtained using a sample with only Carbostyril 124 and NADH (in the same concentration of the respective phantom). Analyzing the experimental spectra, the intrinsic fluorescence spectrum of phantom (c) presents only one emission peak (near to 420 nm), since the fluorescence is dominated by Carbostyril 124 (representative of collagen), which has high quantum efficiency. However, the presence of a higher NADH concentration (comparing with the other phantoms) is also responsible for the occurrence of a larger peak, which is an effect already

reported and attributed to the influence of NADH [26]. Concerning the experimental spectra for the other phantoms, they have two emission peaks. As NADH presents a low fluorescence quantum yield, the second peak (at higher wavelength) may by influence by some aggregation of the Carbostyril 124 or by FRET (fluorescence resonance energy transfer) from Carbostyril 124 to NADH (with a rise in emission of the latter) [13]. As the Carbostyril 124 concentration is higher, the spectral intensity is also higher (especially the first peak, which is close to the emission fluorescence peak of Carbostyril 124), but not proportional to its concentration.

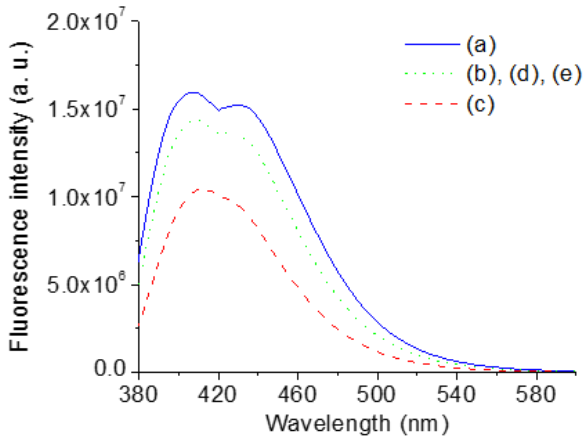

Figure 2.16 Experimental intrinsic fluorescence ($\lambda_{excitation}$ = 350 nm) for all the phantoms of Table 2.2 and Table 2.3.

2.5 Spectroscopy models for signals analysis

The GI cancer progression involves several morphological and biochemical changes on the tissues (as previously explained), which leads to a change in the way the light interacts with the tissues, i. e. changing the shape and intensity of the diffuse reflectance and fluorescence signals. As a result, the signals extraction is fundamental for providing a complete information about the status of the analyzed tissue: normal or with a probability of malignancy presence. However, the signals analysis is also important to extract valuable information for tissue characterization. Thus, in this section a brief discussion about the signals analysis will be presented, referring some work already performed by the research group.

As an example, a direct comparison (trough statistical tests) between signals from normal tissues and an unknown tissue (to be analyzed in a moment) can anticipate, based on differences in intensity and shape of the signals, a possible malignancy presence in the analyzed tissue and mark it as a biopsy site, with which the presence or absence of malignancy will be confirmed. This

can work as an auxiliary to the pathologist during the typical endoscopy and colonoscopy techniques, avoiding the blind biopsies.

Moreover, several authors analyze the spectroscopic extracted signals (diffuse reflectance and fluorescence) with mathematical models in order to extract quantitative information that could improve the detection of changes of tissues properties during cancer progression. The diffuse reflectance signal can be used to extract the absorption and reduced scattering coefficients ($\mu_a(\lambda)$ and $\mu_s'(\lambda)$) of a tissue. The fluorescence signal can be used to extract the intrinsic fluorescence, allowing the identification of the tissue fluorophores and their relative contributions for the overall tissue fluorescence.

Previous work developed by the research team [27, 28] used an approximation of the transport diffuse equation, developed by Zonios *et al.* [29], for the extraction of absorption and reduced scattering coefficients. For the intrinsic fluorescence signal extraction (from the bulk fluorescence spectra in combination with the diffuse reflectance spectra), the research team used a photon migration model developed by Wu *et al.* [30]. Finally, the intrinsic fluorescence spectra were fitted using a linear combination of the tissue fluorophores basis spectra.

The main goal of this thesis is to develop a miniaturized spectroscopy system. In the conventional spectroscopy setups, the signals extraction and its discrimination over a wavelength range is achieved in steps of 1 nm and using a spectrograph, which is not suitable in a miniaturized system. The discrimination of the signals will be achieved using a narrow-band optical filtering system (that will be described in detail in chapter 3). Thus, a study previously conducted by the research team showed the viability of using only 16 wavelengths for signals extraction and quantification of tissue information [27, 28].

In that study, it was used an existing spectroscopy data set with fluorescence and diffuse reflectance signals from esophageal tissues (non-dysplastic and dysplastic). The Figure 2.17 shows representative diffuse reflectance and intrinsic fluorescence spectra for normal and dysplastic tissues [27, 28].

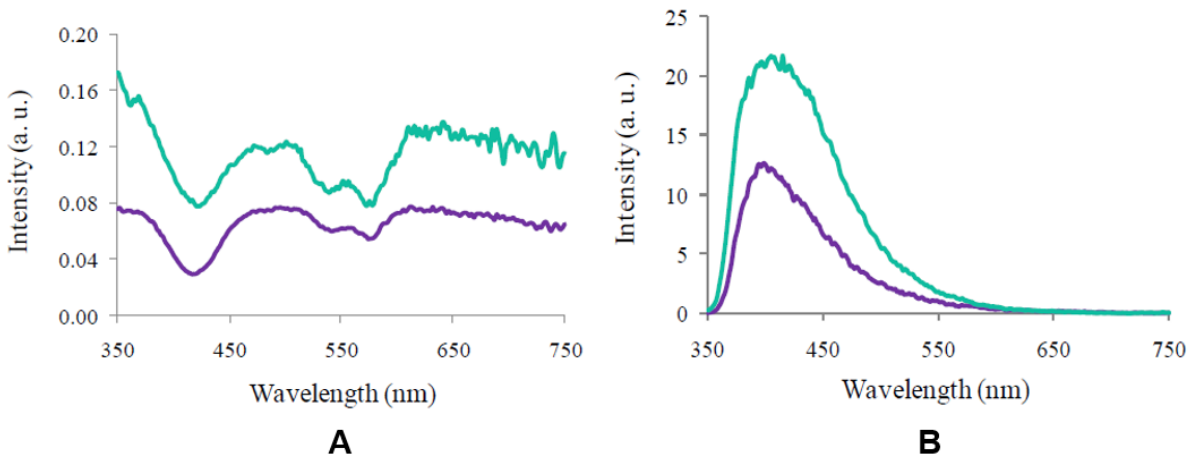

Figure 2.17 Representative diffuse reflectance (A) and intrinsic fluorescence (B) spectra for normal (upper lines) and dysplastic tissue (bottom lines) (adapted from [28]).

The research team implemented the diffuse reflectance and fluorescence algorithms in *Matlab* software for quantification of tissue information (extraction of tissue optical properties) and compared the results obtained with the full spectra (between 350 nm and 750 nm, in steps of 1 nm) and with the spectra reconstructed from the 16 spectral bands (achieved by linear interpolation): 350, 370, 380, 400, 420, 450, 480, 510, 540, 560, 580, 600, 620, 650, 700, and 750 nm. Figure 2.18 shows and example of reconstructed spectra (using the 16 spectral bands) of the same samples represented on Figure 2.17 [27, 28].

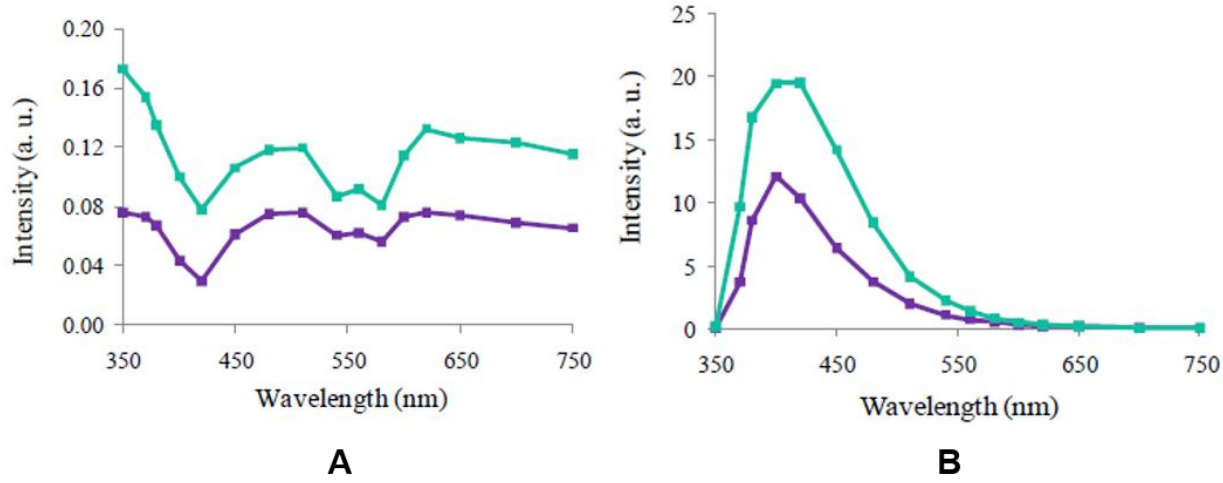

Figure 2.18 Reconstructed diffuse reflectance (A) and intrinsic fluorescence (B) spectra for normal (upper lines) and dysplastic tissue (bottom lines) (adapted from [28]).

Different combinations of 16 wavelengths were simulated. All of them used 6 fixed points: 350 and 750 nm, the first and the last in the analysis; 420, 540 and 580 nm, close to the hemoglobin absorption peaks; and 700 nm, a reference wavelength. The other wavelengths were selected within the full visible range. The wavelength selection took into account the accuracy of the extraction of tissue optical properties but also the constraints inherent to the optical filter fabrication process, for example the filters FWHM (full width half maximum) since the filters transmittance spectra should not overlap [27, 28].

A more reduced number of spectral bands can be useful to reduce the complexity and the size of the final microsystem. However, a compromise between an accurate extraction of the tissue optical properties and the number of wavelengths must be considered. Therefore, 16 wavelengths were considered that compromise. As an example, the research group performed a study for extraction of the optical tissue properties using only 10 spectral bands. They verified low correlations between the parameters extracted with the reconstructed spectra and with the full spectra, especially in the extraction of the reduced scattering coefficient [27, 28].

Thus, the 16 selected wavelengths (between 350 and 750 nm) provided good results for tissues characterization, which made possible the optical filters design and fabrication.

2.6 Conclusion

In this chapter the main characteristics of the diffuse reflectance and fluorescence spectroscopy techniques were described. The typical spectra intensity and shape of the signals were study as well as their dependence with the temperature, performing some measurements with phantoms with different biochemical components concentrations. The obtained results allowed to conclude that the temperature has not a significant effect on the diffuse reflectance and fluorescence spectra. It was also concluded that the diffuse reflectance spectra shape and intensity is affected by the absorption and scattering components of the phantoms with a reduction of the signal intensity as the absorption increases and the scattering decreases. The fluorescence signal shape and intensity is affected by the fluorophores (especially by the one with higher quantum efficiency) presented in the phantoms and suffers from distortions introduced by absorption and scattering events. In addition, it was discussed the implementation of some models for spectroscopic signal analysis, featuring the extraction of quantitative information related with the morphology and biochemistry of a tissue. Finally, the reconstruction of the signals with a discrete

number of wavelengths was discussed, taking into account previous work performed by the research team. It was concluded that 16 wavelengths are enough for the signals extraction and quantification of tissue information. That way, the implementation of the final microsystem is achieved with optical filters design and fabrication centered at the 16 selected wavelengths.

References

[1] I. Georgakoudi, "The Color of Cancer", *Journal of Luminescence,* vol. 119-120, pp. 75-83, 2006.

[2] D. Evers, B. Hendriks, G. Lucassen and T. Ruers, "Optical spectroscopy: current advances and future applications in cancer diagnostics and therapy", *Future oncology,* vol. 8, pp. 307-320, 2012.

[3] C. Zhu, "The use of Fluorescence and Diffuse Reflectance Spectroscopy for Breast Cancer Diagnosis", PhD, Electrical Engineering, University of Wisconsin-Madison, Madison, USA, 2007.

[4] J. Q. Brown, K. Vishwanath, G. M. Palmer and N. Ramanujam, "Advances in Quantitative UV-Visible Spectroscopy for Clinical and Pre-clinical Application in Cancer", *Current Opinion in Biotechnology,* vol. 20, pp. 119–131, 2009.

[5] G. M. Palmer and N. Ramanujam, "Monte Carlo-based inverse model for calculating tissue optical properties. Part I: Theory and validation on synthetic phantoms", *Applied Optics,* vol. 45(5), pp. 1062-1071, 2006.

[6] T. F. Scientific. (2015, February, 2016). *Fluorescence Fundamentals*. Available: https://www.thermofisher.com/pt/en/home/references/molecular-probes-the-handbook/introduction-to-fluorescence-techniques.html

[7] S. Prahl. (1999, February, 2016). *Optical Absorption of Hemoglobin*. Available: http://omlc.org/spectra/hemoglobin/

[8] G. I. Zonios, "Diffuse Reflectance Spectroscopy for Human Colon Tissue", PhD, Department of Physics, Massachusetts Institute of Technology, Massachusetts, USA, 1998.

[9] C.-C. Yu, C. Lau, G. O'Donoghue, J. Mirkovic, S. McGee, L. Galindo*, et al.*, "Quantitative Spectroscopic Imaging for Non-invasive Early Cancer Detection", *Optics Express,* vol. 16, pp. 16227-16239, 2008.

[10] J. Y. Lo, B. Yu, H. L. Fu, J. E. Bender, G. M. Palmer, T. F. Kuech, *et al.*, "A Strategy for Quantitative Spectral Imaging of Tissue Absorption and Scattering Using Light Emitting Diodes and Photodiodes", *Optics Express,* vol. 17, pp. 1372-1384, 2009.

[11] H.-W. Wang, J.-K. Jiang, C.-H. Lin, J.-K. Lin, G.-J. Huang and J.-S. Yu, "Diffuse reflectance spectroscopy detects increased hemoglobin concentration and decreased oxygenation during colon carcinogenesis from normal to malignant tumors", *Optics Express,* vol. 17, pp. 2805-2817, 2009.

[12] S. Pimenta, S. Cardoso, E. M. S. Castanheira and G. Minas, "Advances towards a miniaturized optical system for gastrointestinal cancer detection using diffuse reflectance and fluorescence spectroscopies", in *Gastrointestinal Cancers: Prevention, Detection and Treatment*, Volume 1, Chapter 13, A. K. Tyagi and S. Prasad (Editors), Nova Publishers, New York, 1 Dec. 2016; ISBN: 978-1-53610-168-3.

[13] B. Valeur, *Molecular Fluorescence: Principles and Applications* Germany: Wiley-VCH, 2001.

[14] M. W. Davidson. (2015, February, 2016). *Interactive Tutorials: Jablonski Energy Diagram*. Available: https://micro.magnet.fsu.edu/primer/java/jablonski/lightandcolor/index.html

[15] Q. Zhang, M. G. Müller, J. Wu and M. S. Feld, "Turbidity-free Fluorescence Spectroscopy of Biological Tissue", *Optics Letters,* vol. 25, pp. 1451-1453, 2000.

[16] S. McGee, V. Mardirossian, A. Elackattu, J. Mirkovic, R. Pistey, G. Gallagher, *et al.*, "Anatomy-based algorithms for detecting oral cancer using reflectance and fluorescence spectroscopy", *Annals of Otology, Rhinology & Laryngology,* vol. 118, pp. 817-826, 2009.

[17] A. Nonoyama, A. Garcia-Lopez, L. H. Garcia-Rubio, G. F. Leparc and R. L. Potter, "Hypochromicity in red blood cells: an experimental and theoretical investigation", *Biomedical Optics Express,* vol. 2, pp. 2126-2143, 2011.

[18] Sigma-Aldrich. (2016, February, 2016). *363308 Aldrich Carbostyril 124 99%*. Available: http://www.sigmaaldrich.com/catalog/product/aldrich/363308?lang=pt&region=PT

[19] Sigma-Aldrich. (2016, February, 2016). *N6005 Sigma Beta-Nicotinamide adenine dinucleotide, reduced disodium salt hydrate >94%.* Available: http://www.sigmaaldrich.com/catalog/product/sigma/n6005?lang=pt&region=PT

[20] S. Pimenta, E. Castanheira and G. Minas, "Study of the fluorescence signal for gastrointestinal dysplasia detection", in *Second International Conference on Applications of Optics and Photonics*, 2014, pp. 92864I-92864I-5.

[21] Sigma-Aldrich. (2012, February, 2016). *Product Information - Beta-Nicotinamide adenine dinucleotide, reduced disodium salt hydrate*. Available: http://www.sigmaaldrich.com/content/dam/sigma-aldrich/docs/Sigma/Product_Information_Sheet/2/n6005pis.pdf

[22] X. Dai, E. Rollin, A. Bellerive, C. Hargrove, D. Sinclair, C. Mifflin, *et al.*, "Wavelength Shifters for Water Cherenkov Detectors", *Nuclear Instruments and Methods in Physics Research A,* vol. 589, pp. 290–295, 2008.

[23] J. R. Lakowicz, *Principles Fluorescence Spectroscopy*, Third Edition ed. New York, USA: Springer, 2006.

[24] T. G. Scott, R. D. Spencer, N. J. Leonard and G. Weber, "Synthetic spectroscopic models related to coenzymes and base pairs. V. Emission properties of NADH. Studies of fluorescence lifetimes and quantum efficiencies of NADH, AcPyADH, [reduced acetylpyridineadenine dinucleotide] and simplified synthetic models", *Journal of the American Chemical Society,* vol. 92, pp. 687-695, 1970.

[25] N. Ramanujam, "Fluorescence Spectroscopy In Vivo," in *Encyclopedia of Analytical Chemistry*, R. A. Meyers, Ed., ed. Chichester: John Wiley & Sons Ltd, 2000, pp. 20-56.

[26] M. G. Müller, I. Georgakoudi, Q. Zhang, J. Wu and M. S. Feld, "Intrinsic Fuorescence Spectroscopy in Turbid Media: Disentangling Effects of Scattering and Absorption", *Applied Optics,* vol. 40, pp. 4633-4646 2001.

[27] D. S. Ferreira, J. Mirkovic, R. F. Wolffenbuttel, J. H. Correia, M. S. Feld and G. Minas, "Narrow-band Pass Filter Array for Integrated Opto-Electronic Spectroscopy Detectors to Assess Esophageal Tissue", *Biomedical Optics Express,* vol. 2, pp. 1703-1716, 2011.

[28] D. S. Ferreira, "Spectroscopy Systems for the Detection of Gastrointestinal Dysplasia", PhD, Escola de Engenharia, Universidade do Minho, Braga, Portugal, 2011.

[29] G. Zonios, L. T. Perelman, V. Backman, R. Manoharan, M. Fitzmaurice, J. V. Dam, *et al.*, "Diffuse Reflectance Spectroscopy of Human Adenomatous Colon Polyps In Vivo", *Applied Optics,* vol. 38, pp. 6628-6637, 1999.

[30] J. Wu, M. S. Feld and R. P. Rava, "Analytical Model for Extracting Intrinsic Fluorescence in Turbid Media", *Applied Optics,* vol. 32, pp. 3585-3595, 1993.

3 Thin-film optical filters

The final microsystem integrates narrow bandpass optical filters based on thin-films, for diffuse reflectance and fluorescence signals selection and detection, in specific spectral bands, previously considered significant for signals extraction featuring GI tissue characterization [1, 2]. The optical filters for selecting the relevant spectral bands avoid the use of heavy and complex equipment, such as monochromators, that are used in the majority of spectroscopy prototypes for several clinical applications.

This chapter describes the design, optimization, fabrication and characterization of 16 MgO/TiO_2 and SiO_2/TiO_2 based high selective narrow bandpass optical filters used in the final microsystem.

3.1 Thin-films properties: basic theory

A thin-film is defined as a specific layer of material with a thickness up to 1 μm, deposited on a substrate – Figure 3.1. The refractive index, n, is defined by the ratio between the speed of light in vacuum and the speed of light in the medium. Generally, the thin-films do not absorb any energy. In this case, the filter characteristic in reflection is the complement of that in transmission. Thus, taking into account the incident light on the film, part of that is reflected and the other is transmitted to the substrate [3].

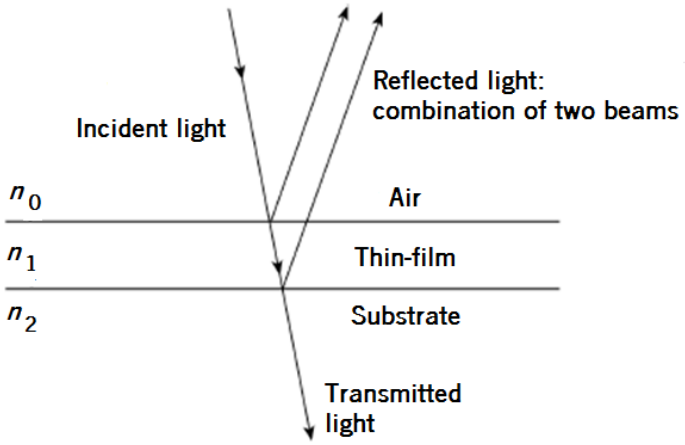

Figure 3.1 Representation of a single thin-film (adapted from [4] by permission of Taylor and Francis Group, and [3]).

In order to understand, qualitatively, the performance of the optical filters based on thin-films, it is necessary to accept three statements [4]:

(1) The amplitude of the reflected light at any boundary between two media is given by Equation 3.1[4].

$$\frac{1-\rho_r}{1+\rho_r}$$

Equation 3.1

where ρ_r is the amplitude reflection coefficient, which is the ratio of the optical admittances at the boundary or the ratio of the refractive indices (n). The reflectance is defined as the square of this amplitude.

(2) There is a phase shift of 180° when the reflectance occurs in a medium that has a lower refractive index when compared with its adjacent medium; and a phase shift of 0° when the reflectance occurs in a medium that has a higher refractive index when compared with its adjacent medium [4].

(3) If the light beam is split in two components by reflection at the top and the bottom of a thin-film, these two light beams will recombine such that the amplitude of the resultant beam is the difference between the amplitudes of the two components, when there is a phase shift of 180° (destructive interference); or is the sum of the amplitudes of the two components, when there is a phase shift of 0° (constructive interference) [4].

The implementation of a thin-film multilayer (deposition of a stack of alternate high and low refractive index films) can be useful to obtain a structure with a constructive interference of the reflected light beams - Figure 3.2. Thus, the effective reflectance of the structure is controlled by the number of layers and can be made very high, increasing the number of layers. This is the elementary form of the high-reflectance coatings [4].

However, when this type of structure is constructed, its reflectance remains high only within a limited range of wavelengths. Outside that range, the reflectance drops to a low value. Therefore, this structure has a reflectance spectrum with maxima and minima at specific wavelengths. As a result, the thin-film multilayers can be used as a basic block for many types of thin-film filters. The

filter characteristic in reflection is the complement of that in transmission if no energy is absorbed by the filter [4].

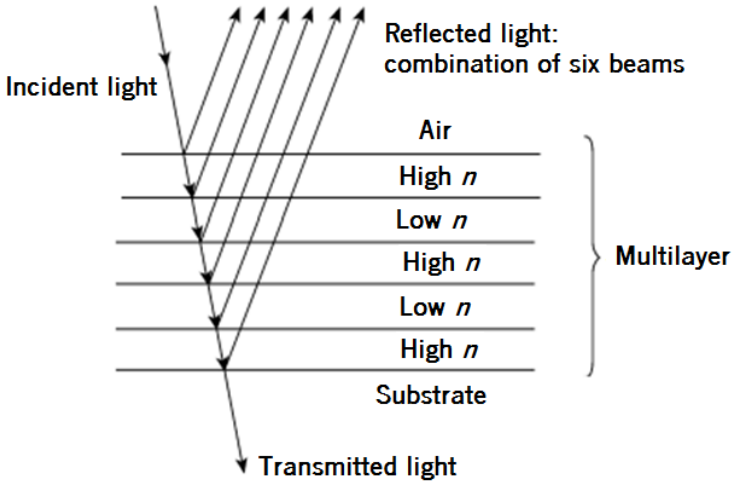

Figure 3.2 Representation of a thin-film multilayer (adapted from [4] by permission of Taylor and Francis Group).

Then, some theoretical concepts will be presented to understand the performance of a multilayer thin-film filter and make the required calculations for its design.

Maxwell's equations and electromagnetic waves

Light is an electromagnetic wave. Thus, its characteristics can be described by the Maxwell equations, which are presented as follows (considering isotropic and uniform media) [4, 5]:

$$\vec{\nabla}.\vec{D} = \rho$$

Equation 3.2

$$\vec{\nabla}.\vec{B} = 0$$

Equation 3.3

$$\vec{\nabla} \times \vec{E} = -\frac{\partial}{\partial t}\vec{B}$$

Equation 3.4

$$\vec{\nabla} \times \vec{H} = \vec{J} + \frac{\partial}{\partial t}\vec{D}$$

Equation 3.5

where $\vec{D}$ is the electric displacement vector, $\vec{B}$ is the magnetic induction vector, $\vec{E}$ is the electric field vector, $\vec{H}$ is the magnetic field vector, ρ is the electric charge density and $\vec{J}$ is the electric current density vector.

The electric current density and the electric displacement can be related with the electric field using the following equations [4, 5]:

$$\vec{J} = \sigma \vec{E}$$

Equation 3.6

$$\vec{D} = \varepsilon \vec{E}$$

Equation 3.7

where σ is the electric conductivity and ε is the permittivity of the medium.

Moreover, the magnetic induction can be related with the magnetic field using the following equation [4, 5]:

$$\vec{B} = \mu \vec{H}$$

Equation 3.8

where μ is the magnetic permeability of the medium.

In free space, μ and ε have the following values [5]:

$$\mu = \mu_0 = 4\pi \times 10^{-7} Hm^{-1}$$

$$\varepsilon = \varepsilon_0 = \frac{10^{-9}}{36\pi} Fm^{-1}$$

where μ_0 and ε_0 are the permeability and the permittivity of the free space, respectively.

Moreover, the permittivity of the free space can be expressed using the following equation [4]:

$$\varepsilon_0 = \frac{1}{\mu_0 c^2}$$

Equation 3.9

where c is the speed of light in free space or in vacuum ($c = 2.997925 \times 10^8 ms^{-1}$).

The following analysis is based on the literature [1, 3-5]. The electric and magnetic fields can be considered two aspects of a unique physical phenomenon: the electromagnetic field. Once there is an electromagnetic variation, it spreads away independently of the source that generated it. The electric and magnetic fields forms a unique entity and regenerate each other continually. In the following analysis, it will be considered a medium free of sources, this is, $J = 0$ and $\rho = 0$. Taking into account Equation 3.4 and solving using Equation 3.2, Equation 3.5, Equation 3.7 and Equation 3.8, it is obtained the following expression:

$$\nabla^2 \vec{E} = \mu\varepsilon \frac{\partial^2}{\partial t^2} \vec{E}$$

Equation 3.10

Using a similar process and for the magnetic induction, it is possible to obtain the following expression:

$$\nabla^2 \vec{B} = \mu\varepsilon \frac{\partial^2}{\partial t^2} \vec{B}$$

Equation 3.11

Equation 3.10 and Equation 3.11 are wave equations. In this case, the velocity of light propagation in a medium, v, is related with the product $\mu\varepsilon$ by the following expression:

$$v = \frac{1}{\sqrt{\mu\varepsilon}}$$

Equation 3.12

The ratio between the velocity of light in vacuum, c, and the velocity of light in a medium, v, defines the refractive index (n) of the medium:

$$n = \frac{c}{v} = \sqrt{\frac{\varepsilon\mu}{\varepsilon_0\mu_0}}$$

Equation 3.13

Generally, the magnetic properties of a medium have an insignificant effect on the velocity of light propagation. So it can be considered that $\mu \approx \mu_0$. As a result, the refractive index of a

medium is determined by its permittivity, which depends on the frequency of the incident electromagnetic wave.

For plane waves (waves whose surfaces of constant phase [wavefronts] are parallel planes normal to the direction of propagation [6]), Equation 3.10 and Equation 3.11 have the following solutions:

$$\vec{E} = \mathrm{Re}\left\{\overrightarrow{E_0} e^{i(\omega t - \vec{k}.\vec{r} + \phi)}\right\}$$

Equation 3.14

$$\vec{B} = \mathrm{Re}\left\{\overrightarrow{B_0} e^{i(\omega t - \vec{k}.\vec{r} + \phi)}\right\}$$

Equation 3.15

where Re indicates the real part, $\overrightarrow{E_0}$ and $\overrightarrow{B_0}$ are vectors that represent the amplitudes of the oscillations, ω is the angular frequency, $\vec{r}$ is the position vector, ϕ is the phase of the wave and $\vec{k}$ is the wave vector.

The frequency, f, and the wavelength, λ, of the electromagnetic wave are given by:

$$f = \frac{\omega}{2\pi}$$

Equation 3.16

$$\lambda = \frac{2\pi}{\left|\vec{k}\right|}$$

Equation 3.17

Finally, the optical admittance of a medium (that measures how easily the light can pass along it) is numerically equal to its refractive index (n) and connects the magnetic and electric fields, $\overrightarrow{H}$ and $\overrightarrow{E}$, respectively:

$$\vec{H} = n\vec{E}$$

Equation 3.18

The reflectance of a thin-film

A thin-film is represented in Figure 3.3. At this point, it is desirable to define a new notation: waves in the direction of incidence with the symbol "+" (positive-going) and waves in the opposite direction with the symbol "–" (negative-going) [1, 4].

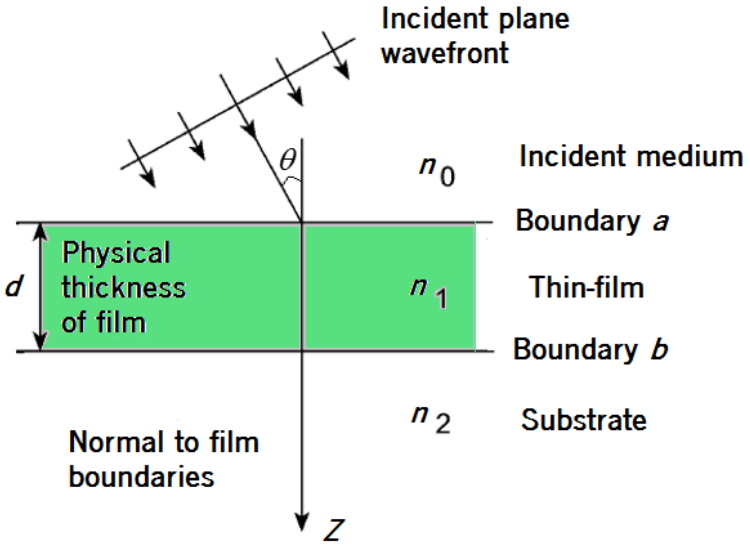

Figure 3.3 Plane wave incident on a thin-film (adapted from [4] by permission of Taylor and Francis Group).

Considering the interface between the film and the substrate (boundary *b* in Figure 3.3), there is no negative-going wave in the substrate. In the film, there is one resultant positive-going wave and one resultant negative-going wave. As a result, at this interface the tangential components of electric and magnetic fields ($\vec{E}$ and $\vec{H}$, respectively) are [1, 4]:

$$E_b = E_{1b}^{+} + E_{1b}^{-}$$

Equation 3.19

$$H_b = n_1 E_{1b}^{+} - n_1 E_{1b}^{-}$$

Equation 3.20

where:

$$E_{1b}^{+} = \frac{1}{2}\left(\frac{H_b}{n_1} + E_b\right)$$

Equation 3.21

$$E_{1b}^{-} = \frac{1}{2}\left(-\frac{H_b}{n_1} + E_b \right)$$

Equation 3.22

$$H_{1b}^{+} = n_1 E_{1b}^{+} = \frac{1}{2}\left(H_b + n_1 E_b \right)$$

Equation 3.23

$$H_{1b}^{-} = -n_1 E_{1b}^{-} = \frac{1}{2}\left(H_b - n_1 E_b \right)$$

Equation 3.24

At the other interface (boundary *a* in Figure 3.3), at the same instant and at a point with similar *x* and *y* coordinates, the electric and magnetic fields can be determined by altering the phase factors of the waves allowing a shift in the *z* coordinate from 0 to -*d*. Thus, the phase factor of the positive-going wave will be multiplied by $e^{i\delta}$ and the phase factor of the negative-going wave will be multiplied by $e^{-i\delta}$, where [1, 4]:

$$\delta = \frac{2\pi n_1 d \cos\theta}{\lambda}$$

Equation 3.25

where *d* is the physical thickness of the thin-film, θ is the light incidence angle and n_1 is the refractive index of the thin-film. δ is defined as the phase thickness that represents the phase shift experienced by the wave when it crosses a distance *d*, normal to the boundary. The optical path length (OPL) is defined as the light distance traveled in a thin-film and can be obtained by the following equation [1]:

$$OPL = n_1 d \cos\theta$$

Equation 3.26

Moreover, if absorption is included (usually, this is not the case for thin-films, which normally are completely transparent [3]), the refractive index (n) will be writing as [7]:

$$n = n - ik$$

Equation 3.27

where k is the extinction coefficient.

Thus, for the interface *a* (Figure 3.3), the tangential components of $\vec{E}$ and $\vec{H}$ are [1, 4]:

$$E_{1a}^{+} = E_{1b}^{+} e^{i\delta} = \frac{1}{2}\left(\frac{H_b}{n_1} + E_b\right) e^{i\delta}$$

Equation 3.28

$$E_{1a}^{-} = E_{1b}^{-} e^{-i\delta} = \frac{1}{2}\left(-\frac{H_b}{n_1} + E_b\right) e^{-i\delta}$$

Equation 3.29

$$H_{1a}^{+} = H_{1b}^{+} e^{i\delta} = \frac{1}{2}\left(H_b + n_1 E_b\right) e^{i\delta}$$

Equation 3.30

$$H_{1a}^{-} = H_{1b}^{-} e^{-i\delta} = \frac{1}{2}\left(H_b - n_1 E_b\right) e^{-i\delta}$$

Equation 3.31

Consequently,

$$E_a = E_{1a}^{+} + E_{1a}^{-} = E_b\left(\frac{e^{i\delta} + e^{-i\delta}}{2}\right) + H_b\left(\frac{e^{i\delta} - e^{-i\delta}}{2n_1}\right) = E_b \cos\delta + H_b \frac{i \sin\delta}{n_1}$$

Equation 3.32

$$H_a = H_{1a}^{+} + H_{1a}^{-} = E_b n_1\left(\frac{e^{i\delta} - e^{-i\delta}}{2}\right) + H_b\left(\frac{e^{i\delta} + e^{-i\delta}}{2}\right) = E_b i n_1 \sin\delta + H_b \cos\delta$$

Equation 3.33

Equation 3.32 and Equation 3.33 can be written in matrix notation [1, 4]:

$$\begin{bmatrix} E_a \\ H_a \end{bmatrix} = \begin{bmatrix} \cos\delta & (i \sin\delta)/n_1 \\ i n_1 \sin\delta & \cos\delta \end{bmatrix} \begin{bmatrix} E_b \\ H_b \end{bmatrix}$$

Equation 3.34

Equation 3.34 relates the tangential components of $\vec{E}$ and $\vec{H}$ at the incident interface (interface *a* of Figure 3.3) with the tangential components of $\vec{E}$ and $\vec{H}$ that are transmitted through the interface *b* (Figure 3.3). The matrix 2×2 is defined as the characteristic matrix of a thin-film [1, 4].

The input optical admittance of the assembly can be defined by [1, 4]:

$$Y = \frac{H_a}{E_a}$$

Equation 3.35

The reflectance of an interface between an incident medium of admittance n_0 and a medium of admittance Y is obtained with the following equation [1, 4]:

$$R = \left(\frac{n_0 - Y}{n_0 + Y}\right)\left(\frac{n_0 - Y}{n_0 + Y}\right)$$

Equation 3.36

Finally, dividing Equation 3.34 by E_b it can be obtained [1, 4]:

$$\begin{bmatrix} \frac{E_a}{E_b} \\ \frac{H_a}{E_b} \end{bmatrix} = \begin{bmatrix} B \\ C \end{bmatrix} = \begin{bmatrix} \cos\delta & (i\sin\delta)/n_1 \\ in_1\sin\delta & \cos\delta \end{bmatrix}\begin{bmatrix} 1 \\ n_2 \end{bmatrix}$$

Equation 3.37

where B and C are the normalized electric and magnetic fields at the front interface and are the quantities that will be used to extract the properties of the thin-film system. $\begin{bmatrix} B \\ C \end{bmatrix}$ is defined as the characteristic matrix of the assembly. Taking into account Equation 3.35 and Equation 3.37, it is also possible to write the following expression:

$$Y = \frac{H_a}{E_a} = \frac{C}{B} = \frac{n_2\cos\delta + in_1\sin\delta}{\cos\delta + i(n_2/n_1)\sin\delta}$$

Equation 3.38

The reflectance of an assembly of thin-films

Figure 3.4 shows another thin-film that was added to the single film presented on Figure 3.3. Thus, the final interface is designated by *c*.

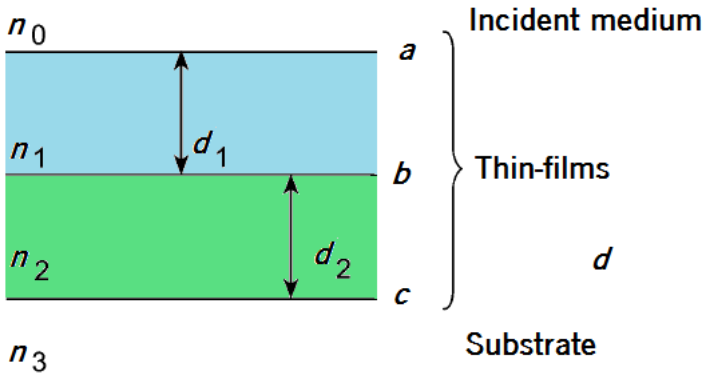

Figure 3.4 Representation of two thin-films on a surface (adapted from [4] by permission of Taylor and Francis Group).

The characteristic matrix of the thin-film more close to the substrate is [1, 4]:

$$\begin{bmatrix} \cos\delta_2 & (i\sin\delta_2)/n_2 \\ in_2\sin\delta_2 & \cos\delta_2 \end{bmatrix}$$

Equation 3.39

Applying Equation 3.34, it is possible to obtain the parameters at the interface *a* [1, 4]:

$$\begin{bmatrix} E_a \\ H_a \end{bmatrix} = \begin{bmatrix} \cos\delta_1 & (i\sin\delta_1)/n_1 \\ in_1\sin\delta_1 & \cos\delta_1 \end{bmatrix} \begin{bmatrix} \cos\delta_2 & (i\sin\delta_2)/n_2 \\ in_2\sin\delta_2 & \cos\delta_2 \end{bmatrix} \begin{bmatrix} E_c \\ H_c \end{bmatrix}$$

Equation 3.40

The characteristic matrix of the assembly is expressed by [1, 4]:

$$\begin{bmatrix} B \\ C \end{bmatrix} = \begin{bmatrix} \cos\delta_1 & (i\sin\delta_1)/n_1 \\ in_1\sin\delta_1 & \cos\delta_1 \end{bmatrix} \begin{bmatrix} \cos\delta_2 & (i\sin\delta_2)/n_2 \\ in_2\sin\delta_2 & \cos\delta_2 \end{bmatrix} \begin{bmatrix} 1 \\ n_3 \end{bmatrix}$$

Equation 3.41

Equation 3.41 can be extended to the case of an assembly of *q* layers. In this case, the characteristic matrix of the assembly is the product of the individual matrices, done in the correct order [1, 4]:

$$\begin{bmatrix} B \\ C \end{bmatrix} = \left\{ \prod_{r=1}^{q} \begin{bmatrix} \cos\delta_r & (i\sin\delta_r)/n_r \\ in_r\sin\delta_r & \cos\delta_r \end{bmatrix} \right\} \begin{bmatrix} 1 \\ n_m \end{bmatrix}$$

Equation 3.42

where m represents the substrate and δ_r can be obtained using the following expression:

$$\delta_r = \frac{2\pi n_r d_r \cos\theta_r}{\lambda}$$

Equation 3.43

where θ_r can be determined from Snell's law, if θ (the light incidence angle) is given:

$$n_0 \sin\theta = n_r \sin\theta_r = n_m \sin\theta_m$$

Equation 3.44

Taking into account Equation 3.36 and Equation 3.38, the reflectance of the thin-films assembly is [1, 4]:

$$R = \left(\frac{n_0 B - C}{n_0 B + C}\right)\left(\frac{n_0 B - C}{n_0 B + C}\right)$$

Equation 3.45

Optical filters with dielectric thin-films: quarter- and half-wave optical thicknesses

The characteristic matrix of a dielectric thin-film (a thin-film with a very little radiation absorption [8]), for a normal light incidence, is simplified if the optical thickness is an integer number of quarter- or half-wave thicknesses [1, 4].

If $\delta = \pi$, then $\cos\delta = \cos\pi = -1$ and $\sin\delta = \sin\pi = 0$. Thus, the layer is an integer number of half-wavelengths thick ($\lambda \setminus 2$) and the characteristic matrix is [1, 4]:

$$\begin{bmatrix} -1 & 0 \\ 0 & -1 \end{bmatrix}$$

This is the unity matrix and in this particular case the thin-film has no effect on the reflectance of an assembly [1, 4].

If $\delta = \frac{\pi}{2}$, then $\cos\delta = \cos\frac{\pi}{2} = 0$ and $\sin\delta = \sin\frac{\pi}{2} = 1$. Thus, the layer is an odd number of quarter-wavelengths thick ($\lambda / 4$) and the characteristic matrix is [1, 4]:

$$\begin{bmatrix} 0 & i/n \\ in & 0 \end{bmatrix}$$

In this particular case, the reflectance of an assembly will have its minimum or maximum peak, depending on the fact that the n of the added thin-film is lower or higher than the n of the substrate, respectively [1].

Since the properties of the assemblies involving quarter- and half-waves optical thicknesses are simple to calculate, the design of optical filters will be based on quarter- and half-waves layers at a reference wavelength. For example, in the case of using two dielectric materials for filters design, the quarter-wave thicknesses are generally represented by *H* or *L*, depending if the material has the highest or the lowest refractive index, respectively. The half-wave thicknesses layers are represented by *HH* or *LL* [1, 4].

Taking into account a multilayer structure with half-wave and quarter-wave thickness layers, *H L H L H LL H L H L H*, with an incident medium of air (refractive index equal to 1) and a substrate of glass (refractive index equal to 1.52), it is possible to write Equation 3.46 (considering n_1 the highest refractive index and n_2 the lowest refractive index):

$$\begin{bmatrix} 0 & \frac{i}{n_1} \\ in_1 & 0 \end{bmatrix} \times \begin{bmatrix} 0 & \frac{i}{n_2} \\ in_2 & 0 \end{bmatrix} \times \begin{bmatrix} 0 & \frac{i}{n_1} \\ in_1 & 0 \end{bmatrix} \times \begin{bmatrix} 0 & \frac{i}{n_2} \\ in_2 & 0 \end{bmatrix} \times \begin{bmatrix} 0 & \frac{i}{n_1} \\ in_1 & 0 \end{bmatrix} \times \begin{bmatrix} -1 & 0 \\ 0 & -1 \end{bmatrix} \times$$
$$\begin{bmatrix} 0 & \frac{i}{n_1} \\ in_1 & 0 \end{bmatrix} \times \begin{bmatrix} 0 & \frac{i}{n_2} \\ in_2 & 0 \end{bmatrix} \times \begin{bmatrix} 0 & \frac{i}{n_1} \\ in_1 & 0 \end{bmatrix} \times \begin{bmatrix} 0 & \frac{i}{n_2} \\ in_2 & 0 \end{bmatrix} \times \begin{bmatrix} 0 & \frac{i}{n_1} \\ in_1 & 0 \end{bmatrix} = \begin{bmatrix} 1 & 0 \\ 0 & 1 \end{bmatrix}$$

Equation 3.46

Thus, the characteristic matrix of the assembly can be written as:

$$\begin{bmatrix} B \\ C \end{bmatrix} = \begin{bmatrix} 1 & 0 \\ 0 & 1 \end{bmatrix} \times \begin{bmatrix} 1 \\ n_m \end{bmatrix} = \begin{bmatrix} 1 \\ n_m \end{bmatrix}$$

Equation 3.47

Using Equation 3.45, it is possible to obtain the reflectance (R) and the transmittance (T) of the structure, being $R = 0.0426$ and $T = 1 - R = 0.9574$.

3.2 Optical filters design based on thin-films

3.2.1 Optical filters structure

In the present work, narrow bandpass optical filters were implemented, taking advantage of the constructive/destructive combination of a thin-film multilayer that produces simultaneously pass and rejection bands. The implemented optical filters are based on a *Fabry-Perot* interferometer structure.

The *Fabry-Perot* interferometer consists of two flat parallel mirrors (high-reflectance coatings) separated by a layer with a pre-defined thickness d_s, called resonance cavity [1, 4, 9, 10] - Figure 3.5.

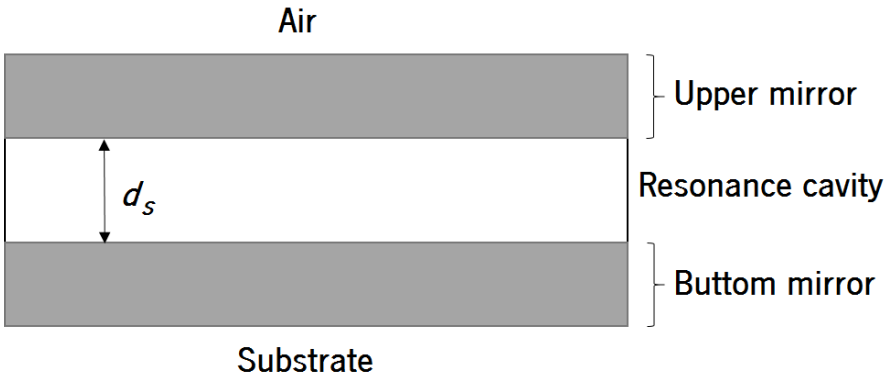

Figure 3.5 *Fabry-Perot* interferometer structure.

The parallel mirrors (or reflectors) of the *Fabry-Perot* interferometer can be implemented with metallic or dielectric films. In this work, dielectric materials were used (Figure 3.6), since they have some important advantages comparing with metallic ones. The most important is related with the high energy absorption rates of the metallic films, leading to a lower optical transmittance, especially if a narrow bandpass filter is desired. Dielectric films, contrarily, have low energy absorption rates, making its reflecting capacity just complementary to its transmitting capacity, and leading to the implementation of narrow bandpass optical filters with high transmittance at specific wavelengths [4, 9, 10].

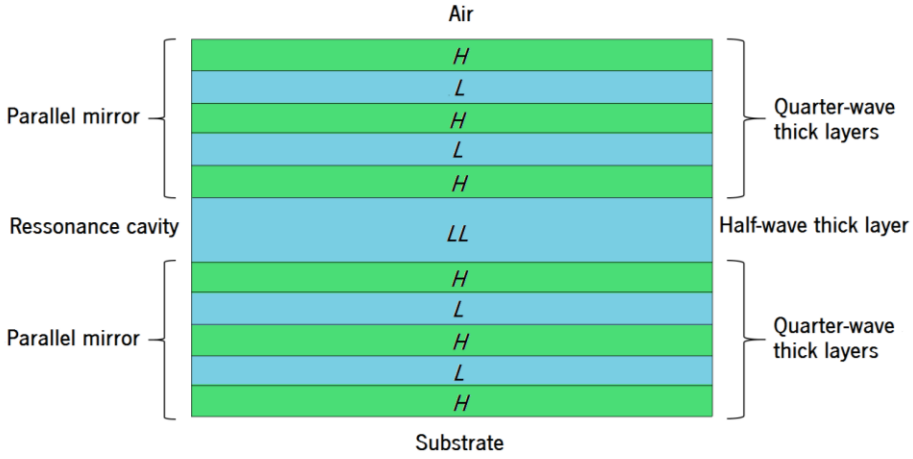

Figure 3.6 *Fabry-Perot* interferometer with dielectric layers (adapted from [4] by permission of Taylor and Francis Group).

In the resonance cavity there is a multiple-beam interference that causes the transmission of the filter to be very high at a narrow band of wavelengths around a wavelength for which the cavity is a multiple of one half wavelength thick. In a *Fabry-Perot* interferometer, when a light beam reaches the first surface of the resonance cavity (Figure 3.7) it is divided in two waves: one reflected (R1) and other transmitted into the resonance cavity. This last one will reach the second surface of the resonance cavity and again it will be divided in two light beams: one transmitted (T1) and the other reflected in the direction of the first surface of resonance cavity (R2). This process of successive reflections and transmissions will continue and will be repeated along the resonance cavity. The total transmitted light is the sum of all transmitted beams (T1, T2, T3 and T4) and the total reflected light is the sum of all reflected beams (R1, R2, R3 and R4) [1, 4].

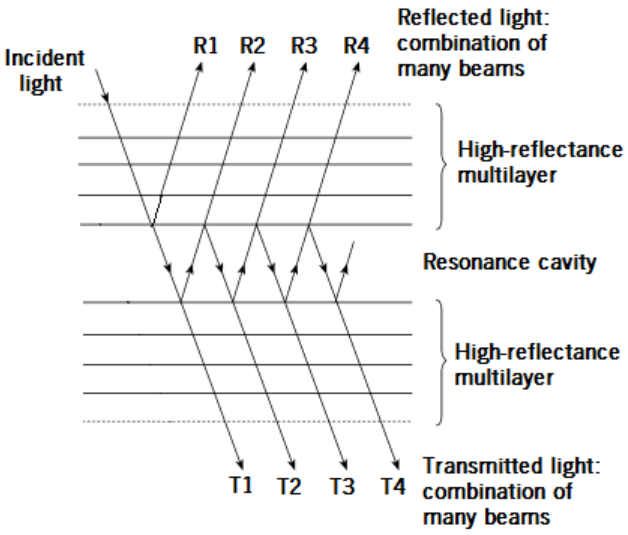

Figure 3.7 *Fabry-Perot* interferometer showing multiple reflections in the resonance layer (adapted from [4] by permission of Taylor and Francis Group, and [1]).

When the filter bandwidth is very narrow (i. e., the reflectance of the mirrors of *Fabry-Perot* interferometer is very high), a specific light beam is transmitted only if the thickness (d_s), the refractive index of the resonance cavity (n_s), the light incidence angle (θ) and the light wavelength (λ) satisfy the relation presented in Equation 3.48 [1]:

$$\delta = \frac{2\pi n_s d_s \cos\theta}{\lambda} = q\pi$$

Equation 3.48

where q is the filter interference order. Thus, the thickness of the resonance cavity determines the tuned wavelength [1, 9].

Considering a simple approach for the filters design, i. e., an interference order of 1 and a light incidence angle of 0° (normal light incidence), the separation between the mirrors (thickness of the resonance cavity of the *Fabry-Perot* interferometer - d_s), can be calculated using Equation 3.49 [1]:

$$d_s = \frac{\lambda}{2n_s}$$

Equation 3.49

where λ is the wavelength that is transmitted by the structure.

The thickness of the quarter-wave layers of the *Fabry-Perot* interferometer - d_t - (for transmission of the same wavelength) can be obtained using Equation 3.50 [1]:

$$d_t = \frac{\lambda}{4n_t}$$

Equation 3.50

where n_t is the refractive index of the quarter-wave layer.

Another important parameter that characterizes the selectivity of a filter is the value of FWHM, which is the bandwidth at half of the filter peak transmission [1].

Thus, in a *Fabry–Perot* interferometer the thickness of the resonance cavity determines the tuned wavelength, for the same mirrors films. Taking advantage of that, 16 optical filters,

designated simply by "*Fabry-Perot* optical filters", centered at specific spectral bands (ranging from 350-750 nm) previously considered relevant to extract the spectroscopic signals to GI tissue characterization [1, 2], were computationally designed using the software *TFCalc 3.5* supplied by *Software Spectra Inc*. During this step, the transmittance peak and the FWHM of the filters were analyzed. For the reported application, the intensity of the transmitted peak should be high, with at least twice the intensity of any noise peak that might appear in the considered spectral range. Concerning the FWHM, a value around 10 nm is enough, once the 16 required spectral bands are centered at 350, 370, 380, 400, 420, 450, 480, 510, 540, 560, 580, 600, 620, 650, 700 and 750 nm [11, 12].

The reported features give rise to divide the optical filters in three spectral regions: UV/Vis (350 nm – 450 nm), Vis (480 nm – 600 nm) and Vis/IR (620 nm – 750 nm). Within the same spectral region, the optical filters were centered at different spectral bands by adjusting only the thickness of the resonance cavity, keeping the same thicknesses of the mirrors films. This procedure minimizes the deposition time required for the optical filters fabrication. Therefore, the optical filter multilayer structure is composed by 11 thin-films with high and low refractive index materials, alternatively. The number of layers was chosen taking into account the optical filters performance during their design on *TFCalc 3.5*, concerning the FWHM and the transmittance peak [11, 12].

3.2.2 Optical filters materials

In an initial stage, TiO_2 and SiO_2 films were used as high and low refractive index materials [1], respectively, once they are compatible with CMOS fabrication, their refractive indices are almost wavelength independent in the visible range of the spectrum and they are commonly deposited by IBD (ion beam deposition), the process used for optical filters fabrication. However, it was checked (during the simulations on *TFCalc 3.5*) that this combination results in a poor optical filter performance below 420 nm, especially due to their low transmittance. As a result, other materials combinations (compatible with the IBD process) were considered, in order to improve the transmittance peak, keeping the selectivity of the filters. After several simulations, using different materials (such as MgO, Al_2O_3 and Ta_2O_5), but compatible with the IBD process, the combination MgO/TiO_2 was the best option for the UV/Vis range up to 400 nm, leading to an increase of the transmittance peak, keeping low values for the filters FWHM [11, 12].

The resonance cavity thickness and the thicknesses of the mirrors films, for each filter, are presented on Table 3.1 for the combinations of MgO/TiO_2 and of SiO_2/TiO_2. The thicknesses of the mirrors films (d_t) were calculated using as reference a central wavelength, in each specific group or region (400 nm for UV/Vis, 550 nm for Vis and 680 nm for Vis/IR), and Equation 3.50. The resonance cavity thicknesses (d_s) were obtained using Equation 3.49 or adjusted on the *TFCalc 3.5* software [11, 12].

Table 3.1 Optical filters in the UV/Vis, Vis and Vis/IR regions and respective layer thicknesses, with the combinations MgO/TiO_2 and SiO_2/TiO_2 (RC: Resonance Cavity), (reprinted from [11] with permission from OSA).

	Maximum transmittance peak wavelength (nm)																
	350	**370**	**380**	**400**		**420**	**450**	**480**	**510**	**540**	**560**	**580**	**600**	**620**	**650**	**700**	**750**
	Layer Thickness (nm)					Layer Thickness (nm)											
TiO_2	30				TiO_2	30		45						60			
MgO	57				SiO_2	68		95						117			
TiO_2	30				TiO_2	30		45						60			
MgO	57				SiO_2	68		95						117			
TiO_2	30				TiO_2	30		45						60			
MgO (RC)	–	**88**	**98**	**114**	**SiO_2 (RC)**	**153**	**174**	**140**	**163**	**184**	**199**	**214**	**229**	**189**	**211**	**248**	**285**
TiO_2	30				TiO_2	30		45						60			
MgO	57				SiO_2	68		95						117			
TiO_2	30				TiO_2	30		45						60			
MgO	57				SiO_2	68		95						117			
TiO_2	30				TiO_2	30		45						60			

3.2.3 Optical filters simulations

The simulation results (from *TFCalc 3.5*) for the approach on Table 3.1 (using the theoretical refractive indices available at *Sopra* database and [13]) are presented in Figure 3.8. At this phase, it was not possible to present the transmittance of the 350 nm optical filter, using the materials and thicknesses indicated in Table 3.1, since the transmittance obtained for this filter in the simulations was too small. This can be explained by the theoretical properties of the materials being used, namely their refractive indices [11, 12].

The simulation results of Figure 3.8 show that the chosen multilayer stack (five layers) of MgO/TiO_2 or SiO_2/TiO_2 thin-films for each dielectric mirrors and a MgO or SiO_2 layer for the resonance cavity (see Table 3.1), is the best option for the optical filters in terms of optical characteristics, feasibility and fabrication process. Moreover, those simulations allowed concluding that: (1) each spectral band has a high transmittance, close to 90%, except for the optical filter centered at 370 nm, explained by the theoretical refractive indices; (2) the FWHM average is around 6 nm; and (3) the interference of each neighbor peak is less than 10%. The performance of the optical filters could be improved by increasing the layers number of the dielectric mirrors, but the complexity of the fabrication process would also increase [11, 12].

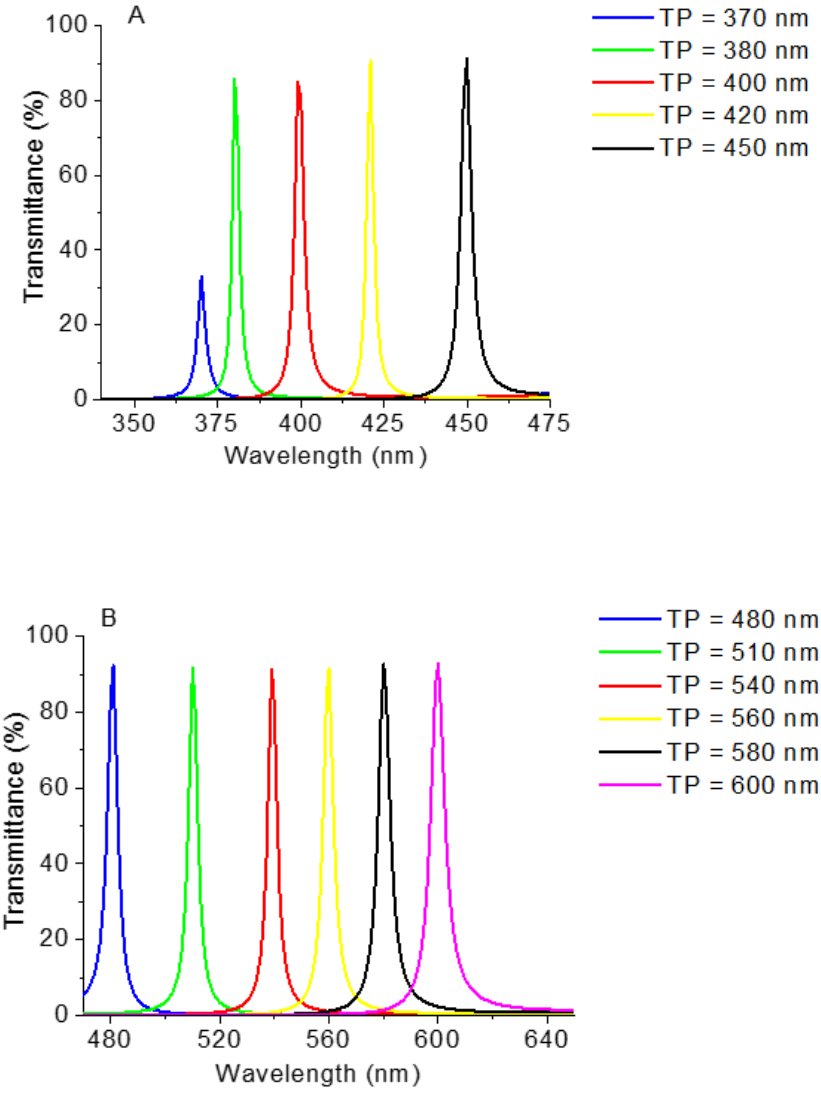

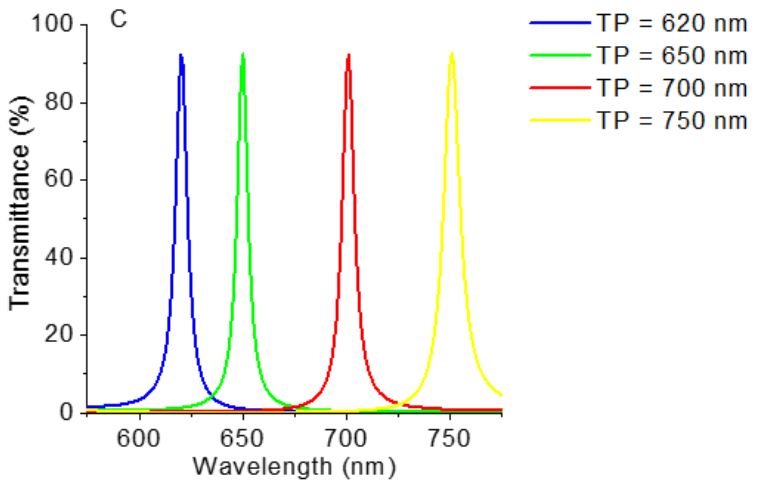

Figure 3.8 Transmittance spectra for the UV/Vis optical filters (A), Vis optical filters (B) and Vis/IR optical filters (C), obtained with the *TFCalc 3.5* simulations and using the theoretical refractive indices (TP: filter maximum transmittance peak wavelength), (adapted from [11] with permission from OSA).

3.3 Thin-films deposition process

The *Fabry-Perot* optical filters were deposited (at INESC-MN, Lisbon) by IBD in a *Nordiko 3000* tool equipped with a deposition and assist guns, in a broad beam architecture [14, 15] compatible with 150 mm diameter wafer deposition. Figure 3.9 illustrates the equipment geometry for a standard film deposition. The Xe ions created inside the deposition gun (by a RF [radio frequency] coil) were accelerated through a grid assembly into the target, at a pressure of 0.4 mTorr [11, 12].

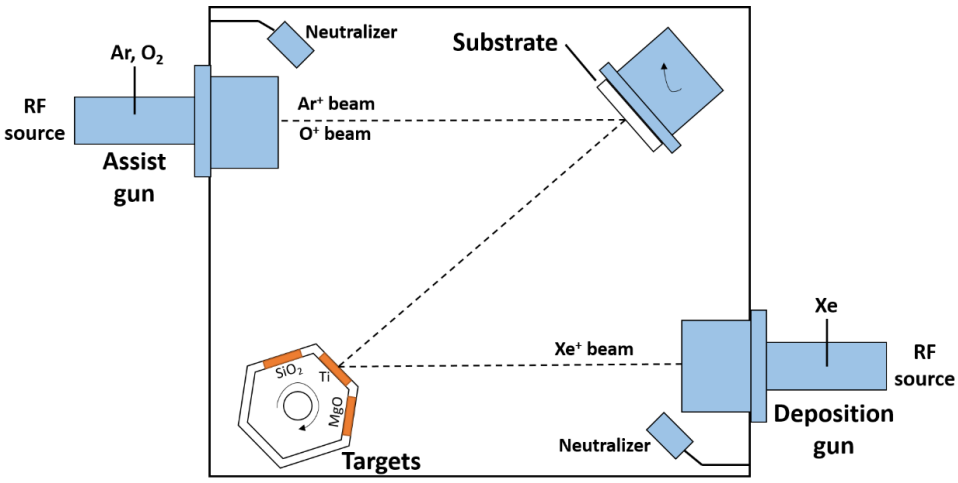

Figure 3.9 Geometry of the automated deposition system (*Nordiko 3000*) with a 6 target configuration, in order to allow sequential deposition of the films. The film thickness uniformity is ± 2% over 150 mm diameter area (reprinted from [11] with permission from OSA).

The SiO_2 and MgO films were prepared from ceramic targets. The Xe beam distortion caused by charging at the target surface was avoided with a neutralizer (*e*-beam), which is truly important for the SiO_2 and MgO deposition control, since it assures minimum beam deflection upon target surface charging and, therefore, a stable deposition rate along several hours of deposition. A deficient neutralization causes different SiO_2 and MgO films thicknesses across the multilayer, i.e., the bottom layers near the substrate have different thickness comparing with the top layers [11, 12].

The TiO_2 films were prepared from a metallic target, using a Xe beam and an assisted ion beam (Ar^+-O^+), extracted from the assist gun through a grid assembly, increasing the deposition pressure to 1.4 mTorr. The assist beam current was maintained low in order to minimize the material etching while depositing. Again, a neutralizer beam was used to avoid the assisted beam distortion [11, 12].

First, SiO_2, TiO_2 and MgO films were deposited on silicon substrates in order to calibrate the individual deposition rate and refractive index. Then, several SiO_2, TiO_2 and MgO thin-films with different thicknesses, close to the simulated ones (see Table 3.1), were deposited on the top of silicon wafers, in order to further measure the experimental refractive indices dependence on the wavelength and films thickness. These dependencies are crucial to the optical filter performance and cannot be disregarded, as they impact the maximum transmittance peak wavelength and the FWHM. The knowledge of the real optical properties of the films allows the adjustment of the previous simulations upon fabricating each optical filter in the specific spectral band. Therefore, the test samples have a range of thicknesses as close as possible to the ones previously simulated (see Table 3.1) [11, 12].

The variation of the refractive index with wavelength in the range of 350 nm to 750 nm was obtained by spectroscopic ellipsometry using a *nanofilm EP3-SE* ellipsometer from *Accurion GmbH* (at INL, Braga). Figure 3.10 shows the measured refractive index as a function of wavelength, for the different thicknesses, of the SiO_2, TiO_2 and MgO films, respectively. Moreover, the obtained thicknesses for each film were confirmed by profilometry, using a *Veeco Dektak 150* profilometer [11, 12].

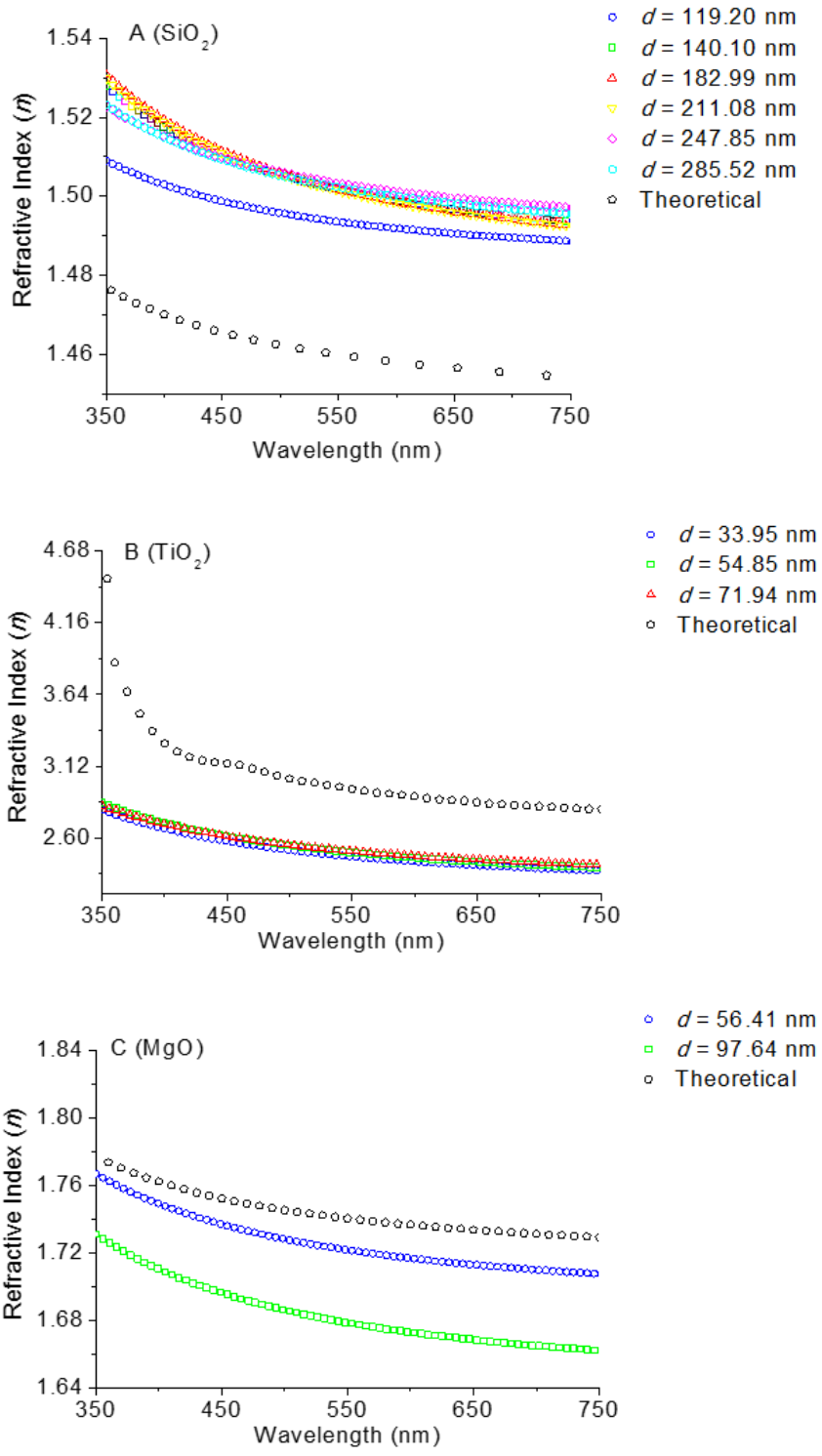

Figure 3.10 Comparison between the theoretical refractive indices and the ones obtained experimentally, for different thicknesses (*d*) of SiO_2 (A), TiO_2 (B) and MgO (C). The thicknesses are measured by profilometry (adapted from [11] with permission from OSA).

The measurements shown in Figure 3.10 allow concluding that there are significant differences between the refractive indices obtained experimentally and the theoretical ones used on the simulations. Moreover, the refractive index is dependent on the wavelength and also on the film thickness. The last variation is especially significant for the MgO and SiO_2 films. Notice that the theoretical refractive indices do not have either the thickness, or the deposition parameters dependences. The latter will extremely influence the optical characteristics of the films and, thus, must be obtained carefully. For the TiO_2 film for example, the differences between the experimental refractive indices and the theoretical ones are not unexpected, because assisted deposition allows tuning the oxygen content in the films, and creates amorphous films (while databases use their crystalline phase). As a consequence, the layers thicknesses to be used in the multilayer (*Fabry-Perot* structure) must be adjusted for maintaining the desired optical properties of the fabricated filters [11, 12]. That kind of adjustments will be explained on the next section (section 3.4).

3.4 Optical filters design adjustment

After the theoretical optical filters design using the theoretical refractive indices (section 3.2), the experimental refractive indices of SiO_2, TiO_2 and MgO (presented in Figure 3.10), were used in the *TFCalc 3.5* design software to adjust the layers thicknesses, in order to obtain the optical filters centered at the required 16 spectral bands (otherwise, it will be deviated). For a better observation of the refractive indices variation effect in the filters maximum transmittance peak and in the FWHM, Figure 3.11 compares the simulations for a filter (initially designed for 510 nm peak, see Table 3.1) with the same layers thicknesses and materials, but with different refractive indices – theoretical refractive indices and experimental refractive indices. As it can be observed, the use of the same materials and thicknesses, but with different refractive indices, causes a peak deviation of 15 nm and a larger FWHM [11, 12].

Thus, for each optical filter, the resonance cavity and the mirrors films thicknesses were adjusted according to the new refractive indices, measured experimentally (Figure 3.10) at different thicknesses. Table 3.2 presents this optimization and Figure 3.12 shows their simulation results. This time, it was also possible to present the transmittance of the 350 nm optical filter, using the experimental refractive indices of the MgO and TiO_2 materials, mainly due to the more constant experimental TiO_2 refractive index value in the UV/Vis region, when compared with the theoretical one [11, 12].

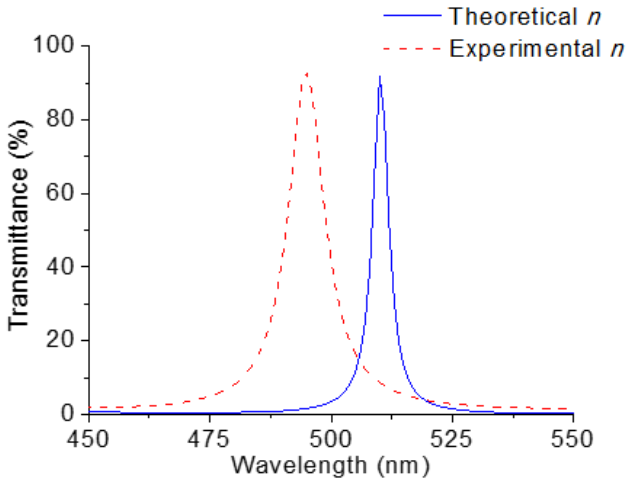

Figure 3.11 Transmittance spectra for an optical filter (simulated on the *TFCalc 3.5*) initially designed for 510 nm maximum transmittance peak. The two curves are obtained using the theoretical refractive indices (theoretical *n*) and the experimental refractive indices (Experimental *n*), maintaining the layers structure thicknesses and materials (adapted from [11] with permission from OSA).

The use of the experimental refractive indices allows achieving each spectral band with higher transmittance, close to 90%, even for the optical filter centered at 350 nm. However, the FWHM increased slightly (average around 13 nm), as might be expected since the experimental *n* value for TiO_2 is lower, being the mirror less metallic and more dielectric. Nevertheless, this FWHM increase is not critical for the described application. As it can be seen in Figure 3.12, the transmittance background noise is around 20%, except for the optical filter centered at 350 nm; and the interference of each neighbor peak is around 25%, except for the two filters centered at 370 nm and 380 nm, which is close to 40%. Therefore, despite the filters performance in terms of a narrow spectral bandpass is not as expected with the first theoretical simulations, they are still suitable for the application. The optical filters performance could be improved increasing the number of dielectric layers of the mirrors. However, the fabrication process complexity will also increase. Thus, it is important to ensure a compromise between the filters performance and the complexity inherent to the filters fabrication process [11, 12].

Table 3.2 Optical filters in the UV/Vis, Vis and Vis/IR regions and respective layer thicknesses, with the combinations MgO/TiO_2 and SiO_2/TiO_2, after the design adjustment (RC: Resonance Cavity), (reprinted from [11] with permission from OSA).

	Maximum transmittance peak wavelength (nm)																
	350	**370**	**380**	**400**		**420**	**450**	**480**	**510**	**540**	**560**	**580**	**600**	**620**	**650**	**700**	**750**
	Layer Thickness (nm)					Layer Thickness (nm)											
TiO_2	37				TiO_2	37		55						70			
MgO	57				SiO_2	67		92						114			
TiO_2	37				TiO_2	37		55						70			
MgO	57				SiO_2	67		92						114			
TiO_2	37				TiO_2	37		55						70			
MgO (RC)	**70**	**92**	**101**	**118**	**SiO_2 (RC)**	**149**	**177**	**122**	**149**	**175**	**192**	**209**	**227**	**175**	**202**	**243**	**287**
TiO_2	37				TiO_2	37		55						70			
MgO	57				SiO_2	67		92						114			
TiO_2	37				TiO_2	37		55						70			
MgO	57				SiO_2	67		92						114			
TiO_2	37				TiO_2	37		55						70			

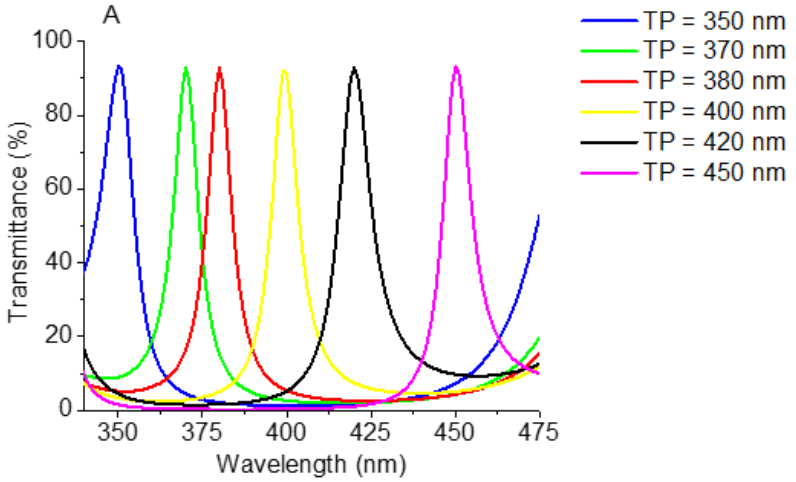

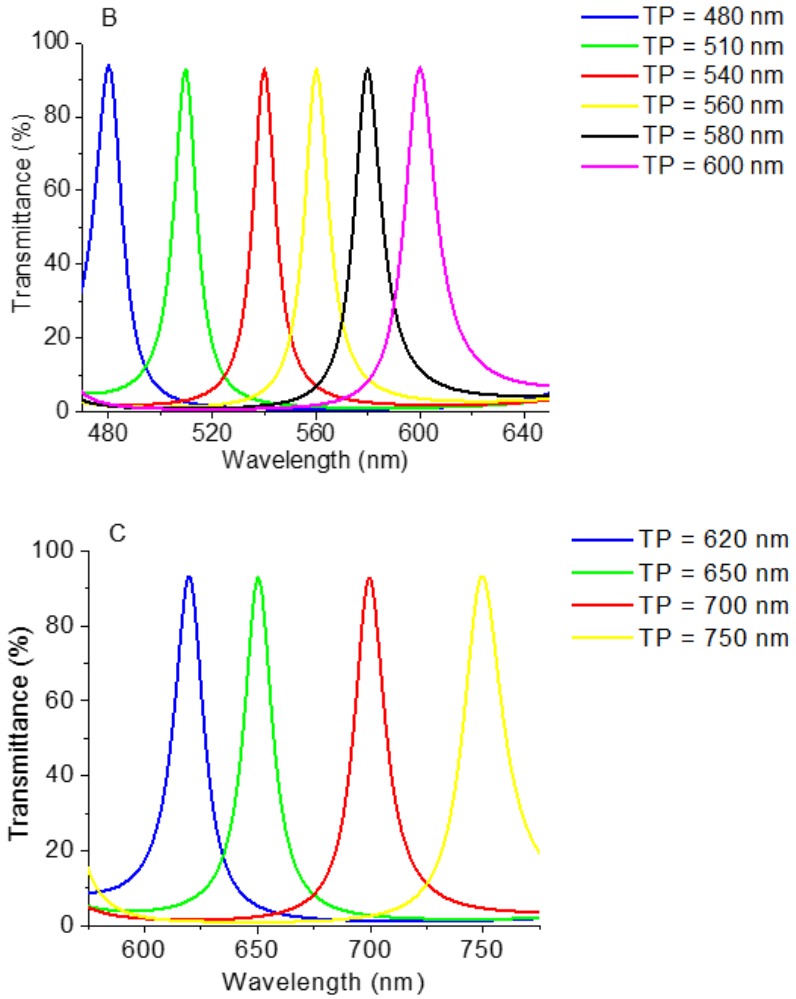

Figure 3.12 Simulated transmittance spectra for the UV/Vis optical filters (A), Vis optical filters (B) and Vis/IR optical filters (C) after the design adjustment, i. e., obtained with the *TFCalc 3.5* simulations and using the experimental refractive indices (TP: filter maximum transmittance peak wavelength), (adapted from [11] with permission from OSA).

3.5 Optical filters fabrication and characterization

After the layer thicknesses adjustment, the 16 optical filters were deposited, as described in section 3.3, on a borosilicate glass substrate with 0.7 mm thickness and 25 × 25 mm^2 area, adjusting the deposition time to obtain the thicknesses presented on Table 3.2. The optical transmittance of the borosilicate glass is higher than 90% in the required spectral band, 350 nm to 750 nm (Figure 3.13), making this substrate suitable for the optical filters fabrication and future characterization. Before the deposition, the substrate was ultrasonically cleaned with Alconox solution for 30 minutes, followed by another cleaning with deionized water and blown dry with compressed air gun [11, 12].

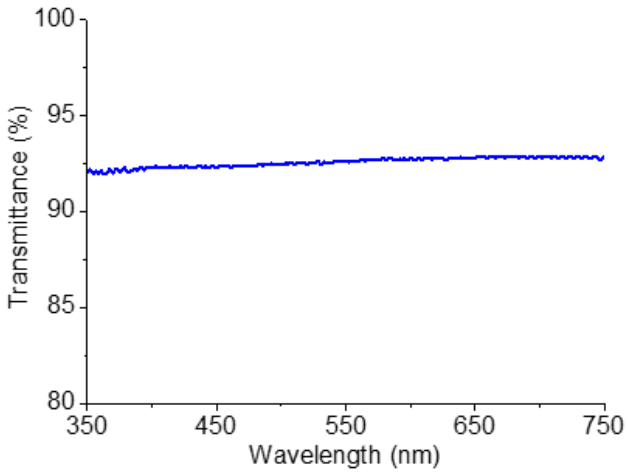

Figure 3.13 Experimental transmission curve of the borosilicate glass substrate measured using a commercial UV-Vis-NIR spectrophotometer (*Shimadzu UV-3101PC*).

The deposition of the 16 filters was performed using a combined process, where the first several multilayers are deposited without vacuum break for substrates with the same composition set (first mirror). Then, the samples are split (with vacuum break) for individual resonance cavity layer deposition. Finally, the top multilayers are again deposited upon combining several samples from the same set (second mirror) [11, 12].

Figure 3.14 shows the measured transmittance of the fabricated optical filters, using a commercial UV-Vis-NIR spectrophotometer (*Shimadzu UV-3101PC*). It can be observed that the optical transmittance is close to 80%, except for the filters initially designed for 350 nm and 370 nm [11, 12].

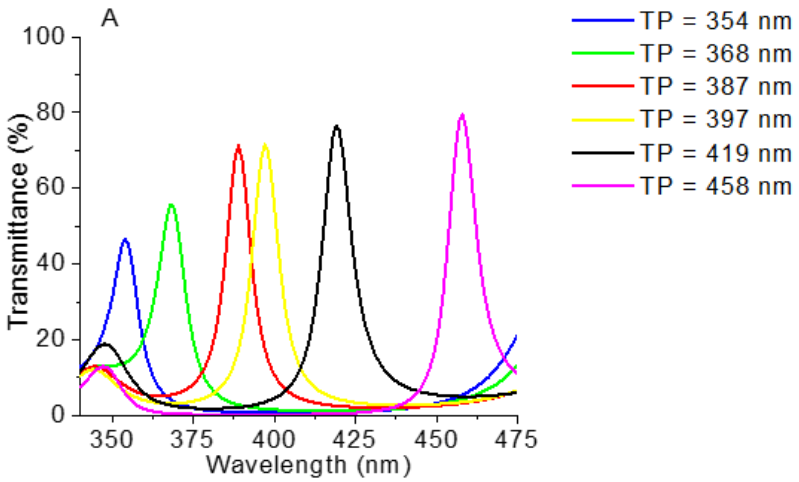

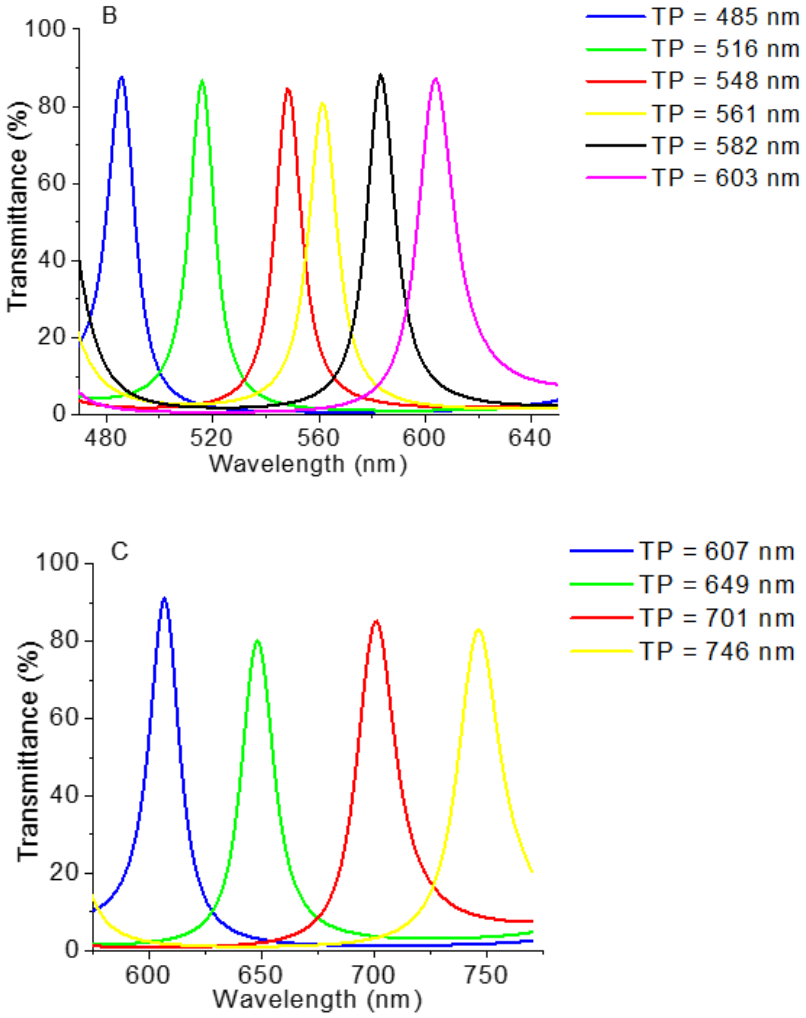

Figure 3.14 Transmittance spectra obtained experimentally for the UV/Vis fabricated optical filters (A), Vis fabricated optical filters (B) and Vis/IR fabricated optical filters (C), (TP: filter maximum transmittance peak wavelength), (adapted from [11] with permission from OSA).

Table 3.3 shows a comparison between the simulated and the fabricated optical filters, highlighting the maximum transmittance peak to better observe the deviations. Concerning the filters FWHM, its average is around 11 nm for the UV/Vis optical filters, 13 nm for the Vis optical filters and 20 nm for the Vis/IR optical filters. The transmittance background noise is around 20%, except for the filter centered at 582 nm, which is close to 40%; and the interference of each neighbor peak is around 25%, except for the two filters centered at 387 nm and 397 nm, which is close to 40%. The maximum peak deviation was 13 nm for the filter initially programmed for 620 nm [11, 12].

Table 3.3 Comparison between the simulated maximum transmittance peak and the one obtained experimentally for the fabricated optical filters (reprinted from [11] with permission from OSA).

Optical Filter	1	2	3	4	5	6	7	8	9	10	11	12	13	14	15	16
Maximum transmittance peak simulated (nm)	350	370	380	400	420	450	480	510	540	560	580	600	620	650	700	750
Maximum transmittance peak measured (nm)	354	368	387	397	419	458	485	516	548	561	582	603	607	649	701	746
Peak Deviation	4	-2	7	-3	-1	8	5	6	8	1	2	3	-13	-1	1	-4

Figure 3.15 shows photographs of some of the fabricated optical filters. It is important to refer that the photographs were obtained using a *Olympus CKX41* microscope (10×) with a *Olympus i-speed LT* camera and commercial optical wide bandpass filters (information in appendix I), in order to eliminate the second order effects of the fabricated optical filters far outside their main spectral region.

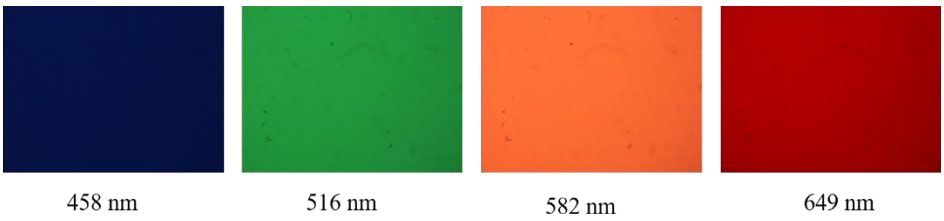

Figure 3.15 Photographs of some of the fabricated optical filters.

The optical filters FWHM could be improved increasing the number of the dielectric layers that form the mirrors. However, the complexity of the fabrication process in terms of deposition time and cost will also increase. An increase in the TiO_2 refractive index (*n* about 3.2) will also improve the FWHM (around 5 nm). The TiO_2 films deposited by IBD (and, in general, in all large area industrial deposition tools) are amorphous, which results in a refractive index lower than that of the crystalline phase. Therefore, increasing the TiO_2 refractive index would be possible upon crystallization of these materials using high temperature annealing, under high pressure of oxygen. Yet, not only this is incompatible with many wafer production lines, but also adds extra complexity

to the microfabrication process and increases the final cost. Thus, taking all these aspects into account, it is important to ensure a compromise between the desired filters performance and the complexity inherent to the filters fabrication process [11, 12].

In order to present a comparison between the fabricated filters and the available commercial ones, Appendix II presents some features of the commercial optical filters, i. e., optical properties under the 350-750 nm range (FWHM, transmittance), integration capability (thickness and area) and approximate cost (per area). Briefly, although bandpass optical filters are commercially available, their integration with the microfabricated chip is very limited, due to their large dimensions: diameter and thickness that round 12.5 mm (minimum) and 5 mm (minimum), respectively [16]. Thin-film deposition is an ultra-compact method to reduce the filter size to dimensions as low as hundreds of microns (0.1 × 0.1 mm^2). The same happens with the cost. It is expected that the proposed optical filters deposited on top of the photodiodes will cost about 0.07 €/mm^2 (against the commercial ones, which cost rounds between 0.1 €/mm^2 to 1 €/mm^2 [16]), particularly upon optimization was done, and a large number of wafers can be produced in a batch. Therefore, the possibility to integrate thin-film bandpass filters in a large scale production will have higher impact to reduce the final cost, size and performance, when comparing with mounting discrete filters externally on the chip [11, 12].

Additionally, some of the fabricated filters were characterized by SEM (scanning electron microscopy), using a *NanoSEM – Fei Nova 200* equipment (at SEMAT, University of Minho). Figure 3.16 displays SEM images showing the cross-section of the filters number 6 and number 8 presented on Table 3.3 (maximum transmittance peak wavelength at 458 nm and at 516 nm, respectively), with the layer thicknesses values measured by SEM. As it can be observed, there is a clear separation between the SiO_2 and TiO_2 thin-films. Moreover, there is a good film flatness along the entire analyzed area, ensuring the parallelism between the mirrors and the resonance cavity, which is crucial for the feasibility of the optical measurements [11, 12].

The total thickness of the same optical filters was also measured using the *Veeco Dektak 150* profilometer. Table 3.4 shows the obtained differences between the theoretical, the profilometry and the SEM measurements. As expected, the thicknesses obtained with profilometry are close to the ones obtained with SEM, but both are slightly deviated from the simulated ones. These deviations explain the maximum peak transmittance wavelength deviations that were obtained in the optical measurements (see Table 3.3) [11, 12].

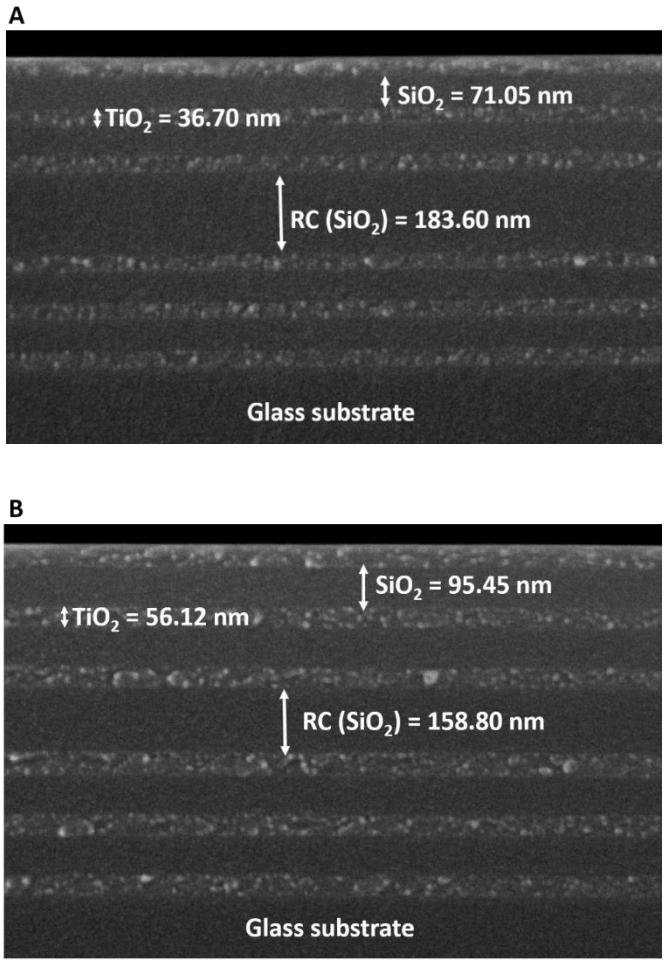

Figure 3.16 SEM image showing the cross-section of the 458 nm *Fabry-Perot* optical filter (A) and the 516 nm *Fabry-Perot* optical filter (B); magnification 200 000 × (RC: resonance cavity), (adapted from [11] with permission from OSA).

Table 3.4 Comparison between the optical filters theoretical thickness with the experimental one obtained by profilometry and by SEM (adapted from [11] with permission from OSA).

	Theoretical	Profilometry	SEM
Total thickness of filter number 6	667.00 nm	684.75 nm	688.00 nm
Total thickness of filter number 8	847.00 nm	869.57 nm	877.32 nm

Finally, in order to study the surface roughness of the IBD process, Figure 3.17 shows the surface 3-D map obtained by profilometry (in the *Dektak 150 Vision* software) of a thin-film of TiO_2. The thin-film is smooth (roughness average 2.27 nm), leading to conclude, once again, that the

thin-films have good flatness, ensuring the parallelism between the mirrors and the resonance cavity in the fabrication of the optical filters based on thin-films.

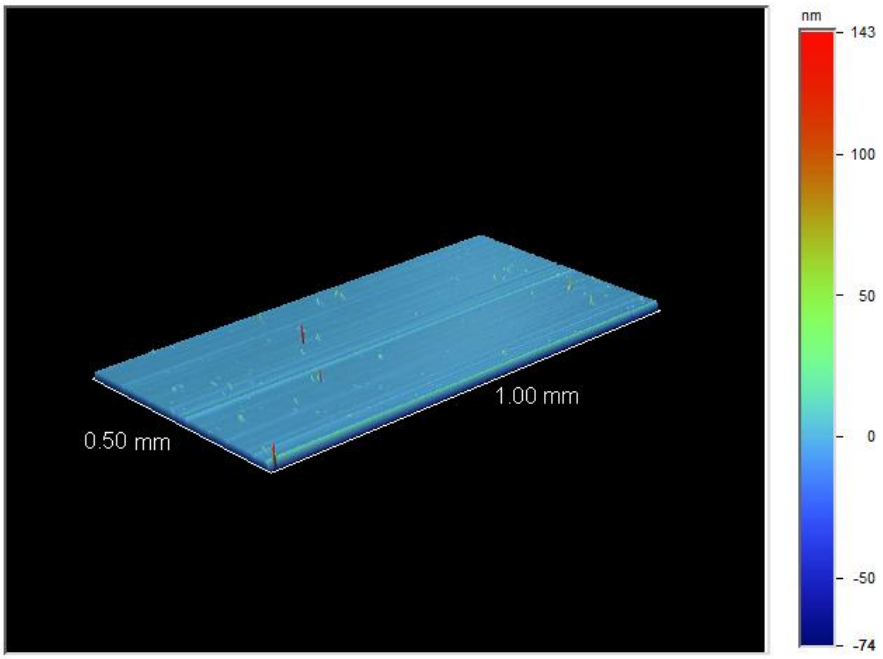

Figure 3.17 Surface 3-D map of a TiO_2 thin-film.

3.6 Conclusion

Along this chapter, the design, optimization and fabrication of 16 MgO/TiO_2 and SiO_2/TiO_2 based narrow bandpass optical filters were presented. Moreover, they were characterized through optical transmittance, selectivity capacity (FWHM), SEM and profilometry. The characterization results can explain (in part) the peak deviations, from the simulated ones, of the optical filters, since the results obtained with SEM are in accordance with the optical measurements. However, it is also important to note that, as previously emphasized, the materials refractive indices are affected by their thickness, introducing an additional constraint in programming the fabrication of optical filters centered at a desired spectral band. A more complete characterization of the refractive indices will be time consuming and cannot be performed for all the desired thicknesses. In fact, the design and fabrication of the optical filters is a challenging process, since there are several variables that need a precise control and constant adjustment, according to the measurements [11, 12].

Therefore, there must be a compromise between the filters performance needed for the described application, and the complexity inherent to the filters fabrication process. As a result, although the filters transmittance and performance in terms of a narrow transmission are slightly deviated from the simulated, the most important is to evaluate the filters performance and their viability to correctly extract the spectroscopic signals, specifically diffuse reflectance and fluorescence signals, performing spectroscopic measurements with phantoms representative of GI tissues with different compositions [11, 12]. This evaluation is presented on chapter 5.

References

[1] D. S. Ferreira, "Spectroscopy Systems for the Detection of Gastrointestinal Dysplasia", PhD, Escola de Engenharia, Universidade do Minho, Braga, Portugal, 2011.

[2] D. S. Ferreira, J. Mirkovic, R. F. Wolffenbuttel, J. H. Correia, M. S. Feld and G. Minas, "Narrow-band Pass Filter Array for Integrated Opto-Electronic Spectroscopy Detectors to Assess Esophageal Tissue", *Biomedical Optics Express,* vol. 2, pp. 1703-1716, 2011.

[3] G. Minas, "Microssistema Laboratorial Para Análise de Fluídos Biológicos", PhD, Eletrónica Industrial, Universidade do Minho, Braga, Portugal, 2004.

[4] H. A. Macleon, *Thin-film Optical Filters*, 3 ed. London, UK: Institute of Physics Publishing, 2001.

[5] M. Ferreira, *Óptica e Fotónica*. Lisboa: Lidel, 2003.

[6] G. Associates. (June, 2016). *Acoustic Glossary*. Available: http://www.acoustic-glossary.co.uk/sound-waves.htm

[7] F. R. Flory, *Thin Films For Optical Systems*. New York, USA: Marcel Dekker, 1995.

[8] P. H. Lissberger, "Optical applications of dielectric thin films", *Reports on Progress in Physics,* vol. 33, p. 197, 1970.

[9] G. Minas, R. F. Wolffenbuttel and J. H. Correia, "An array of highly selective Fabry-Perot optical channels for biological fluid analysis by optical absorption using a white light source for illumination", *Journal of Optics A: Pure and Applied Optics,* vol. 8, pp. 272-278, 2006.

[10] G. Minas, J. Ribeiro, J. S. Martins, R. Wolffenbuttel, and J. Correia, "An array of Fabry-Perot optical-channels for biological fluids analysis", *Sensors and Actuators A: Physical,* vol. 115, pp. 362-367, 2004.

[11] S. Pimenta, S. Cardoso, A. Miranda, P. De Beule, E. Castanheira and G. Minas, "Design and fabrication of SiO_2/TiO_2 and MgO/TiO_2 based high selective optical filters for diffuse reflectance and fluorescence signals extraction", *Biomedical Optics Express,* vol. 6, pp. 3084-3098, 2015.

[12] S. Pimenta, S. Cardoso, E. M. S. Castanheira and G. Minas, "Advances towards a miniaturized optical system for gastrointestinal cancer detection using diffuse reflectance and fluorescence spectroscopies", in *Gastrointestinal Cancers: Prevention, Detection and Treatment*, Volume 1, Chapter 13, A. K. Tyagi and S. Prasad (Editors), Nova Publishers, New York, 1 Dec. 2016; ISBN: 978-1-53610-168-3.

[13] M. Polyanskiy. (2008-2016, April, 2013). *Refractive index database*. Available: http://refractiveindex.info/

[14] S. Cardoso, R. J. Macedo, R. Ferreira, A. Augusto, P. Wisniowski and P. P. Freitas, "Ion beam assisted deposition of MgO barriers for magnetic tunnel junctions", *Journal of Applied Physics,* vol. 103, pp. 07A905:1-3, 2008.

[15] M. Davis, G. Proudfoot and D. Pearson, "Ion Beam Vacuum Sputtering Apparatus and Method", *Europeon Patent EP1212777,* 2001.

[16] *Commercial optical filters features.* Available: http://www.edmundoptics.eu/optics/optical-filters, https://www.thorlabs.com, http://search.newport.com (access date – April, 2015).

4 Microsystem design and implementation on CMOS technology

This chapter describes the design and implementation of the on-chip CMOS microsystem that incorporates: a silicon photodiodes matrix (4×4), in order to extract the spectroscopic signals in the relevant spectral bands selected by the optical filters; and the readout electronics, based on LF converters, for converting the photocurrent generated by the photodiodes in a digital signal for further processing. The photodiodes matrix and all the readout electronics was fabricated in a standard n-well 0.7 μm CMOS process using *AMIS Technology* from *Europractice*. The chapter also presents the performance of the photodiodes and of the LF converters.

4.1 Photodiodes matrix

A photodiode is an optical sensor that converts the light intensity (in this case, the light that is transmitted through the optical filter) into a photocurrent. A CMOS silicon photodiode allows the integration of its readout electronics and the respective optical filter, on a single chip and in a small silicon area. That way, the manufacturing costs are reduced and the use of conventional complex equipment, such as spectrograph and CCD detectors, which are used in the majority of the spectroscopy prototypes, is avoided. Moreover, CMOS technology allows low power consumption, which is a very important requirement for the reported application [1-3].

Therefore, the implemented photodetectors are CMOS silicon photodiodes. The CMOS technology allows the implementation of three vertical junction photodiodes: n-well/p-epilayer, p+/n-well and n+/p-epilayer - Figure 4.1. These photodiodes have the same operation principle but they differ in the pn junction depth, varying their quantum efficiency (how well it collects the incident light) as a function of the wavelength [4, 5].

The operation principle of a photodiode is based on the photoelectric effect, i. e., photons conversion in electron-hole pairs. When a high energy photon reaches the semiconductor, the photon can be absorbed by the electrons in the valence band, which can get sufficient energy to reach the conduction band. This happens when the photon energy exceeds the bandgap of the material between the valence and conduction bands (1.14 eV in the case of silicon). This process creates free electrons (negative carriers) in the conduction band and holes (positive carriers) in the

valence band. However, only a small part of the generated carriers contribute to the photocurrent, since the majority of the electrons generated in the conduction band recombine with the holes generated in the valence band. This phenomenon originates a region deprived of mobile carriers, a neutral region – depletion region – which opposes the movement of additional charges. As a result, when the high energy photons are absorbed near or into the depletion region, the generated electrons are brought back to the n type junction zone and the holes to the p type junction zone, before they can recombine. Thus, a photocurrent is generated, that is directly proportional to the intensity of the incident light [5].

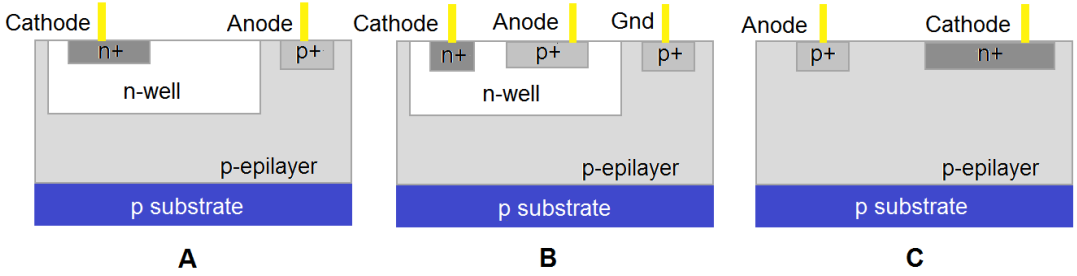

Figure 4.1 Cross section of the vertical photodiodes implemented by the CMOS technology: (A) n-well/p-epilayer; (B) p+/n-well; (C) n+/p-epilayer (adapted from [4] with permission from IEEE).

Photodiodes are characterized by two parameters: quantum efficiency (η) and responsivity (R_{Ph}). The first is defined as the percentage of the incident photons that contribute to the photocurrent. The second one is the ratio between the generated photocurrent and the incident optical power. These two parameters can be related by Equation 4.1 [5, 6].

$$\eta(\lambda) = \frac{R_{Ph} hc}{q_e \lambda}$$

Equation 4.1

where h is the Planck constant, c is the light velocity in vacuum, q_e is the electron charge and λ is the incident light wavelength.

The quantum efficiency of a photodiode is a function of the light wavelength ($\eta(\lambda)$). The absorption of light in silicon in the visible range of the spectrum is wavelength dependent, since the radiation with short wavelengths is absorbed in the silicon surface, and the radiation with long wavelengths is absorbed in the deeper part. This effect is caused by the wavelength dependency

of the silicon absorption coefficient ($\alpha_{silicon}$) (Figure 4.2), and gives rise to the fact that the penetration depth of light in silicon ($d_{silicon}$) is also wavelength dependent – Equation 4.2. Thus, a photodetector could be programmed to have a better efficiency in different wavelengths, changing the junction depth. However, in a standard CMOS process and using pn junction photodiodes, the pn junction depth is fixed and cannot be altered. As a result, considering the visible spectrum, the blue light is more efficiently collected by a shallower junction (p+/n-well or n+/p-epilayer) and the red light by a deeper junction (n-well/p-epilayer). Figure 4.3 shows the typical spectral response (deduced by Moini [7]) of each type of vertical photodiode implemented by the CMOS technology [4, 5].

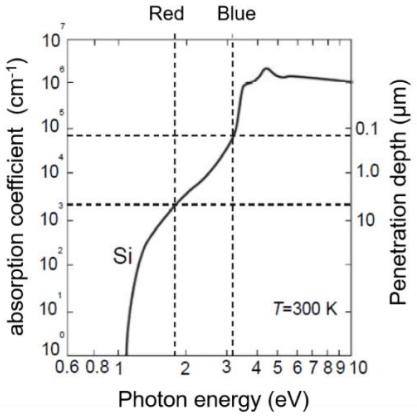

Figure 4.2 Absorption coefficient and penetration depth of light in silicon (adapted from [5]).

$$d_{silicon}(\lambda) = \frac{1}{\alpha_{silicon}(\lambda)}$$

Equation 4.2

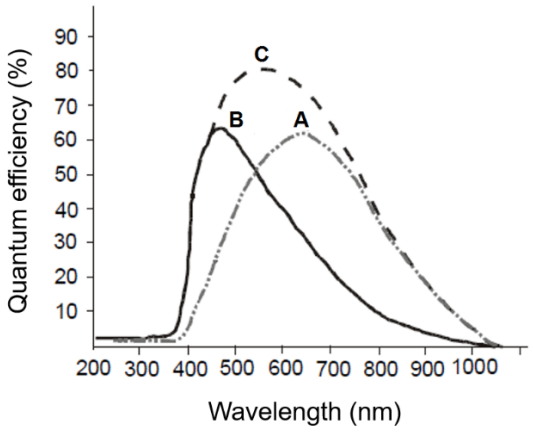

Figure 4.3 Quantum efficiency of the three types of vertical photodiodes implemented by the standard CMOS technology: (A) n-well/p-epilayer; (B) p+/n-well; (C) n+/p-epilayer (adapted from [5]).

Since the main objective of this thesis is the extraction of signals between 350 nm and 750 nm, the chosen photodiodes for the matrix will be based on n+/p-epilayer type, due to their wider spectral response, as it can be seen on Figure 4.3.

Figure 4.4 presents the layout of the photodiodes matrix extract from the *L-Edit* software from *Tanner EDA*. Each photodiode has as active area of 100 × 100 μm^2. Figure 4.5 shows the cross-section of each n+/p-epilayer photodiode implemented on the 4×4 matrix. The photodiodes matrix were implemented through a double-metal, single-polysilicon, 0.7 µm n-well CMOS process using *AMIS Technology* from *Europractice*.

The photodiodes junction depth cannot be altered, but their quantum efficiency can be improved by an appropriate arrangement of the three dielectric layers on top of each photodiode surface (first oxide, second oxide and overlayer) that act as a thin-film interference filter. Fulfilling the technology rules from the CMOS process, the design is restricted to the combinations of those three dielectric layers. However, fulfilling also the *AMIS Technology* rules, the first and second oxide must be kept, as presented in Figure 4.5. In this technology, the thickness of the first oxide above the photodiode is 660 nm, the second oxide 600 nm and the overlayer used for scratch protection is 1000 nm thick, approximately [8].

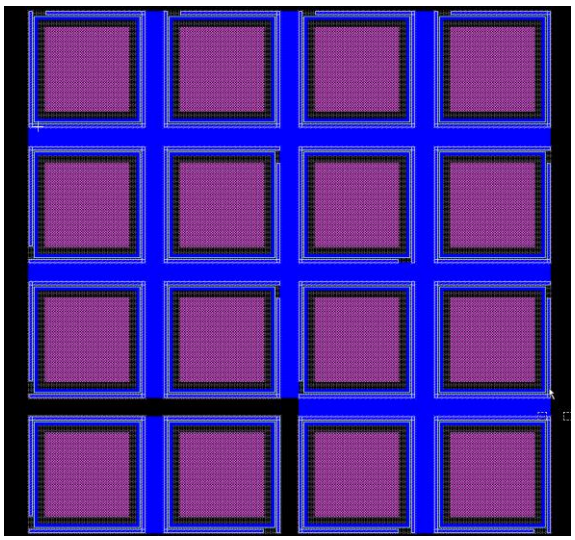

Figure 4.4 Layout of the 4×4 photodiodes matrix of the implemented chip.

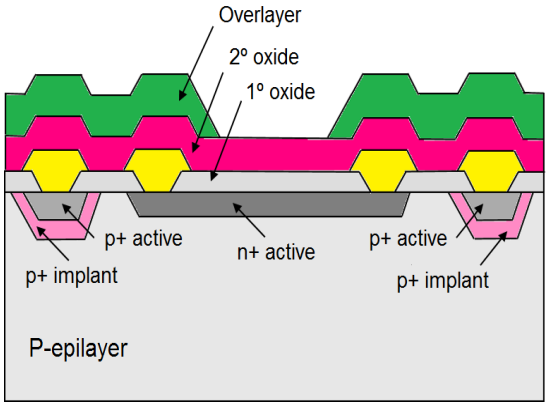

Figure 4.5 Cross-section of each fabricated n+/p-epilayer photodiode (not scaled). In the *AMIS Technology* (from *Europractice*) layout, the p+ implant mask is designed, while the n+ implant mask is not designed once the process knows that where it is an active mask without p+ implant, it will be an n+ implant (adapted from [8]).

Figure 4.6 shows a SEM image of the implemented 4×4 photodiodes matrix, obtained used a *JEOL JSM-6010LV* SEM instrument (at 3B's Research Group, University of Minho).

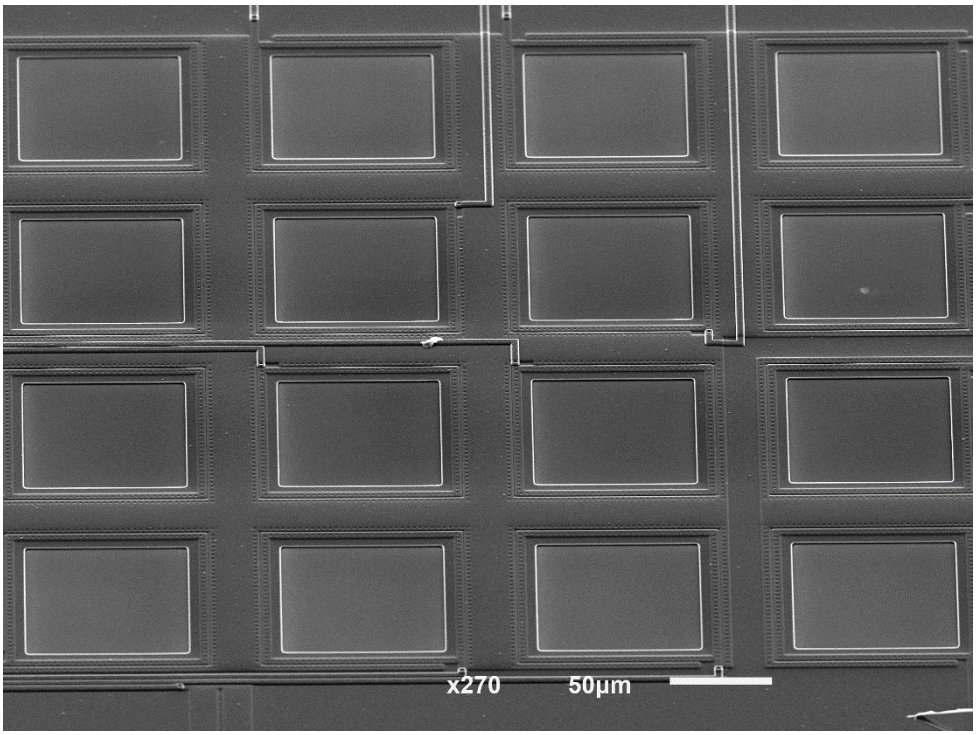

Figure 4.6 SEM image of the 4×4 photodiodes matrix (45° tilt).

Two of the photodiodes in the matrix are assessable at the implemented chip pinout, which makes possible their spectral characterization, using as reference a commercial photodiode (*Hamamatsu S1336-5BQ*). For the spectral characterization an optical setup was used (Figure 4.7)

comprising a quartz tungsten halogen lamp at 200 W, a picoammeter to measure the photodiodes current (*Keithley 487*), a monochromator (*Newport 74125*), an optical fiber to direct the light to the photodiodes (*Newport 77563*) and, finally, the implemented chip that contains the photodiodes or the commercial photodiode used as reference (not presented on Figure 4.7). In the characterization, this commercial photodiode has a pinhole on its top with approximately 100 µm diameter. The use of the pinhole on the commercial photodiode is essential to ensure that the optical power is the same for all the photodiodes, ensuring the accuracy of the obtained results.

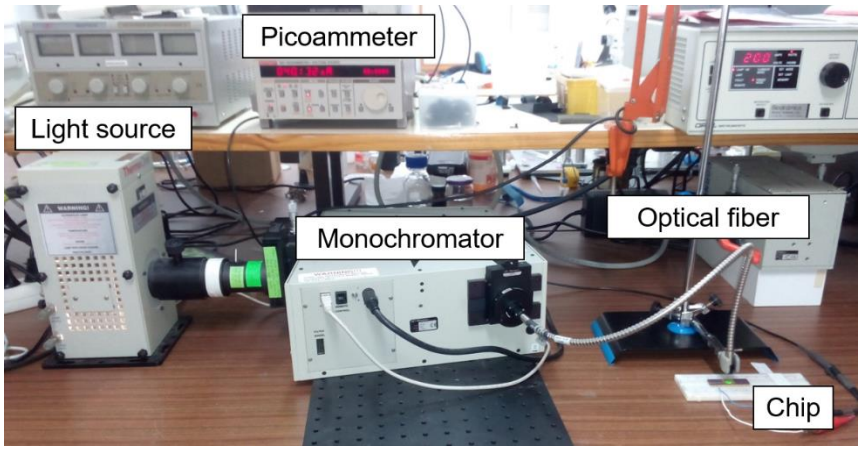

Figure 4.7 Optical setup used for the photodiodes spectral characterization.

Figure 4.8 shows the currents obtained for the two n+/p-epilayer photodiodes and for the commercial photodiode with the pinhole.

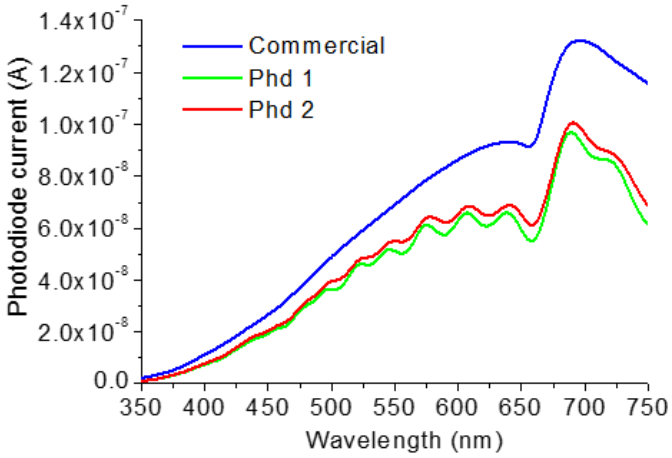

Figure 4.8 Photodiode currents obtained with the fabricated photodiodes of the matrix (Phd 1 and Phd 2) and the commercial photodiode used as reference (Commercial).

Since the responsivity of the commercial photodiode is known (data in appendix III), is possible to obtain the optical power incident in each photodiode (Figure 4.9). With the optical power (OP), it is possible to obtain the responsivity (R_{Ph}) of each fabricated photodiode (Figure 4.10), using the following expression:

$$R_{Ph} = \frac{I}{OP}$$

Equation 4.3

where I is the measured current for each photodiode, presented at Figure 4.8.

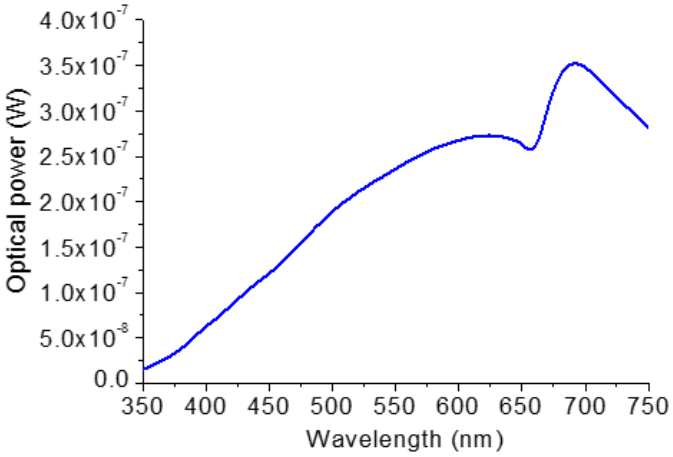

Figure 4.9 Optical power incident in each fabricated photodiode.

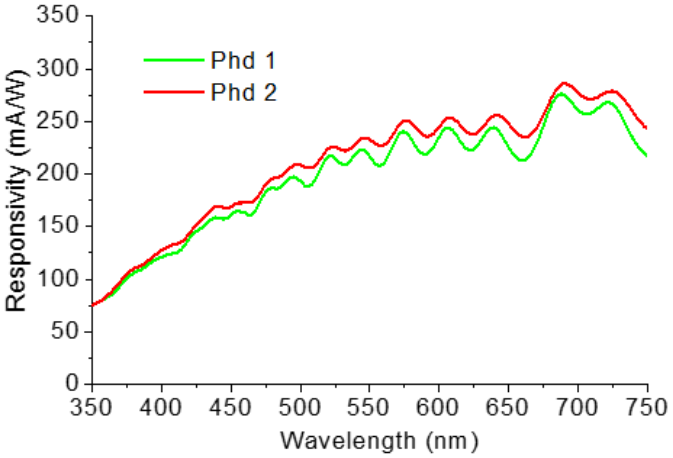

Figure 4.10 Responsivity of the fabricated photodiodes.

The quantum efficiency of each photodiode can be obtained by Equation 4.1 – Figure 4.11.

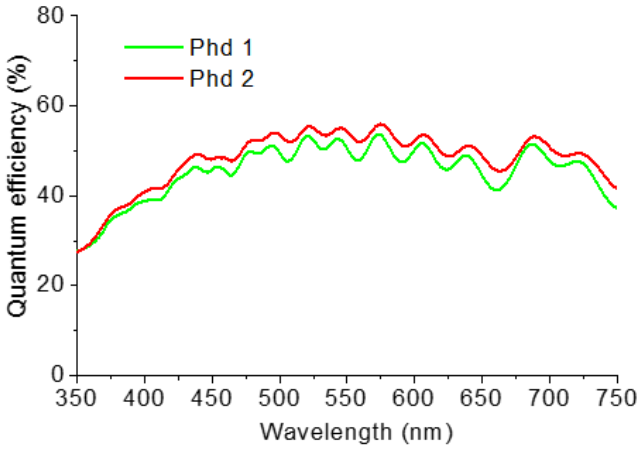

Figure 4.11 Quantum efficiency of the fabricated photodiodes.

Concerning the shape of the responsivity and quantum efficiency curves, they are affected by the two dielectric layers of SiO_2 above the photodiode (first and second oxides). The two dielectric layers above the photodiode introduce a wavelength dependence (fluctuations), when compared with the transmittance without the dielectric layers, as shown in [4] and on Figure 4.12, which shows a simulation (on the software *TFCalc 3.5*) of the optical effect of those two dielectric layers above a photodiode. However, in the same CMOS run, these dielectric layers have the same properties, such as thickness and oxide concentration. Moreover, for this application, these wavelength dependences will not affect the spectroscopic measurements (diffuse reflectance and fluorescence), because the diffuse reflectance measurements are relative (consider a reference for 100% reflectance) and the fluorescence spectral shape is not affected by these fluctuations, as shown in chapter 5 [8, 9].

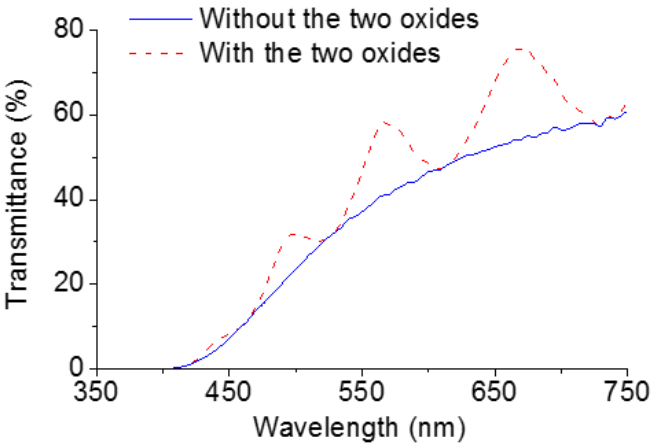

Figure 4.12 Optical transmittance simulation showing the effect of the two dielectric layers above a photodiode, using the software *TFCalc 3.5*.

The behavior of one of the photodiodes (Phd1) at several temperatures was also studied, measuring its current as a function of wavelength, at a medium (incubator) with four different temperatures: 22 °C, 37 °C, 40 °C and 42 °C, approximately, and using the equipment describe on Figure 4.7. Figure 4.13 shows the measured currents at these four temperatures.

As it can be seen, a rise of temperature increases the photodiode current, as expected, once the responsivity of a silicon photodiode is temperature dependent [10]. This variation can be avoided in the final microsystem using a temperature calibration circuit.

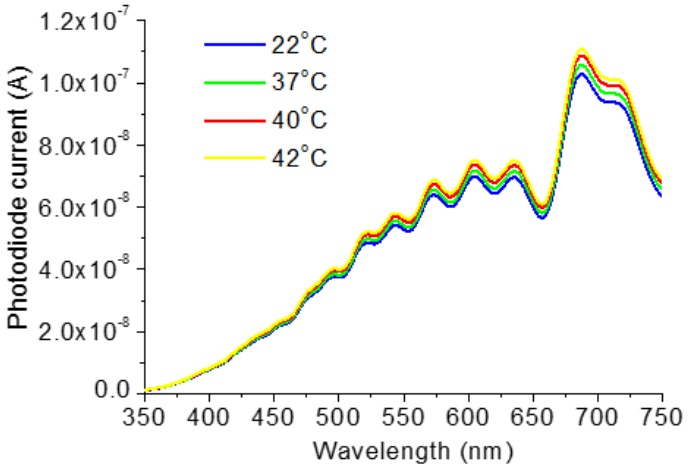

Figure 4.13 Photodiode current as a function of wavelength for four different temperatures of the medium (22 °C, 37 °C, 40 °C and 42 °C).

4.2 Readout electronics

4.2.1 Light-to-frequency converter

Using a LF converter, it is possible to convert a photocurrent in a digital signal proportional to the light intensity that reaches a photodiode. Each photodiode of the matrix must have its LF converter integrated in the same die, ensuring the signals acquisition with the same illumination conditions.

Figure 4.14 shows a representative scheme of one photodiode and its respective LF converter. Since the LF converters for all photodiodes are equal, a general explanation will be presented. The LF converter was developed by a group colleague, R. G. Correia [8, 11].

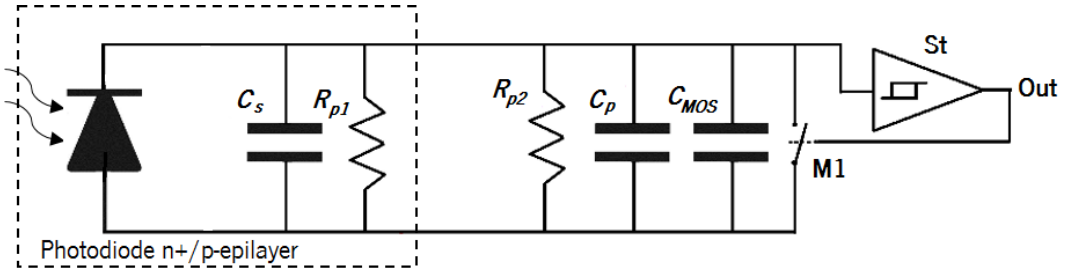

Figure 4.14 Representative scheme of one photodiode and its respective readout electronic circuit (adapted from [8]).

The total capacitance (photodiode capacitance (C_s), parasitic capacitance (C_p) and design capacitance (C_{MOS})) is used as storage element. The capacitors charging and discharging are controlled by a St (schmitt trigger). When the capacitors terminals voltage is higher than 2.4 V, the St output (Out) is at a high logic level, leading to the capacitors discharging, through M1, until the capacitors terminals voltage reaches 1.0 V, which causes St output to switch to a low logic level, charging again the capacitors and repeating the cycle. The main advantage of using a St, instead of a standard comparator, is its noise immunity, which improves the switch between high and low levels. The resistor R_{p1} represents the photodiode resistance and R_{p2} represents the wire resistance from the photodiode to the St connection [8].

Figure 4.15 shows the schematic circuit of the implemented LF converter. The photodiode current (**Input** in Figure 4.15) charges the capacitor (C_{MOS} in Figure 4.14), which is implemented by the drain to source connection of the PMOS transistor, M2 in Figure 4.15. When the capacitor terminals voltage exceeds 2.4 V (e.g., when **Vcap** in Figure 4.15 and Figure 4.16 reaches 1.1 V), the St (transistors M3 to M8) generates a low level pulse signal (**TriggerDischarge** in Figure 4.15 and Figure 4.16), leading to the capacitor discharging, through M1, operate it, and putting a voltage of 2.5 V in the M2 gate (**Vcap**), charging again the capacitor and repeating the cycle. Moreover, the pulse **TriggerDischarge** (see Figure 4.15) operates in the clock signal of a Flip Flop D (FFD in Figure 4.15). FFD is responsible to ensure a duty cycle of 50% in the LF output signal (**Output** in Figure 4.15 and Figure 4.16). Figure 4.17 highlights the capacitor discharging [8].

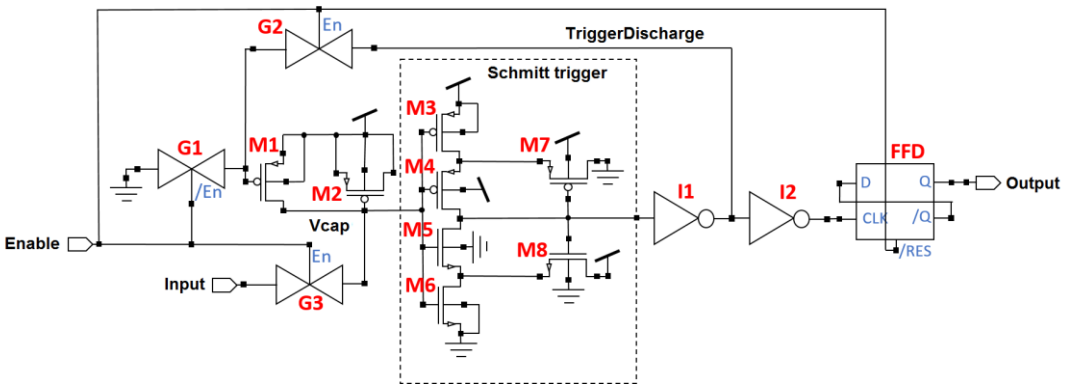

Figure 4.15 Schematic circuit of the implemented LF converter. Its power supply (V_{DD}) is 3.5 V. The Schmitt trigger comparator reference values are 2.5 V and 1.1 V, approximately, in the **Vcap** terminal (adapted from [8]).

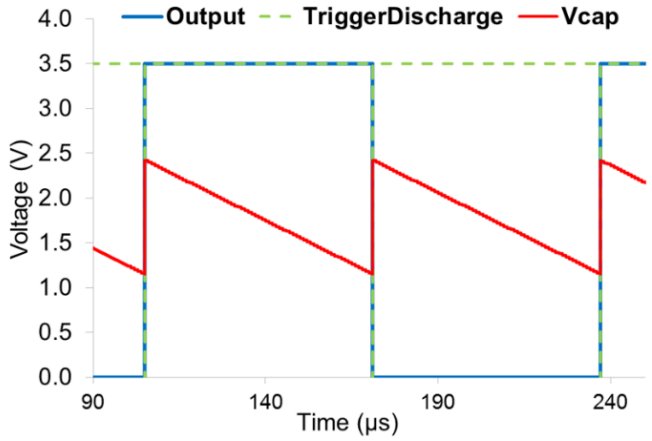

Figure 4.16 Simulated signals (from software *S-Edit* from *Tanner EDA*) of the LF converter with an input current (**Input** in Figure 4.15) of 100 nA: **Vcap** signal is the M2 gate voltage; **TriggerDischarge** signal is the St output signal responsible to discharge the M2 capacitor; **Output** signal is the LF output signal with a duty-cycle of 50% and a frequency proportional to the photodiode current (adapted from [8]).

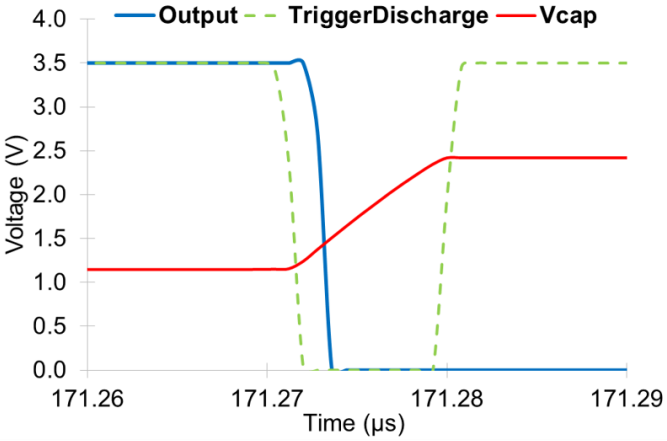

Figure 4.17 Detailed region of Figure 4.16, highlighting the capacitor discharging (adapted from [8]).

The transmission gates presented in Figure 4.15 (G1 to G3) are responsible for connecting and disconnecting the circuit. When the LF converter is turned off, G1 is on, connecting M1 gate to Ground and leading all M2 terminals to V_{DD}. This ensures that the capacitor (M2) remains discharged, ensuring also that when it (M2) starts a new conversion it is started in a known state. G2 ensures the functionality of the general circuit, avoiding short-circuit between the Schmitt trigger output and the Ground imposed by G1. G3 is needed in order to disconnect the photodiode from the converter input, when none conversion is needed [8].

The M2 capacitance is 0.2 pF, which is calculated using Equation 4.4 [8, 12]:

$$C_{MOS} = C_{0x} \times W \times L$$

Equation 4.4

where W and L are the gate width (10 μm) and length (10 μm), respectively; and C_{0x} is the PMOS gate capacitance per square meter, which can be calculated using Equation 4.5 [8, 12]:

$$C_{0x} = \frac{\varepsilon_{0x}}{t_{0x}}$$

Equation 4.5

where ε_{0x} is the permittivity of the silicon dioxide (3.45×10^{-11} F/m [13]); and t_{0x} is the thickness of the gate oxide layer (17 nm).

The capacitor M2 charging time (t_{MOS}) can be obtained using Equation 4.6 [8, 14, 15]:

$$\Delta V_{MOS} = \frac{1}{(C_s + C_p + C_{MOS})} \int_0^{t_{MOS}} I(\tau) d\tau$$

Equation 4.6

where ΔV_{MOS} is the difference between the highest and lowest potential in the M2 capacitor, which is 1.4 V (see Figure 4.16, **Vcap** signal); and I is the current supplied by the photodiode. Solving Equation 4.6, it is possible to obtain Equation 4.7 [8]:

$$t_{MOS} = \frac{\Delta V_{MOS} \times (C_s + C_p + C_{MOS})}{(I + \frac{V(t_{MOS})}{(R_{p1} // R_{p2})})}$$

Equation 4.7

where $V(t_{MOS})$ is the voltage in the M2 gate, which is 1.1 V (allowing M2 charging). The total capacitance $(C_s + C_p + C_{MOS})$ and $R_{p1} // R_{p2}$ could be obtained experimentally, with the LF converter and considering a system of equations based on Equation 4.7 [8].

Finally, the energy stored (ΔEC) in the capacitor M2, responsible for generate each **TriggerDischarge** signal (Figure 4.16) is calculated using [8, 16]:

$$\Delta EC = \frac{1}{2}(C_s + C_p + C_{MOS})\Delta V_{MOS}^{\ 2}$$

Equation 4.8

The main advantage of using this topology, when compared with some LF converters implemented in literature [4, 17], is its noise immunity, good repeatability and robustness, once it is based mainly in digital electronics. Moreover, for the required application, where a converter per photodiode is required at a small area, this topology is the best choice [8].

Figure 4.18 presents the layout of a LF converter extract from the *L-Edit* software (from *Tanner EDA*). Each LF has an area of 250 × 70 μm², approximately [8]. The LF converters were implemented through a double-metal, single polysilicon, 0.7 μm n-well CMOS process using *AMIS Technology* from *Europractice*.

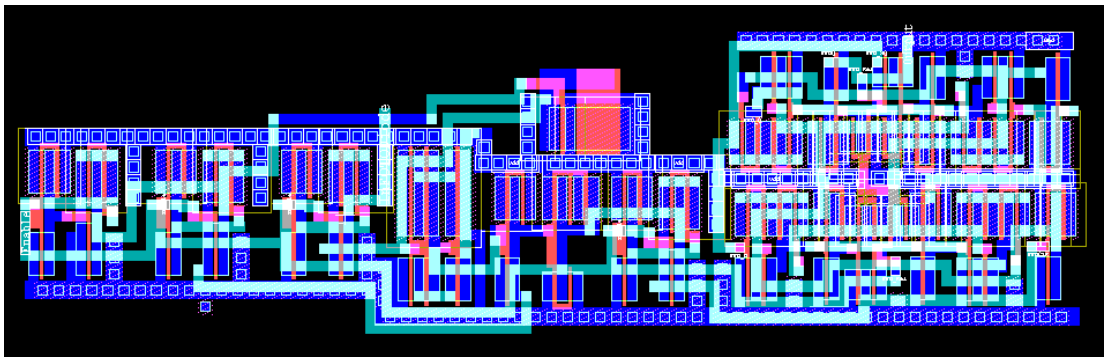

Figure 4.18 Layout of the LF converter of the implemented chip.

Figure 4.19 shows a SEM image of the 16 implemented LF converters (one for each photodiode), obtained used a *JEOL JSM-6010LV* SEM instrument (at 3B's Research Group, University of Minho).

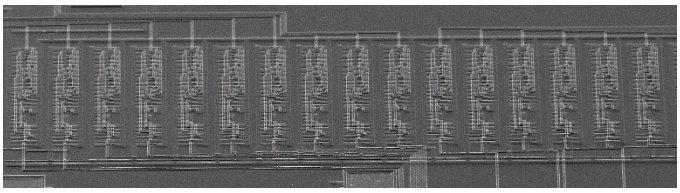

Figure 4.19 SEM image (x55) of the LF converters implemented on the chip (45° tilt).

4.2.2 Light-to-frequency converter: experimental tests

Taking into account one of the photodiodes previously characterized (Phd 1) and its respective LF converter, experimental tests were performed using a light source directly incident at the photodiode and measuring the output frequency.

The optical setup was based on the use of a quartz tungsten halogen lamp at different powers (200 W, 160 W, 120 W, 80 W and 40 W), a monochromator (*Newport 74125*), an optical fiber to direct the light to the photodiode (*Newport 77563*), a picoammeter to measure the photodiode current (*Keithley 487*), a DC power supply (*Mastech HY3005D-3*) at 3.5 V and a microcontroller to acquire the output frequency of the LF converter (*stm32vl discovery*).

Figure 4.20 shows the photodiode current at different light source powers, measured between 350 nm and 750 nm in steps of 10 nm. Figure 4.21 shows the respective output frequency for the same photodiode currents. As it can be seen, the shape of the curves are similar, as expected, since the higher is the photodiode current, the higher is the output frequency.

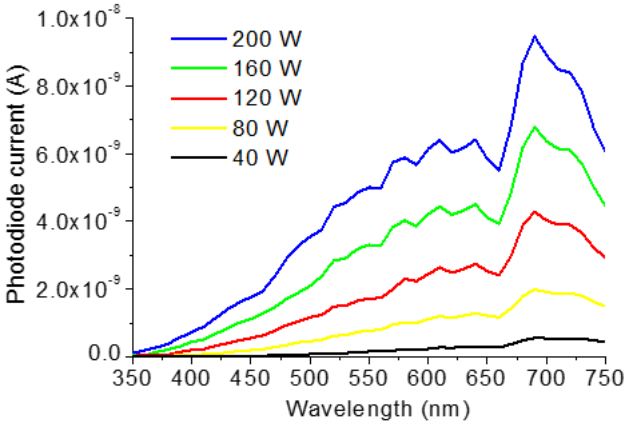

Figure 4.20 Photodiode currents for different light source powers.

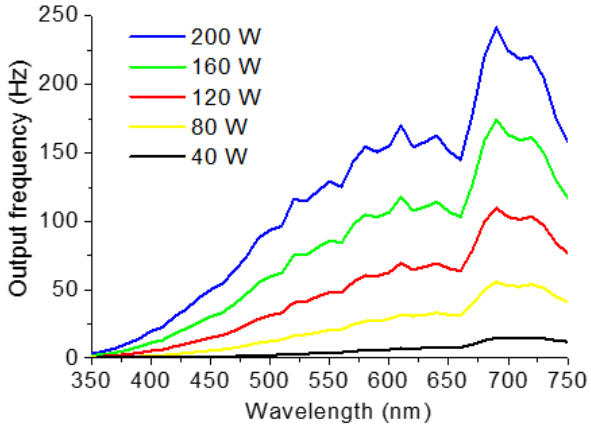

Figure 4.21 Output frequencies for different light source powers.

In order to evaluate the LF converter linearity, Figure 4.22 presents the frequency as a function of photodiode current for three fixed wavelengths (450 nm, 550 nm, and 700 nm), covering all the desired spectral range, blue zone (450 nm), a central wavelength (550 nm) and the wavelength at which the used equipment has its maximum efficiency (700 nm). The different photodiode currents were obtained directing a variable intensity monochromatic light, as previously presented in Figure 4.20 and Figure 4.21.

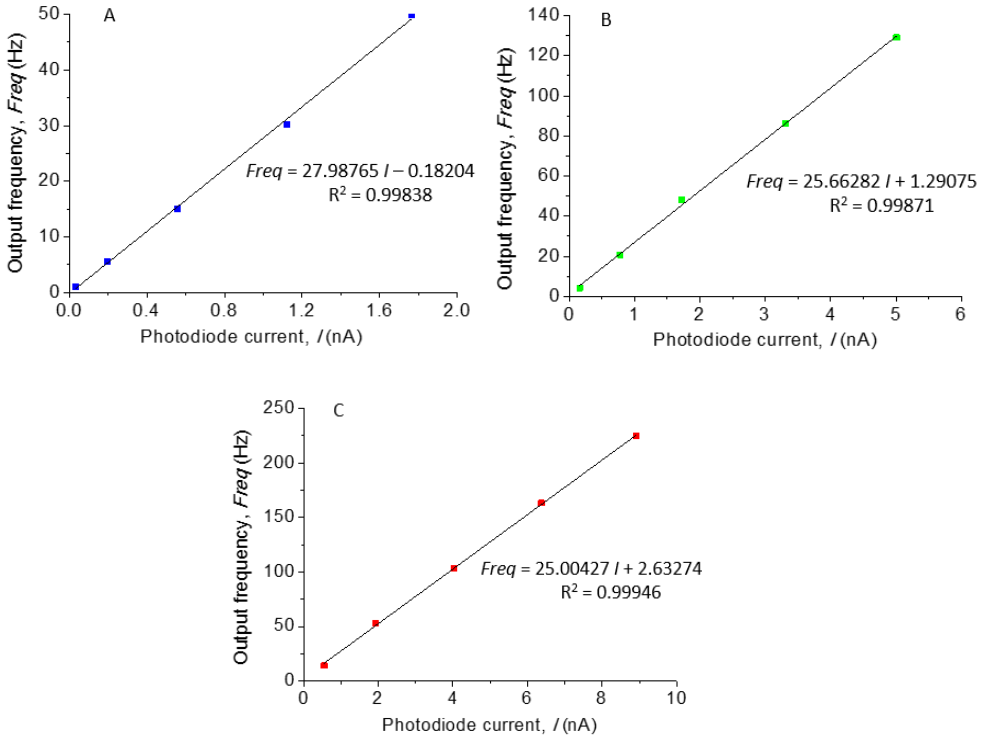

Figure 4.22 Frequency as a function of photodiode current for three fixed wavelengths: 450 nm (A), 550 nm (B) and 700 nm (C).

The results show that the output frequencies are proportional to the light intensity that reaches the photodiode, showing a good linearity, since the values of R^2 are higher than 0.99. It is also important to note that the measured values in absence of light were approximately 0.6 Hz for a current of 23.4 pA.

The total capacitance ($C_s + C_p + C_{MOS}$) and the $R_{p1} // R_{p2}$ were obtained experimentally (at 700 nm) based on two photodiode currents and the respective output frequencies, i. e., using a system of equations based on Equation 4.7. As a result, the obtained values are 29.55 pF and 2.94 GΩ, for the used photodiode. It is important to refer that the photodiode capacitance is wavelength dependent. It was chosen the wavelength of 700 nm, once it is the value at which the used equipment has its maximum efficiency, as it can be seen on Figure 4.20 and Figure 4.21. Finally, the energy stored (ΔEC) in the capacitor M2 is 28.90 pJ (using Equation 4.8).

4.2.3 Current-to-frequency (IF) features

The IF converter performance was also studied, using a current source at its input (between 60 pA and 300 μA, approximately). The setup used for the experimental tests were based on a picoammeter to measure the input current (*Keithley 487*), a voltage source with a resistance to produce the input current (*Keithley 6487*), a DC power supply (*Mastech HY3005D-3*) at 3.5 V, a microcontroller to acquire the output frequency of the IF converter (*stm32vl discovery*) for low frequencies (less than 70 KHz) or a oscilloscope (*LeCroy 9310*) to measure the output frequency of the IF converter for high frequencies (higher than 300 KHz).

Figure 4.23 shows the output frequencies of the IF converter for different input currents. Experimentally, its maximum conversion limit is close to 9 MHz, which is defined by M2 discharging time and by the input maximum current, once this input current is always active even in the discharge. This maximum current is close to 300 μA. Figure 4.24 shows a zoom of Figure 4.23, showing that the IF converter has a linear behavior for input currents up to 600 nA approximately, which is more than suitable for this application, where the photodiode currents do not exceed that range (verified during the experimental tests presented on chapter 5, where the measured currents do not exceed 50 nA). Therefore, Figure 4.25 shows a more detailed zoom of Figure 4.23 for input currents up to 63 nA approximately.

Finally, taking into account Figure 4.25 and the respective equation, and considering an input current of 10 nA, a frequency of approximately 600 Hz is obtained, which is different from

the one obtained in Figure 4.22C, which is approximately 250 Hz. This is due to the photodiode total capacitance, which is not considered in this case, since none photodiode is used and the input current was directly injected in the IF input.

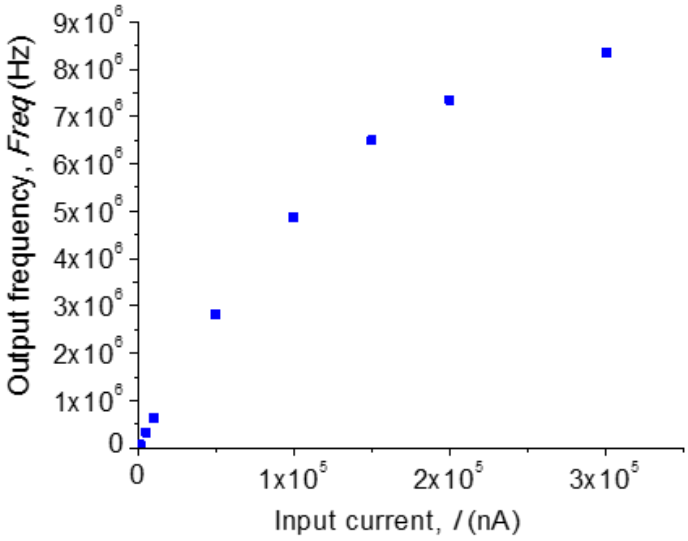

Figure 4.23 Measured frequency of the IF converter as a function of the input current.

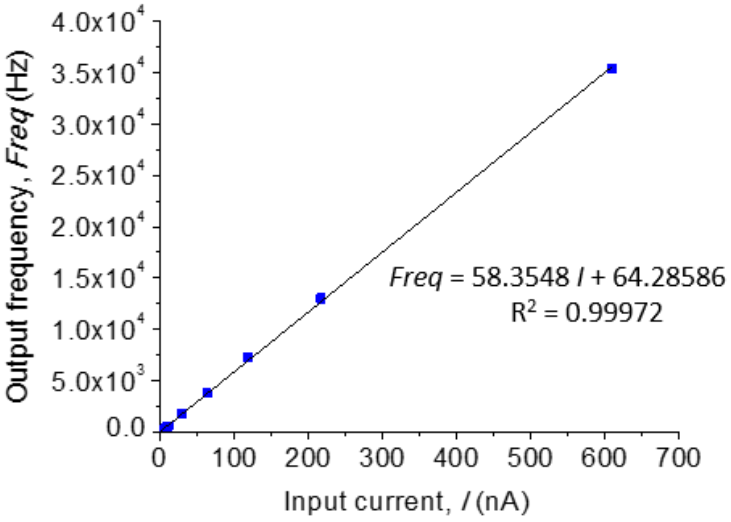

Figure 4.24 Zoom of Figure 4.23, showing the output frequency of the IF converter as a function of input currents up to 600 nA.

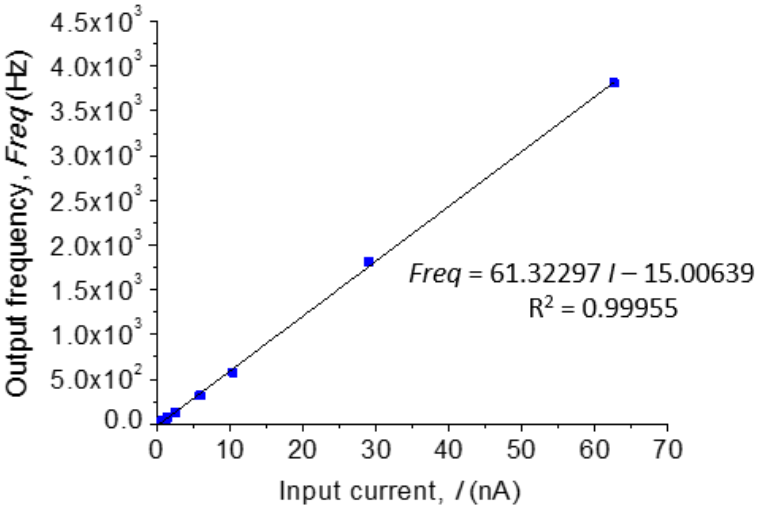

Figure 4.25 Zoom of Figure 4.23, showing the output frequency of the IF converter as a function of input currents up to 63 nA.

The IF converter power consumption was measured as 1 mW approximately, when 3.5 V is applied as supply [8]. Some important IF converter features were also studied, performing some simulations in the software *S-Edit* from *Tanner EDA* – Table 4.1 and Table 4.2. For all the simulations, different input currents were injected to study the IF behavior.

Table 4.1 shows the IF response (for an input current of 1 nA) at different doping concentrations during the mosfets fabrication (Low, Typical and Fast) at 22 °C and 3.5 V power supply. As expected, the output frequency increases with the doping concentration. The doping concentration cannot be controlled, but since the measurements are performed with the same CMOS die, this variation is not important for the application presented in this work.

Table 4.1 IF response considering different doping levels (simulation).

Input current (nA)	Output Frequency (Hz)		
	Model Low	Model Typical	Model Fast
1	57.34	61.86	67.83

The IF response at different temperatures was also simulated considering a typical doping concentration, the same input current (1 nA) and 3.5 V power supply – Table 4.2. As it can be seen, the output frequency slight increases with the temperature increase, as expected, once the

electronics is silicon based. This variation can be compensated in the final microsystem using a temperature calibration circuit.

Table 4.2 IF response considering different temperatures (simulation).

Input current (nA)	Output Frequency (Hz)			
	22 °C	37 °C	40 °C	42 °C
1	61.86	63.80	64.67	64.91

4.3 Conclusion

Along this chapter, the design and implementation of the on-chip CMOS microsystem were described, including the photodiodes matrix (4×4) and the respective readout electronics. Two of the photodiodes of the matrix were characterized in terms of the responsivity and the quantum efficiency in the desired spectral band to extract the spectroscopic signals – 350 nm and 750 nm. In spite of some fluctuations in the responsivity and quantum efficiency curves, this will not affect the extraction of the spectroscopic signals. The behavior of one of the photodiodes with temperature was also studied, allowing to conclude the importance of a temperature calibration circuit in the final microsystem. The performance of the readout electronics was also tested. The obtained results allow to conclude that the LF converter has a linear response with output frequencies proportional to the light intensity that reaches the photodiode. Moreover, the output frequencies are dependent of the photodiode capacitance, since the behavior of the IF was also studied when an external current source was directly injected in its input. With the study of the IF behavior, it was also possible to know the maximum input current at its input, approximately 300 μA, and the limits of linearity. Finally, the IF response at different conditions (doping concentration and temperature) was simulated, allowing concluding that the final microsystem must have a temperature calibration circuit.

References

[1] D. S. Ferreira, "Spectroscopy Systems for the Detection of Gastrointestinal Dysplasia", PhD, Escola de Engenharia, Universidade do Minho, Braga, Portugal, 2011.

[2] G. Minas, R. F. Wolffenbuttel and J. H. Correia, "A lab-on-a-chip for spectrophotometric analysis of biological fluids", *Lab on a Chip,* vol. 5, pp. 1303-1309, 2005.

[3] J. H. Correia and J. P. Carmo, *Introdução às Microtecnologias no Silício*, 1 ed. Lisboa, Portugal: Lidel, 2010.

[4] G. Minas, J. Ribeiro, R. Wolffenbuttel and J. Correia, "On-chip integrated CMOS optical detection microsystem for spectrophotometric analyses in biological microfluidic systems", *Proceedings of the IEEE International Symposium on Industrial Electronics (ISIE)*, 2005, pp. 1133-1138.

[5] G. Minas, "Microssistema Laboratorial Para Análise de Fluídos Biológicos", PhD, Eletrónica Industrial, Universidade do Minho, Braga, Portugal, 2004.

[6] Ö. Bazkir, "Quantum efficiency determination of unbiased silicon photodiode and photodiode based trap detectors", *Reviews on Advance Materials Science,* vol. 21, pp. 90-98, 2009.

[7] A. Moini, *Vision Chips*: Kluwer Academic Publishers, 2000.

[8] R. G. Correia, S. Pimenta and G. Minas, "CMOS Integrated Photodetectors and Light-to-Frequency Converters for Spectrophotometric Measurements", *submitted to IEEE Sensors,* 2016.

[9] S. Pimenta, S. Cardoso, E. M. S. Castanheira and G. Minas, "Advances towards a miniaturized optical system for gastrointestinal cancer detection using diffuse reflectance and fluorescence spectroscopies", in *Gastrointestinal Cancers: Prevention, Detection and Treatment*, Volume 1, Chapter 13, A. K. Tyagi and S. Prasad (Editors), Nova Publishers, New York, 1 Dec. 2016; ISBN: 978-1-53610-168-3.

[10] O. Optoeletronics. (May, 2016). *Photodiode Characteristics and Applications*. Available: http://www.osioptoelectronics.com/application-notes/AN-Photodiode-Parameters-Characteristics.pdf

[11] R. G. Correia, "Microssistema eletrónico para leitura, controlo e atuação de compostos bioquímicos num Lab-on-a-chip", PhD, Escola de Engenharia, Universidade do Minho, Braga, Portugal, 2016.

[12] R. J. Baker, *CMOS: Circuit Design, Layout, and Simulation*, 3rd ed. New Jersey: John Wiley & Sons, 2010.

[13] M. Bucher, C. Lallement, C. Enz, F. Théodoloz and F. Krummenacher, "The EPFL-EKV MOSFET model equations for simulation", *Technical Report, Electronics Laboratory, Swiss Federal Institute of Technology,* 1997.

[14] T. Bergsten, K.-E. Rydler, O. Gunnarsson, G. Eklund and V. Tarasso, "A Precision Current Source Using–Modulation", *IEEE Transactions on Instrumentation and Measurement,* vol. 60, pp. 2341-2346, 2011.

[15] H. S. Narula and J. G. Harris, "A time-based VLSI potentiostat for ion current measurements", *IEEE Sensors Journal,* vol. 6, pp. 239-247, 2006.

[16] Y. Zhu, S. R. Moheimani and M. R. Yuce, "A 2-DOF MEMS ultrasonic energy harvester", *IEEE Sensors Journal,* vol. 11, pp. 155-161, 2011.

[17] J. H. Correia, G. De Graaf, M. Bartek and R. F. Wolffenbuttel, "A CMOS optical microspectrometer with light-to-frequency converter, bus interface, and stray-light compensation", *IEEE Transactions on Instrumentation and Measurement,* vol. 50, pp. 1530-1537, 2001.

5 Experimental results

This chapter presents the on-chip experimental measurements performed on tissue phantoms, for the validation of the optical filters and the implemented CMOS microsystem. Moreover, a discussion of the several results is presented as well as the several challenges during the measurements performance. Finally, the integration of the optical filters on the top of the photodetection system (silicon photodiodes) is discussed.

5.1 Optical filters performance: diffuse reflectance and fluorescence signals measurements on tissue phantoms

The performance of the fabricated optical filters to extract the spectroscopic signals was carried out by a set of experimental measurements of diffuse reflectance and fluorescence signals. For that purpose, several phantoms, with different compositions, were used and the fabricated optical filters were placed in front of a UV-Vis-NIR spectrophotometer (*Shimadzu UV-3101PC*) or a spectrofluorometer (*SPEX® FluoroLog® 2*) detector. This procedure allows determining the accuracy of the filters to extract the signals at all the relevant spectral bands (350 nm to 750 nm), even with the obtained deviations concerning the filters performance in terms of maximum transmission peak and FWHM (previously discussed in chapter 3) [1, 2].

The phantoms used in these experiments consisted of a liquid homogeneous mixture of hemoglobin (*H0267* from *Sigma-Aldrich*), 1 μm polystyrene beads (*07310* from *Polysciences*), the fluorophores NADH (*N6005* from *Sigma-Aldrich*) and Carbostyril 124 (*363308* from *Sigma-Aldrich*), and water (see Table 5.1). In these phantoms, the main absorbing, scattering and fluorescence properties of GI tissues are represented [1, 2].

First, the spectra of the phantoms were measured without using the fabricated optical filters. After that, the same measurements using each fabricated optical filter in front of the respective detection system were performed, exactly for the same phantoms. The final signals measured with the optical filters were corrected in order to take into account the affectation of the respective filter optical transmittance in each measurement [1, 2].

Table 5.1 Phantoms used for the spectroscopic measurements with the fabricated optical filters.

Phantoms	Hemoglobin concentration (mg/mL)	Polystyrene beads concentration (%)	NADH concentration (µg/mL)	Carbostyril 124 concentration (µg/mL)
(a)	0.50	0.50	1.00	1.00
(b)	1.00	0.25	1.00	1.00
(c), (f)	1.00	0.15	1.50	0.50
(d)	0.25	0.5	0.50	1.50
(e)	0.50	0.25	1.00	1.00

Figure 5.1 shows the experimental diffuse reflectance spectra measured with the UV-Vis-NIR spectrophotometer (solid lines) and the reconstructed spectra obtained using the fabricated optical filters (dashed lines), for three phantoms presented on Table 5.1. Figure 5.2 displays the experimental fluorescence spectra measured with the spectrofluorometer (solid lines) and the reconstructed spectra obtained using the fabricated optical filters (dashed lines), also for three phantoms of Table 5.1. The reconstructed spectra were obtained by the application of a *spline Matlab* function and based only in the 16 values extracted using the fabricated optical filters in the measurements (discrete intensity values on Figure 5.1 and Figure 5.2). Moreover, it is also important to note that the fluorescence signal is only represented between 365 and 610 nm approximately, since that range covers the fluorescence emission properties of the fluorophores NADH and Carbostyril 124 [3-5]. As a result, only 12 optical filters were used, filters 2 to 13 (see Table 3.3 on chapter 3), to extract the fluorescence signal. However, as the ultimate goal is to implement a microsystem to extract simultaneously both signals – diffuse reflectance and fluorescence – the importance of the 16 optical filters must be maintained due to the diffuse reflectance not lose its good performance [1, 2].

Figure 5.1 and Figure 5.2 show that the intensity values obtained with the fabricated filters were similar to the experimental values obtained using only the commercial equipment, over the full wavelength range. To evaluate precisely the performance of the fabricated optical filters to extract the spectroscopic signals, a *Spearman's* rank correlation between the experimental and reconstructed spectra was performed in the *SPSS* software, for each phantom and for each type of spectroscopic signal – diffuse reflectance and fluorescence. *Spearman's* rank correlation is a non-parametric test (suitable for a small number of samples) that measures the degree of

association between two variables, which not considers any assumptions about the distribution of the data. For the diffuse reflectance and fluorescence signals, the results obtained for the *Spearman's* correlation coefficient (ρ_s) are presented on Table 5.2. Moreover, all the correlations were considered significant at the 0.01 level ($\alpha = 0.01$) [1, 2].

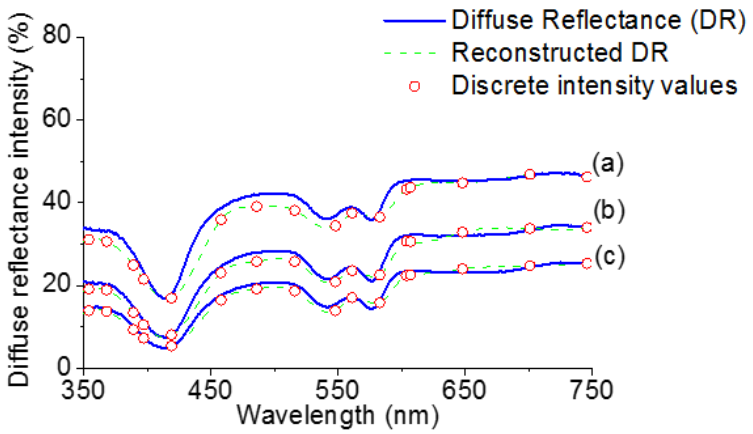

Figure 5.1 Experimental diffuse reflectance spectra of phantoms (a), (b) and (c) of Table 5.1, measured with commercial equipment (solid lines) and reconstructed spectra (dashed lines) obtained using the discrete intensity values extracted with the fabricated optical filters (discrete points), (adapted from [1] with permission from OSA).

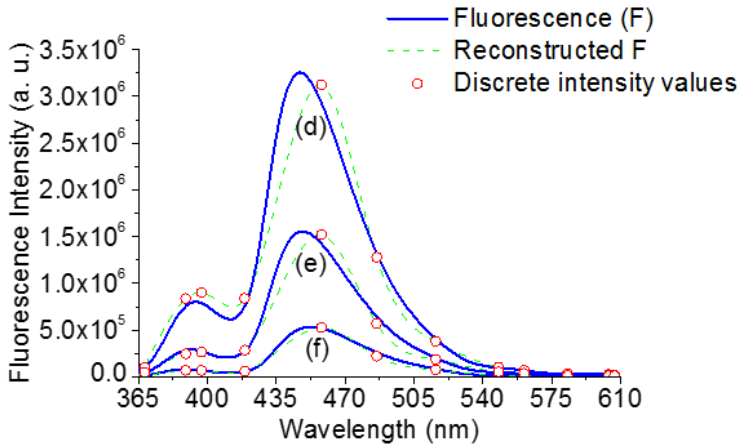

Figure 5.2 Experimental fluorescence spectra of phantoms (d), (e) and (f) of Table 5.1, measured with commercial equipment (solid lines) and reconstructed spectra (dashed lines) obtained using the discrete intensity values extracted with the fabricated optical filters (discrete points), (adapted from [1] with permission from OSA).

Table 5.2 S*pearman's* correlation coefficients (ρ_s) for each of the test phantom.

Phantoms	*Spearman's* coefficient (ρ_s)
(a)	0.985
(b)	0.971
(c)	0.981
(d)	0.987
(e)	0.990
(f)	0.988

With these results (high values for the *Spearman's* correlation coefficients), it is confirmed the feasibility of using the fabricated 16 thin-film narrow bandpass optical filters to correctly extract the diffuse reflectance and fluorescence signals [1, 2].

5.2 Microsystem performance: on-chip diffuse reflectance signal extraction on tissue phantoms

The diffuse reflectance experimental tests were carried out using the implemented microsystem (specifically one of the matrix photodiode with the active area of 100 × 100 μm^2), the fabricated optical filters and one light source (intensity curve in Appendix IV). Figure 5.3 shows the optical setup implemented for the spectrophotometric measurements. It comprises: an optical fiber (*Newport 77577*), to direct the light from the light source to the sample; a picoammeter (*Keithley 487*), to measure the on-chip photodiode current for each optical filter placed between the sample and the on-chip microsystem; and each fabricated optical filter with the respective commercial optical filter/s (as explained on Appendix I), to eliminate the second order effects. All the components in the optical light path were positioned as close as possible in order to minimize the light loss and air layers interference and to maximize the system measurements sensitivity.

Table 5.3 shows the created phantoms to perform the experimental measurements. Again, the used phantoms consist of a liquid homogeneous mixture of hemoglobin (*H0267* from

Sigma-Aldrich), 1 μm polystyrene beads (*07310* from *Polysciences*), the fluorophores NADH (*N6005* from *Sigma-Aldrich*) and Carbostyril 124 (*363308* from *Sigma-Aldrich*), and water.

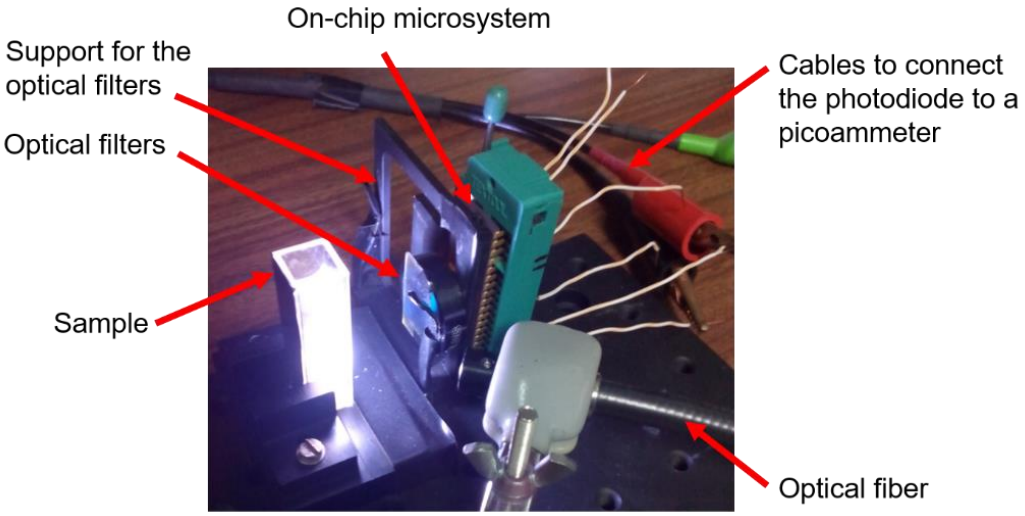

Figure 5.3 Optical setup for the on-chip diffuse reflectance measurements.

Table 5.3 Created phantoms for the experimental diffuse reflectance measurements with the on-chip microsystem and the fabricated optical filters.

Phantoms	Hemoglobin concentration (mg/mL)	Polystyrene beads concentration (%)	NADH concentration (μg/mL)	Carbostyril 124 concentration (μg/mL)
(a)	0.25	0.50	0.50	1.50
(b)	0.50	0.25	1.00	1.00
(c)	1.00	0.15	1.50	0.50
(d)	1.20	0.08	1.50	0.50

Figure 5.4 shows the extracted signals, for the phantoms presented on Table 5.3 with the on-chip photodiode and with one commercial photodiode for comparison (*S2386-5K Hamamatsu*). It is important to mention that it was used $BaSO_4$ (in a quartz cuvette) as reference for the 100% of diffuse reflectance. Moreover, the diffuse reflectance of a quartz cuvette with water was subtracted from the total diffuse reflectance of each phantom, in order to remove its effect from the diffuse reflectance signal.

As it can be observed on Figure 5.4, with the use of the optical setup presented on Figure 5.3 it is possible to extract the diffuse reflectance signals of the phantoms presented on Table 5.3 with very small differences when compared to the same signals acquisition with a commercial photodiode, proving the viability of the on-chip measurements. Moreover, the signals behavior is in accordance with the expected, with a decrease of the diffuse reflectance signal as the hemoglobin concentration increases and the polystyrene beads concentration decrease (from (a) to (d)), i. e., the main contributors to the diffuse reflectance signal behavior. It is also important to refer that phantoms with higher hemoglobin concentration and lower polystyrene beads concentration were not considered since the diffuse reflectance of the phantoms will be too low, being close to the diffuse reflectance of a quartz cuvette with water (blank).

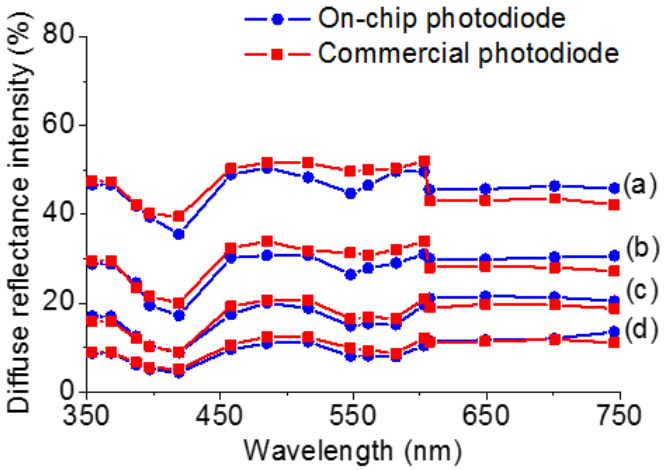

Figure 5.4 Diffuse reflectance spectra measured with one of the photodiodes of the microsystem (on-chip photodiode) and with the *S2386-5K Hamamatsu* photodiode (commercial photodiode). The phantoms (a) to (d) are represented on Table 5.3.

Concerning the spectra intensity and shape, for the different phantoms in Figure 5.4, and comparing with the results obtained in chapter 2 for a similar group of phantoms (Figure 2.14), slight differences are noted, especially below 600 nm. In Figure 5.4, the spectra intensity values are higher and the second hemoglobin peaks (in the region 520-590 nm) are not well defined/clarified. This may be due to some lack of sensitivity of the implemented optical setup to measure the diffuse reflectance signal. As a result, the effect of hemoglobin in the diffuse reflectance signal is less noted (especially where it must be detected, below 600 nm, because its molar extinction coefficient is higher [see Figure 2.2]). However, the typical affectation of

hemoglobin in the diffuse reflectance signal is noted in its main absorption peaks (in the spectral range 350-450 nm and 520-590 nm).

This lack of sensitivity of the optical setup implemented was also observed in the fluorescence signal extraction (that will be discussed in the next section – section 5.3) and may be due to the distances between the optical elements, as it can be seen on Figure 5.3. The distance between the elements can be reduced in the future with the use of LEDs, for illumination of the sample, and mainly with the use of miniaturized optical filters integrated on the top of the photodiodes. This question will be discussed on section 5.4.

5.3 Microsystem performance: on-chip fluorescence signal extraction on tissue phantoms

The on-chip fluorescence experimental tests were performed with an optical setup similar to the one presented on Figure 5.3, but with the light source fixed at 350 nm (for the fluorophores excitation) – Figure 5.5. Again, all the components in the optical light path were positioned as close as possible in order to minimize the light loss and air layers interference, maximizing the system measurements sensitivity.

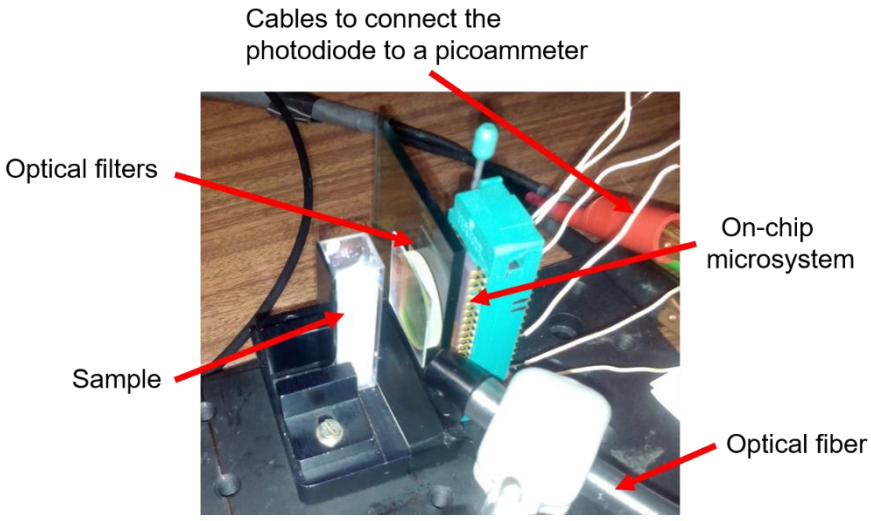

Figure 5.5 Optical setup for the on-chip fluorescence measurements.

In a first step, the same phantoms presented on Table 5.3 were considered, which are in accordance with the ones considered along the thesis. However, it was checked that the implemented optical setup has lack of sensitivity to determine the fluorescence signal emitted by

these phantoms (the obtained signals were too small, lower that 0.01 nA). Since the optical setup cannot be improved because of the optical elements used, phantoms with higher fluorophores concentration were considered.

Table 5.4 presents some of the phantoms experimentally tested. Again, the used phantoms consist of a liquid homogeneous mixture of hemoglobin (*H0267* from *Sigma-Aldrich*), 1 μm polystyrene beads (*07310* from *Polysciences*), the fluorophores NADH (*N6005* from *Sigma-Aldrich*) and Carbostyril 124 (*363308* from *Sigma-Aldrich*), and water. Figure 5.6 shows the fluorescence signals obtained for the phantoms presented on Table 5.4, using only 12 optical filters, filters 2 to 13 (see Table 3.3 on chapter 3). It is important to note that the obtained currents below 0.023 nA were considered as 0 nA, since this is the limit of the set photodiode + readout electronics (as shown in chapter 4).

Table 5.4 Created phantoms for the experimental fluorescence measurements with the on-chip microsystem and the fabricated optical filters.

Phantoms	Hemoglobin concentration (mg/mL)	Polystyrene beads concentration (%)	NADH concentration (μg/mL)	Carbostyril 124 concentration (μg/mL)
(a)	0.25	0.50	25	75
(b)	0.25	0.50	50	150
(c)	0.25	0.50	75	225
(d)	0.25	0.50	100	300

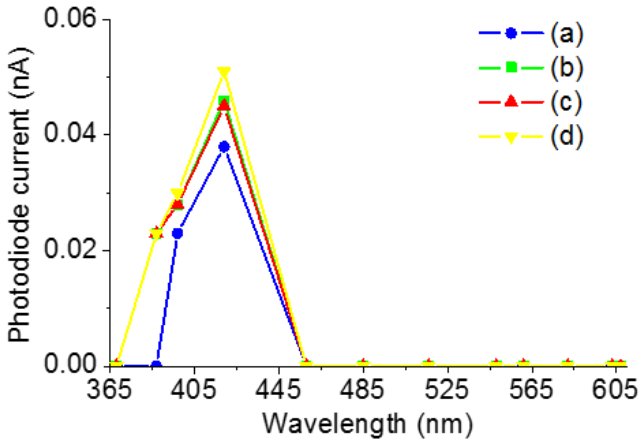

Figure 5.6 Fluorescence signals ($\lambda_{excitation}$ = 350 nm) for phantoms (a), (b), (c) and (d) of Table 5.4 obtained with the optical setup of Figure 5.5.

For the reflectance measurements, it was used $BaSO_4$ as a reference for the 100% of diffuse reflectance, which is very useful because that way the diffuse reflectance measurements are relative and they are not affected by the optical filters transmittance and by the on-chip photodiodes efficiency, in each measurement. For the fluorescence measurements, there is not a reference. That way, it must be ensured that the obtained signals are not affected by the optical filters transmittance and photodiodes efficiency. As a result, instead of comparing the obtained results with the ones measured with a commercial photodiode, the same phantoms were measured in a commercial spectrofluorometer (*SPEX® FluoroLog® 2*) with a set of conditions that aims to reproduce the optical setup of Figure 5.5. Thus, it was used a front face geometry (selected on the spectrofluorometer), where it is detected the fluorescence emitted from the same surface of excitation light incidence, and triangular cuvettes (shown on Figure 5.7), since on the optical setup of Figure 5.5 the angle between illumination and detection is approximately 45°. The equipment excitation and emission slits were opened and the tension of the photomultiplier was lowered, in order to avoid saturation.

Figure 5.7 Triangular quartz cuvette used for the fluorescence measurements on the spectrofluorometer (*SPEX® FluoroLog® 2*).

Figure 5.8 shows the fluorescence spectra obtained in the commercial spectrofluorometer for the phantoms of Table 5.4.

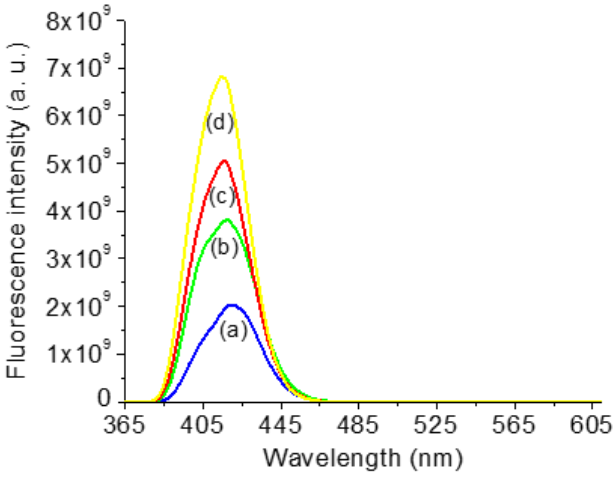

Figure 5.8 Fluorescence signals ($\lambda_{excitation}$ = 350 nm) for phantoms (a), (b), (c) and (d) of Table 5.4 obtained with the commercial spectrofluorometer.

Comparing the obtained results (Figure 5.6 and Figure 5.8), it can be observed that the shape of the spectroscopic signals is similar, with the fluorescence peak close to 419 nm. However, a lack of sensitivity can be noted on the optical setup of Figure 5.5, since the fluorescence signals of phantoms (b) and (c) were not distinguished, as expected and noted on Figure 5.8. Yet, it can be concluded that the shape of the fluorescence signals extracted with the optical setup of Figure 5.5 are in accordance with the expected with a fluorescence peak in the right wavelength (close to 419 nm) and with the highest intensity in the phantom with the highest fluorophores concentration, phantom (d).

Again, the lack of sensitivity may be due to the distances between the optical elements, as it can be seen on Figure 5.5. In the future, it is crucial to reduce the distance between the elements, as reported at the end of the previous section.

5.4 Integration of the optical filters on the top of the silicon photodiodes

5.4.1 CMOS die patterning and optical filters deposition

All the steps described in this section were processed at INESC-MN, Lisbon. The most important step of this approach, for trying to integrate optical filters on top of the silicon photodiodes

(direct deposition of an optical filter in a photodiode), was the pattern of a CMOS die (processed previously using *AMIS Technology* from *Europractice*, as explained in chapter 4) with a specific mask. A photolithography process was used to pattern the desired mask into a photosensitive material, a PR (photoresist). The mask was previously drawn in *AutoCAD* software [6].

Considering a cavity/hole etched (with deep reactive ion etching, at INL - Braga) on a silicon piece of 25.4 × 25.4 mm^2 (Figure 5.9), the CMOS die (area of 5 mm^2, Figure 5.10) was manually glued on that hole using *Ablebond 2025D* and cured for one hour in an oven at 150 °C. That way, it is possible the sample (CMOS die glued on a silicon holder – Figure 5.11) handling and loading into the processing machines [6].

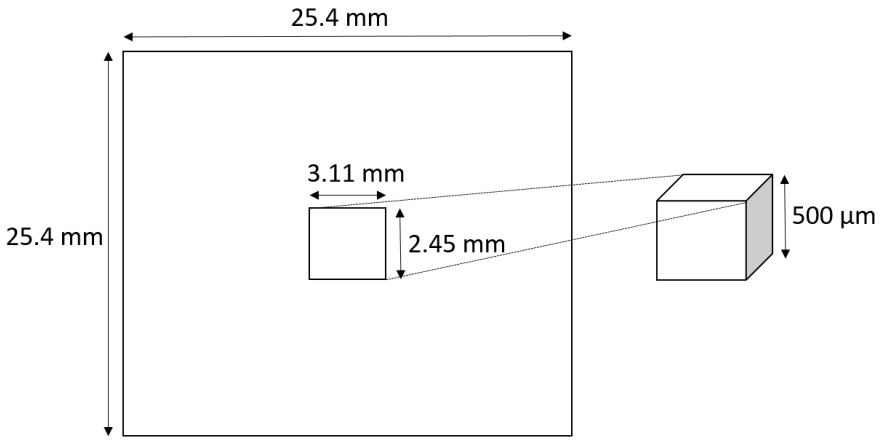

Figure 5.9 Silicon holder with the cavity/hole for the CMOS die (not scaled).

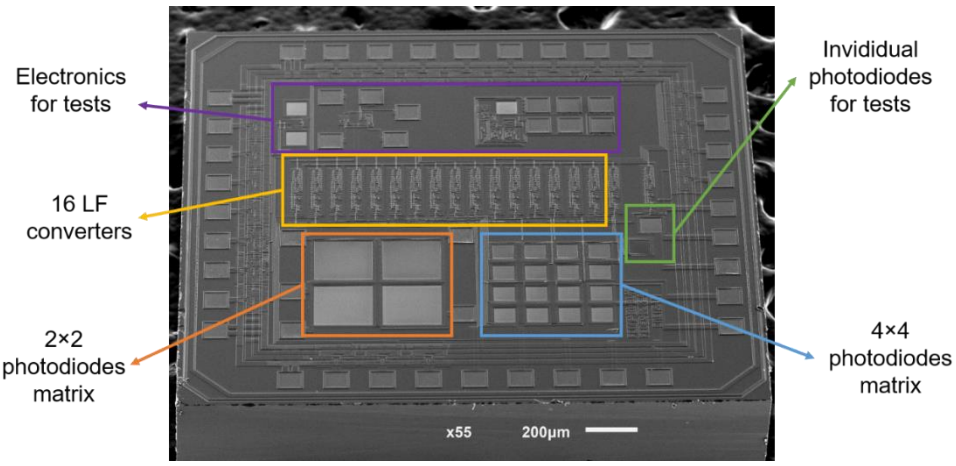

Figure 5.10 SEM image (45° tilt) of the implemented CMOS die (acquired with a *JEOL JSM-6010LV* SEM instrument [at 3B's Research Group, University of Minho]). Each photodiode of the 4×4 matrix has an active area of 100 × 100 μm^2 and each photodiode of the 2×2 matrix has an active area of 250 × 250 μm^2 (an extra matrix added on the on chip microsystem that could be useful for spectroscopic tests).

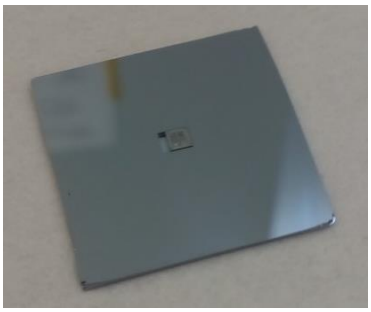

Figure 5.11 Photograph of the CMOS die glued on the silicon holder (the dimensions of the silicon holder are specified of Figure 5.9).

Before starting the photolithography process, the sample was cleaned with acetone in an ultra sound bath during 30 minutes, followed by another cleaning with acetone, IPA (isopropyl alcohol), deionized water and blown dry with compressed air gun. Moreover, as a preparation for the photolithography, the sample was treated with HMDS (hexamethyldisilazane) in a vapor prime system, during 30 minutes, in order to increase the adhesion of the photoresist to the sample. The vapor prime system (*YES [yield engineering]*) applies a gaseous concentration of HDMS, at 130 °C, to the surface of the sample [6].

As a first step of the photolithography process, the sample was coated with 1.5 µm thick PR (*PFR7790G27cP*, *JSR Electronics*) using a coating and development system. Figure 5.12 shows the coating (track 1) and development (track 2) system, where it is used a spinning during 30 seconds, for the coating process, following by a 85 °C soft bake during one minute to evaporate solvents and to get an uniform layer of PR [6].

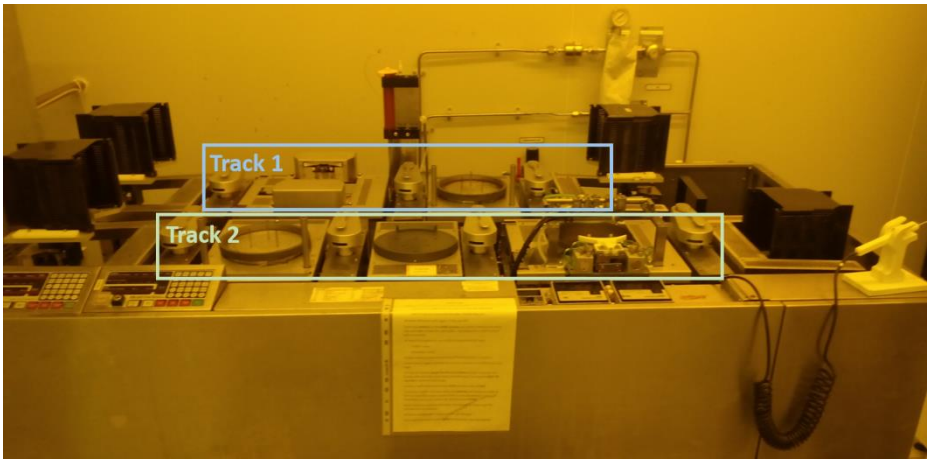

Figure 5.12 Coating (track 1) and development (track 2) system (*SVG [silicon valley group]*).

After the PR coating, two rectangular regions were defined in the sample, using a DWL (direct write laser) system, setting where the optical filter will be deposited. In this case, it were considered two rectangular regions that correspond to two photodiodes, one with an area of 100 × 100 μm^2 (in the photodiodes matrix [4×4]) and another with an area of 250 × 250 μm^2 (in the extra matrix [2×2]). The DWL system (*Heidelberg DWL 2.0*) uses a diode laser (440 nm) to write the desired mask in the sample PR. The process has a maximum resolution of 0.8 µm and an alignment precision of 0.1 µm. In this case, it was used positive PR, so that, the exposed areas to the laser become soluble and will be removed during the development step. Contrarily, the not exposed areas will be kept. That way, the mask patterning is defined. The used mask was non-inverted, since it was desired to expose inside the two rectangular regions [6].

The final step of the photolithography process on the sample, before the direct optical filters deposition on photodiodes, was the development step. This was performed in the system presented on Figure 5.12, track 2. In this track, the sample is baked at 110 °C for one minute followed by a cool down of one minute. After that, the sample is poured with a developer (*TMA 238 WA*), that will dissolve and remove the PR exposed areas. Finally, the sample is cleaned with deionized water [6].

After the CMOS die patterning using the photolithographic process, the next step was the deposition of an optical filter on the sample. The deposition of the optical filters was based on the same process described on section 3.3 (chapter 3), the IBD process. The only difference is that the TiO_2 films were prepared from a ceramic target. Again, the Xe beam distortion caused by charging at the target surface was avoided with a neutralizer (e-beam), ensuring a stable deposition rate along several hours of deposition. Since a new target was used, the experimental refractive indices as a function of wavelength, of a thin-film of TiO_2, were measured (at INL-Braga), for a new optical filter programming. At that moment, it was deposited an optical filter programmed for the wavelength of 540 nm (using the materials combination SiO_2/TiO_2), for trying to prove the concept of the direct deposition of an optical filter on a photodiode.

5.4.2 Integrated optical filters characterization

After the optical filter deposition on the sample it is necessary to remove the PR layer, which results in a sample with the optical filter deposited only on the top of the required photodiodes (where the PR is not presented). The PR layer was removed in an ultra sound bath

with *Microstrip 3001*, followed by a cleaning with IPA, deionized water and blown dry with compressed air gun.

Figure 5.13 shows a microscope image of a CMOS die with the 540 nm optical filter deposited on the top of two photodiodes. As it can be observed, the optical filter seems to be right deposited on the desired photodiodes.

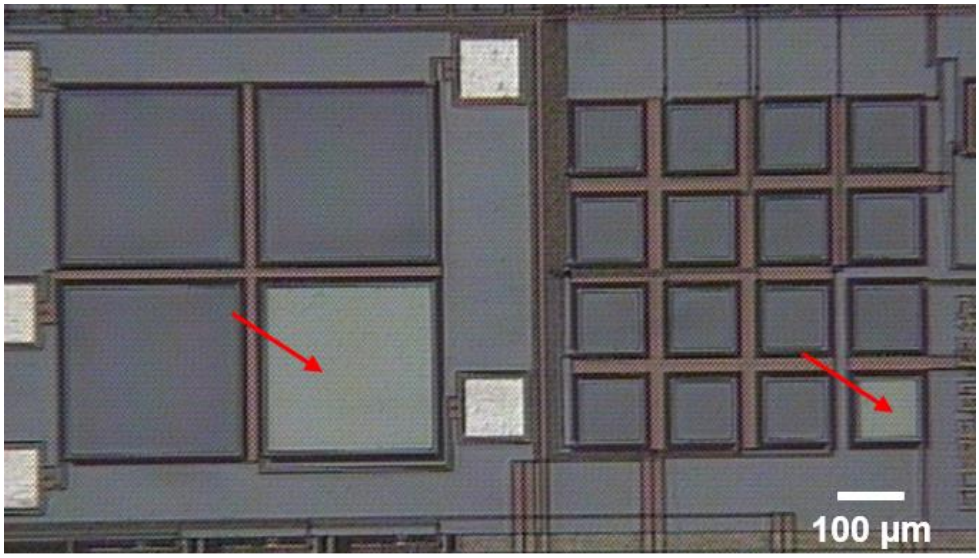

Figure 5.13 Microscope (*Olympus BH2-UMA*) image (10×) of a CMOS die with the 540 nm optical filter deposited on two photodiodes (indicated with arrows).

During the optical filter deposition on the sample (containing the CMOS die) the optical filter was also deposited on a borosilicate glass for optical transmittance characterization. Figure 5.14 shows the optical transmittance of the optical filter programmed for 540 nm. As it can be seen, the obtained result is unexpected since the transmittance peak is too small (approximately 2% at 530 nm). This result could be due to the change in the refractive indices of one of the materials being used (SiO_2), since a long period of time has passed between this new approach and the materials characterization performed on chapter 3.

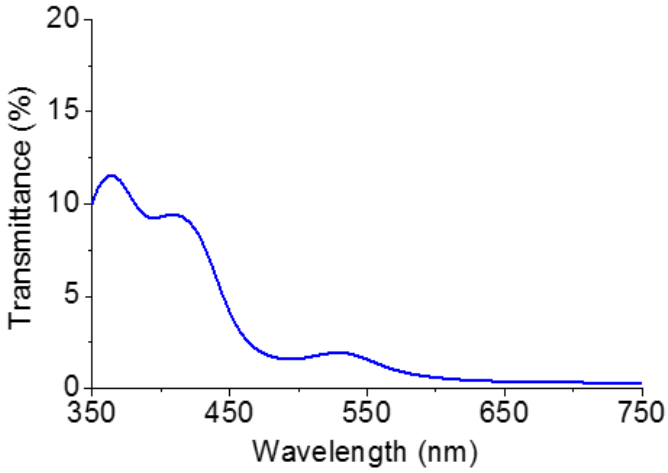

Figure 5.14 Optical transmittance for the optical filter programmed for the 540 nm.

Moreover, the CMOS die was extracted from the silicon holder, for further package and wirebonding. As a result, the dicing of the sample was performed in an automatic dicing saw (*DAD 321*). After the package and wirebonding the characterization of the set of photodiodes and optical filter was performed, measuring the photodiodes curve. It was verified that the presence of the optical filter on top of the photodiodes does not have a significant effect on the photodiodes curves, which is unexpected since the optical filter transmittance (Figure 5.14) is too low.

As a result, it was necessary to perform SEM measurements at CMOS die regions containing the photodiodes with the optical filter deposited, in order to investigate if the optical filter was adequately deposited on the photodiodes. Figure 5.15 exhibits the SEM images showing the cross section of the filters in the 250 × 250 μm^2 photodiode (A) and in the 100 × 100 μm^2 photodiode (B).

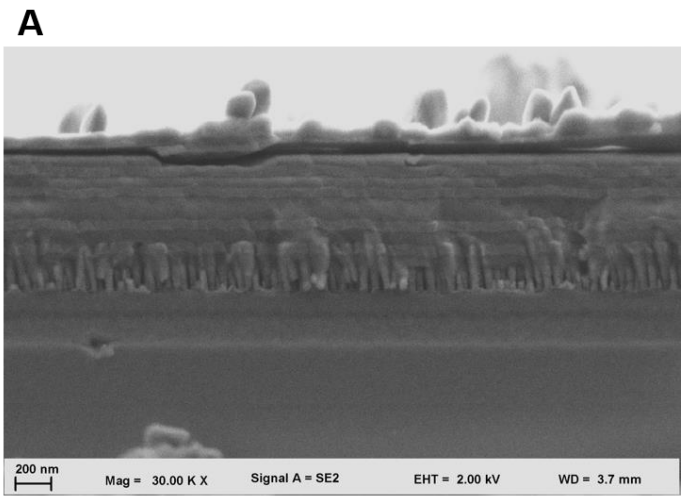

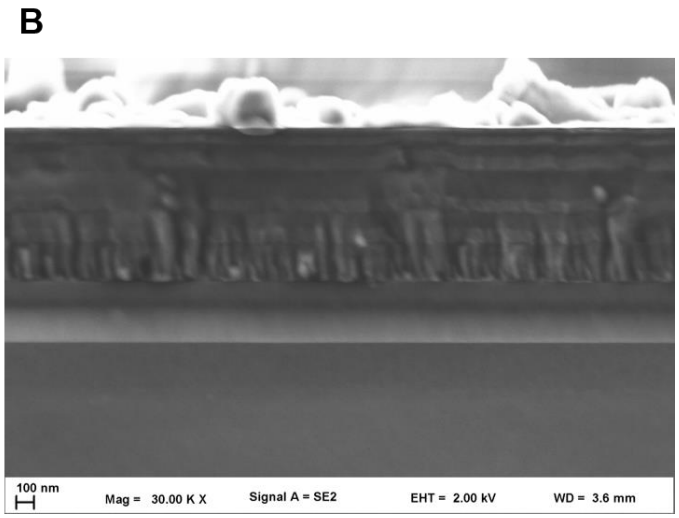

Figure 5.15 SEM images (obtained using a *AURIGA Compact FIB-SEM* instrument at 3B's Research Group, University of Minho), showing the cross-section of the optical filter deposited on the 250 × 250 μm² photodiode (A) and in the 100 × 100 μm² photodiode (B).

As it can be observed on Figure 5.15 the optical filter is deposited on the photodiodes surface, which was also confirmed by profilometry, where a total optical filter thickness of approximately 900 nm was obtained (the optical filter total thickness was programed to be 889 nm). However, it can also be detected that the first layers of the optical filter (close to the photodiodes surface) are not as uniform as the others, being irregular along the cross-section. These irregularities may affect the optical filter performance on the top of the photodiodes, and are unexpected, since the photodiodes surface is the second oxide of SiO_2 (information given by the *AMIS Technology* from *Europractice*) and a correct adherence of the filter must happen. So, in future, it is necessary to evaluate the surface of the photodiodes and verify if there are some materials compositions on that surface that may affect the uniformity of the thin-film deposition on its top. The EDS (energy-dispersive x-ray spectroscopy) technique can be used to evaluate the materials compositions on the photodiodes surface. Moreover, the several steps (described on section 5.4.1) performed on the CMOS die before the optical filter deposition must be revised, to ensure that they do not affect the uniformity of the first layers deposited on the photodiodes surface.

5.4.3 Full integration of the optical filters on the photodetection system

The full integration of the 16 optical filters on the top of the silicon photodiodes (one optical filter for each photodiode) will be possible, considering several levels of patterning/masks of PR,

one mask for each optical filter, and after solving all the issues related with this approach (previously described).

Moreover, the optical filters to remove the second order effects of the main optical filters can also be integrated on the chip, through their direct deposition on the top of the main optical filters. As an example, a wide band pass filter between 350 and 500 nm, approximately, can be implemented considering 9 alternate layers of SiO_2 and TiO_2, each one with 71 nm, and a tenth layer of Ag (silver) with 15 nm. Figure 5.16 shows the filter optical transmittance simulated on *TFCalc 3.5* software and considering the experimental refractive indices of the SiO_2 and TiO_2 materials, previously measured and presented at chapter 3.

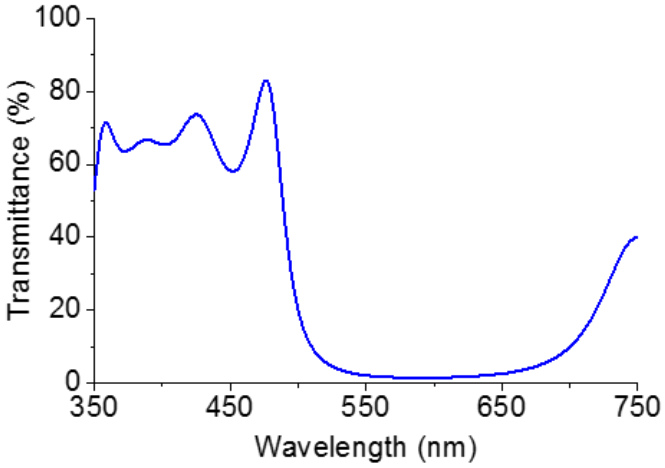

Figure 5.16 Band pass filter between 350 and 500 nm, to eliminate the second order effects of the UV/Vis region optical filters.

5.5 Conclusion

In this chapter, experimental tests were performed for the validation of the implemented optical filters and the CMOS microsystem. In a first step, the viability of the fabricated optical filters to correctly extract spectroscopic signals was proven through tests with a commercial spectrophotometer and spectrofluorometer and considering a group of phantoms. After that, on-chip measurements carried out with tissue phantoms were performed, using not only the fabricated optical filters but also the CMOS microsystem. The obtained results allow to conclude the viability of extracting diffuse reflectance and fluorescence signals with low differences when compared to those obtained with commercial equipment. Some issues were noted, specifically, a lack of sensitivity on the optical setups implemented for the on-chip measurements, which may be avoided

in future with a distance reducing between the optical elements on the setups. Finally, the integration of the optical filters on the photodetection system, i. e., the direct deposition, by IBD, of each optical filter on top of the respective photodiode, was discussed and a new approach was tested.

References

[1] S. Pimenta, S. Cardoso, A. Miranda, P. De Beule, E. Castanheira and G. Minas, "Design and fabrication of SiO_2/TiO_2 and MgO/TiO_2 based high selective optical filters for diffuse reflectance and fluorescence signals extraction", *Biomedical Optics Express,* vol. 6, pp. 3084-3098, 2015.

[2] S. Pimenta, S. Cardoso, E. M. S. Castanheira and G. Minas, "Advances towards a miniaturized optical system for gastrointestinal cancer detection using diffuse reflectance and fluorescence spectroscopies", in *Gastrointestinal Cancers: Prevention, Detection and Treatment*, Volume 1, Chapter 13, A. K. Tyagi and S. Prasad (Editors), Nova Publishers, New York, 1 Dec. 2016; ISBN: 978-1-53610-168-3.

[3] J. R. Lakowicz, *Principles Fluorescence Spectroscopy*, Third Edition ed. New York, USA: Springer, 2006.

[4] X. Dai, E. Rollin, A. Bellerive, C. Hargrove, D. Sinclair, C. Mifflin*, et al.*, "Wavelength Shifters for Water Cherenkov Detectors", *Nuclear Instruments and Methods in Physics Research A* vol. 589, pp. 290–295, 2008.

[5] Sigma-Aldrich. (2012, February, 2016). *Product Information - Beta-Nicotinamide adenine dinucleotide, reduced disodium salt hydrate*. Available: http://www.sigmaaldrich.com/content/dam/sigma-aldrich/docs/Sigma/Product_Information_Sheet/2/n6005pis.pdf

[6] J. Santos, "Methodologies for monolithic integration and 3D through silicon vias microfabrication for chip integration with CMOS", Master, Bioengineering and Nanosystems, Técnico Lisboa, Lisboa, 2016.

6 Conclusions and future work

In this chapter, the main conclusions and final considerations of the performed work are described. Moreover, some important future work is also proposed.

6.1 Conclusions

The main goal of this thesis was to perform important advances towards the implementation of an on-chip microsystem to extract two different spectroscopic signals, specifically diffuse reflectance and fluorescence, for being applicable as a portable system in a surgery room, for inspecting total removing of the GI cancerous tissue during surgery; or integrated with the conventional endoscopic and colonoscopic equipment and be used as an auxiliary in early GI cancer detection.

The proposed microsystem was based on an optical filtering system, low-cost silicon photodiodes and their readout electronics, for the spectroscopic signals selection and detection in specific spectral bands.

First, the study of the spectroscopic signals was performed using phantoms with different biochemical compositions (containing hemoglobin, polystyrene microspheres to represent collagen fibers, and the fluorophores NADH and Carbostyril 124, the latter representing collagen). The typical intensity and shape of the spectral signals were studied, as well as their temperature dependence. It was verified that the diffuse reflectance signal is affected by absorption and scattering components on the phantoms. Moreover, the phantom temperature does not have any effect on the shape and intensity of diffuse reflectance signal. Concerning the fluorescence, it was observed that the fluorescence signal is affected by the fluorophores existing on the phantoms and also by absorption and scattering events. The temperature of the sample influences the fluorescence signal, but the affectation is not statistically significant. The analysis of the spectroscopic signals can be performed with different models/methods to extract quantitative information that could improve the detection of GI cancer. The reconstruction of the signals based in their extraction in a few spectral bands is also practicable, considering 16 wavelengths between 350 and 750 nm, validating the implementation of an optical filter system in the final microsystem.

The design, optimization and fabrication of 16 MgO/TiO_2 and SiO_2/TiO_2 thin-film optical filters (centered at the 16 spectral bands required for signals reconstruction) were performed. After that, the optical filters were characterized through optical transmittance, selectivity, SEM and profilometry. The optical filters results showed transmittances ranging from 50% to 90% approximately, and FWHM averaging from 11 nm to 20 nm. However, the fabricated optical filters exhibited some deviations from their simulated characteristics, which can be explained by the complexity of the optical filters design, for example, the materials refractive index dependence with wavelength and thickness of the thin-film. A more detailed characterization of the refractive indices will be time consuming and cannot be performed for all the desired thin-film thicknesses.

The design and implementation of an on-chip CMOS microsystem were performed, including a photodiodes matrix (4×4) and their respective readout electronics, based on LF converters. This CMOS microsystem was fabricated using the standard n-well 0.7 µm CMOS process from *AMIS Technology* available at *Europractice*. Two of the photodiodes were characterized, measuring their responsivity and quantum efficiency between 350 and 750 nm. The photodiodes responsivity was 200 mA/W at 550 nm, approximately. Some fluctuations on the obtained responsivity and quantum efficiency curves were noted, which do not affect the extraction of the spectroscopic signals. The current of one of the photodiodes was also study at different temperatures, which led to conclude the importance of a temperature calibration circuit in the final microsystem. The measurements using a photodiode and its respective LF converter allows concluding that the latter has a linear response (R^2>0.99), with a sensitivity of 25 Hz/nA at 550 nm, approximately, and with output frequencies proportional to the photodiode current (or to the light intensity that reaches it). Moreover, the output frequencies depend on the photodiode capacitance, which is wavelength dependent. The IF behavior was also studied when injected directly a current at its input, allowing to determine the maximum input current, which is 300 µA, its power consumption of 1 mW and the limits of linearity, confirming its linearity in the range of currents produced in this application. The IF behavior at different conditions, such as doping concentration and temperature, was simulated. The obtained results allow to conclude once more the importance of a temperature calibration circuit in the final microsystem.

Finally, experimental measurements with phantoms (also containing hemoglobin, polystyrene microspheres, NADH and Carbostyril 124) were performed for validation of the implemented optical filters and the CMOS microsystem. First, the use of the fabricated optical

filters to correctly extract spectroscopic signals was proven through tests with a commercial spectrophotometer and spectrofluorometer. Second, on-chip experimental measurements were carried out, using the fabricated optical filters and the CMOS microsystem. The results allowed concluding the viability of the optical filter system and the CMOS microsystem for extracting diffuse reflectance and fluorescence signals, with small differences when compared to those obtained with commercial equipment. However, a lack of sensitivity on the optical setups implemented for the on-chip measurements was noted. This may be avoided, in future, with a reduction of the distance between the optical elements on the setups, using LEDs and integrated optical filters on the CMOS microsystem. The direct integration of the optical filters on top of the photodiodes was discussed and a new approach was tested based on the CMOS die patterning with PR.

6.2 Future Work

Taking into account the results obtained in chapter 5, with the tests performed using the optical filters and the CMOS microsystem, the next step must be the implementation of the final microsystem with miniaturized LEDs included. That way, the system sensitivity will be higher, since the optical elements are closer. A study of the microsystem geometry must be performed to decide the better location of LEDs, in order to improve the system efficiency in the collection of spectroscopic signals. Moreover, since one of the microsystem applications could be its use to detect early stages of GI cancer, it is important to ensure that the LEDs intensity does not exceed the maximum permissible for human cells, especially in the case of fluorescence where UV LEDs can be used.

In addition, the future microsystem must have all the optical filters integrated on the silicon photodiodes. That way, further work is ongoing to solve the issues related with the direct deposition of optical filters on the top of the photodiodes (discussed on chapter 5) and to repeat the process described on chapter 3, with a detailed characterization of the materials refractive indices dependence with wavelength and thickness. Only after those tasks, it will be possible to obtain good results in the fabrication of the optical filters, since several variables (associated with the IBD process) can contribute to the changes in the refractive indices.

Another important aspect to be focused in future work is the exploration of analysis methods to obtain quantitative information from the extracted signals, in order to improve the GI cancer detection. A lot of work was already developed by several research groups, including

previous work performed by the research team (in collaboration with MIT). However, the implementation of fast and effective methods for signals analysis is essential, in collaboration with doctors and using real human GI tissue samples. Only with real tissue samples it is possible to evaluate the final microsystem performance in distinguishing signals extracted from normal, dysplastic and cancerous tissues. Moreover, only with the study of signals from real GI tissue samples is possible to interpret the real absorption, scattering and fluorescence properties of tissues that affect the signals in different parts of the GI tract. A particular aspect to be addressed is to confirm if there are additional endogenous fluorophores (besides collagen and NADH) that could play an important role in the transformations occurring in dysplastic process.

Finally, as an example, it is presented an improved final microsystem, where in addition to the LF converters other electronic components were considered towards a stand-alone microsystem for further connection to a microcontroller. Figure 6.1 shows its schematic. Eight bits synchronous counters can be used to measure the output frequency of the LF converters. One counter for each LF converter is necessary in order to ensure that all the measurements (in each wavelength selected by an optical filter) are performed in similar illumination conditions. After that, an eight bits shift register can be used to read each counter output. The use of a demultiplexer (1:16) and sixteen three-state invertors allows to control which counter output is read in each moment. Figure 6.2 illustrates the layout of the complete microsystem with all the components represented on Figure 6.1. The total area of the layout is approximately 10 mm^2.

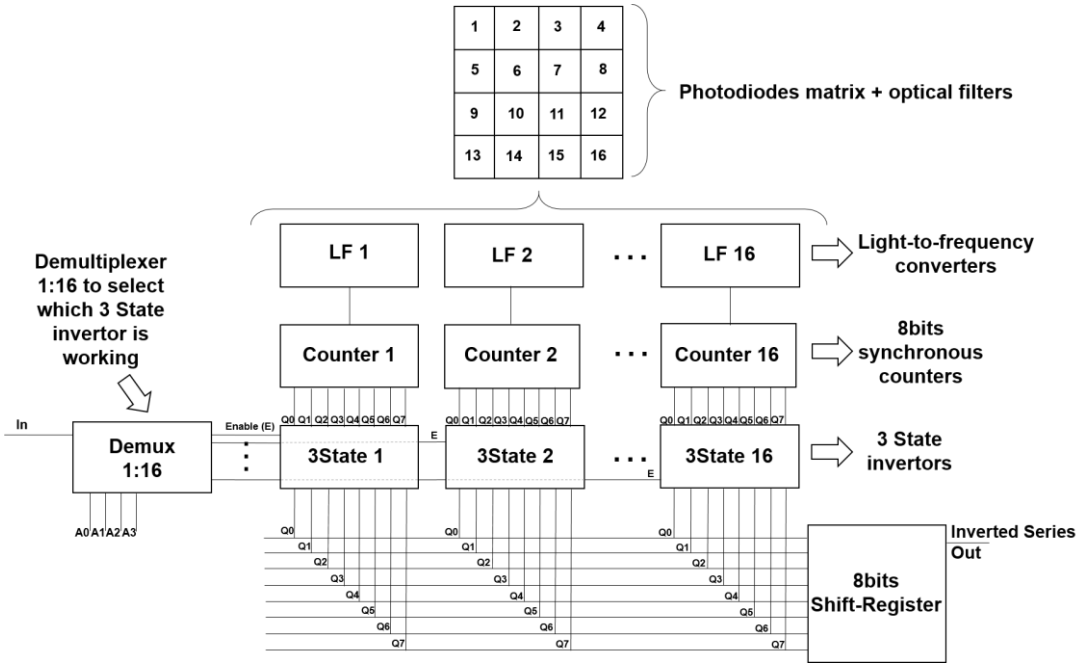

Figure 6.1 Schematic of the final microsystem (some input variables can be controlled using a microcontroller).

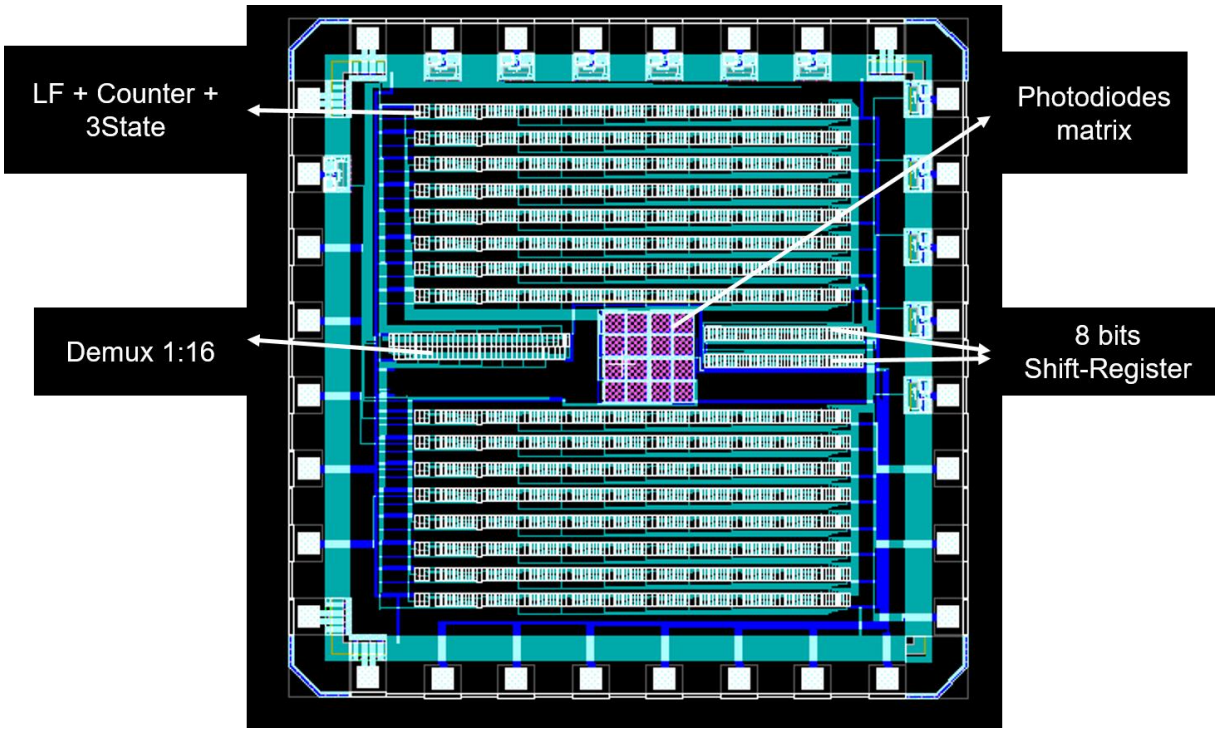

Figure 6.2 Layout of the final microsystem, extracted from the *L-Edit*, with all the components represented on Figure 6.1.

Appendices

Appendix I – Commercial optical filters used

The use of the fabricated optical filters requires some commercial wide band-pass optical filters on their top to avoid the second order effects of the fabricated filters.

For the fabricated optical filters in the UV/Vis region it is necessary to use two commercial optical filters (Commercial 1 [from *Edmund Optics*] and Commercial 2 [FSQ-KG5 from *Newport*]), as shown in Figure I.1.

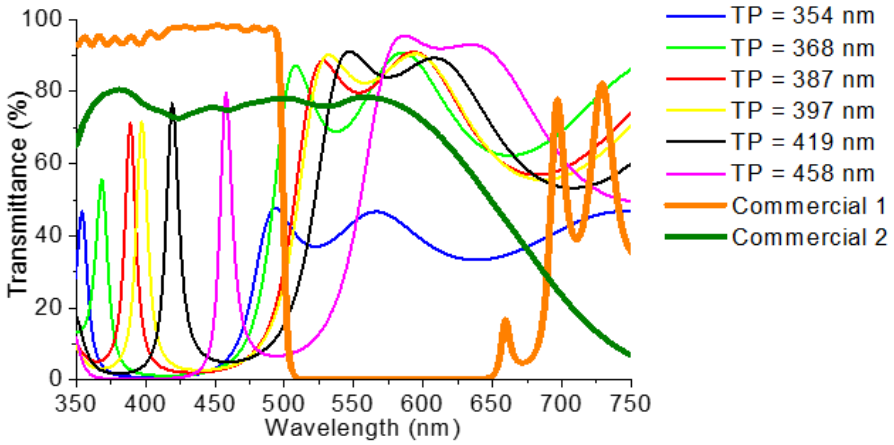

Figure I.1 Transmittance spectra of the fabricated optical filters in the UV/Vis region and commercial optical filters used to eliminate the second order effects. The transmittance curves were obtained using a UV-Vis-NIR spectrophotometer (*Shimadzu UV-3101PC*), (TP: filter maximum transmittance peak wavelength).

For the fabricated optical filters in the Vis region, it is also necessary to use two commercial optical filters (Commercial 2 [FSQ-KG5 from *Newport*] and Commercial 3 [from *Edmund Optics*]), as shown in Figure I.2.

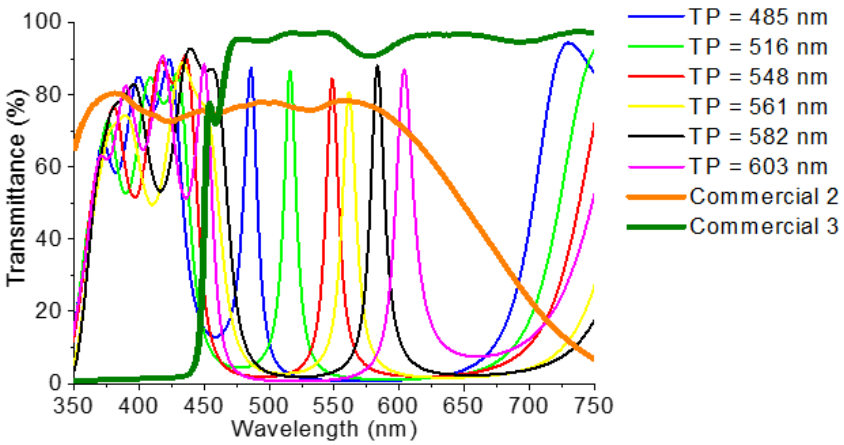

Figure I.2 Transmittance spectra of the fabricated optical filters in the Vis region and commercial optical filters used to eliminate the second order effects. The transmittance curves were obtained using a UV-Vis-NIR spectrophotometer (*Shimadzu UV-3101PC*), (TP: filter maximum transmittance peak wavelength).

Finally, for the optical filters in the Vis/IR region, it is necessary to consider a commercial optical filter (Commercial 4 [FEL0600 from *Thorlabs*]), as shown in Figure I.3.

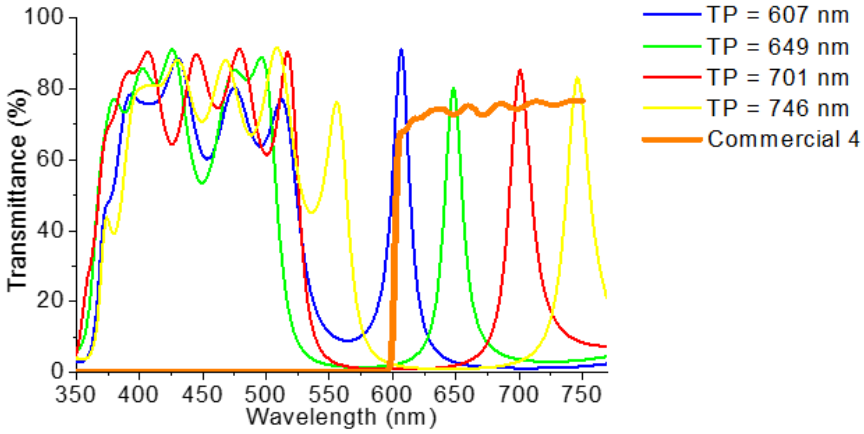

Figure I.3 Transmittance spectra of the fabricated optical filters in the Vis/IR region and commercial optical filter used to eliminate the second order effects. The transmittance curves were obtained using a UV-Vis-NIR spectrophotometer (*Shimadzu UV-3101PC*), (TP: filter maximum transmittance peak wavelength).

Appendix II – Commercial optical filters available

For a comparison between the fabricated filters and the available commercial ones, the Tables below present the main features of the commercial bandpass optical filters, according to several established suppliers. The information is presented as it is available in the websites.

As it can be observed, in terms of fabrication flexibility, no commercial products can be integrated in microchips, due to the large size (area and thickness). The bandpass filters commercially available are already fabricated and could not be changed.

In terms of features, observing Table II.1, Table II. 2 and Table II. 3, the commercial optical filters available have FWHM and transmittances suitable for the application under this thesis (near 10 nm and about 85%, respectively), especially the ones from *Edmund Optics* (Table II.1). However, for the UV/Vis spectral bands, they do not have bandpass filters centered at 350 nm, 370 nm and 380 nm. Probably, the ones they have (the first three of Table II.1) would fit to reconstruct the signals, but it cannot be guaranteed without testing. The other suppliers do not have commercially available bandpass optical filters with these requirements of low FWHM and high transmittance.

Regarding the cost, the optical filter costs are much smaller for the thin-films, particularly upon optimization was done and a large number of wafers can be produced in a batch with the optimized film thicknesses, for each filter. Notice that, in this work, it were used the same materials and thicknesses for several optical filters (the filters were divided in four groups and, in each group, the filters mirrors have the same layers material and thicknesses), the machine deposition time and materials (due to performing the mirrors at the same time in each group) is significantly reduced, when compared to the fabrication of one at a time.

Moreover, some suppliers allow ordering a specific optical filter giving them the transmittance value and required FWHM, but, of course, this will be much more expensive, once suppliers also need to optimize the process. This was asked to Thorlabs and they answered with a price of about $10000 to fabricate an optical filter with transmission peak at 400 nm with a transmittance close to 85% and FWHM close to 10 nm.

Table II.1 Commercial bandpass optical filters from *Edmund Optics*.

Edmund Optics reference	Transmittance peak (nm)	FWHM (nm)	Transmittance	Cost	Size / Thickness (mm)
340nm CWL, 12.5mm Dia., Hard Coated OD 4 10nm Bandpass Filter	340 ± 2	10 ± 2	± 85%	118.75€	12.5 diameter/ 5
365nm CWL, 12.5mm Dia., Hard Coated OD 4 10nm Bandpass Filter	365 ± 2	10 ± 2	± 85%	118.75€	12.5 diameter/ 5
375nm CWL, 12.5mm Dia., Hard Coated OD 4 10nm Bandpass Filter	375 ± 2	10 ± 2	± 85%	118.75€	12.5 diameter/ 5
394nm CWL, 12.5mm Dia., Hard Coated OD 4 10nm Bandpass Filter	394 ± 2	10 ± 2	± 85%	118.75€	12.5 diameter/ 5
400nm CWL, 12.5mm Dia., Hard Coated OD 4 10nm Bandpass Filter	400 ± 2	10 ± 2	± 85%	104.5€	12.5 diameter/ 5
420nm CWL, 12.5mm Dia., Hard Coated OD 4 10nm Bandpass Filter	420 ± 2	10 ± 2	± 85%	104.5€	12.5 diameter/ 5
450nm CWL, 12.5mm Dia., Hard Coated OD 4 10nm Bandpass Filter	450 ± 2	10 ± 2	± 85%	104.5€	12.5 diameter/ 5
480nm CWL, 12.5mm Dia., Hard Coated OD 4 10nm Bandpass Filter	480 ± 2	10 ± 2	± 85%	104.5€	12.5 diameter/ 5
510nm CWL, 12.5mm Dia., Hard Coated OD 4 10nm Bandpass Filter	510 ± 2	10 ± 2	± 85%	104.5€	12.5 diameter/ 5
540nm CWL, 12.5mm Dia., Hard Coated OD 4 10nm Bandpass Filter	540 ± 2	10 ± 2	± 85%	104.5€	12.5 diameter/ 5
560nm CWL, 12.5mm Dia., Hard Coated OD 4 10nm Bandpass Filter	560 ± 2	10 ± 2	± 85%	104.5€	12.5 diameter/ 5

Edmund Optics reference	Transmittance peak (nm)	FWHM (nm)	Transmittance	Cost	Size / Thickness (mm)
580nm CWL, 12.5mm Dia., Hard Coated OD 4 10nm Bandpass Filter	580 ± 2	10 ± 2	± 85%	104.5€	12.5 diameter/ 5
600nm CWL, 12.5mm Dia., Hard Coated OD 4 10nm Bandpass Filter	600 ± 2	10 ± 2	± 85%	104.5€	12.5 diameter/ 5
620nm CWL, 12.5mm Dia., Hard Coated OD 4 10nm Bandpass Filter	620 ± 2	10 ± 2	± 85%	104.5€	12.5 diameter/ 5
650nm CWL, 12.5mm Dia., Hard Coated OD 4 10nm Bandpass Filter	650 ± 2	10 ± 2	± 85%	104.5€	12.5 diameter/ 5
700nm CWL, 12.5mm Dia., Hard Coated OD 4 10nm Bandpass Filter	700 ± 2	10 ± 2	± 85%	104.5€	12.5 diameter/ 5
750nm CWL, 12.5mm Dia., Hard Coated OD 4 10nm Bandpass Filter	750 ± 2	10 ± 2	± 85%	104.5€	12.5 diameter/ 5

Information available at (access date – April, 2015):

http://www.edmundoptics.eu/optics/optical-filters/bandpass-filters/hard-coated-od4-10nm-bandpass-filters/3159/?site=WE&countryid=177&_ga=1.134612337.1066078829.1432649204

Table II. 2 Commercial bandpass optical filters from *Thorlabs*.

Thorlabs reference	Transmittance peak (nm)	FWHM (nm)	Transmittance	Cost	Size / Thickness (mm)
FB350-10	350 ± 2	10 ± 2	25%(min) – 35% (max)	118.80€	25.4 diameter/ 6.3
FB370-10	370 ± 2	10 ± 2	±25%	118.80€	25.4 diameter/ 6.3
FB380-10	380 ± 2	10 ± 2	25% (min) – 30% (max)	118.80€	25.4 diameter/ 6.3
FB400-10	400 ± 2	10 ± 2	± 37%	109.80€	25.4 diameter/ 6.3
FB400-40	400 ± 8	40 ± 8	± 45%	99€	25.4 diameter/ 6.3
FBH400-40	400	40	90%	144€	25 diameter/ 3.5

Thorlabs reference	Transmittance peak (nm)	FWHM (nm)	Transmittance	Cost	Size / Thickness (mm)
FB420-10	420 ± 2	10 ± 2	± 45%	88.20€	25.4 diameter/ 6.3
FB450-10	450 ± 2	10 ± 2	45% (min) – 50% (max)	87.30€	25.4 diameter/ 6.3
FB450-40	450 ± 8	40 ± 8	45% (min) – 70% (max)	84.60 €	25.4 diameter/ 6.3
FB480-10	480 ± 2	10 ± 2	45% (min) – 55% (max)	82.80€	25.4 diameter/ 6.3
FB510-10	510 ± 2	10 ± 2	50% (min) – 60% (max)	78.06€	25.4 diameter/ 6.3
FB540-10	540 ± 2	10 ± 2	± 50%	76.20€	25.4 diameter/ 6.3
FB560-10	560 ± 2	10 ± 2	± 50%	76.20€	25.4 diameter/ 6.3
FB580-10	580 ± 2	10 ± 2	± 50%	76.20€	25.4 diameter/ 6.3
FB600-10	600 ± 2	10 ± 2	± 50%	76.20€	25.4 diameter/ 6.3
FB600-40	600 ± 8	40 ± 8	± 70%	88.71€	25.4 diameter/ 6.3
FB620-10	620 ± 2	10 ± 2	± 50%	76.20€	25.4 diameter/ 6.3
FB650-10	650 ± 2	10 ± 2	± 50%	76.20€	25.4 diameter/ 6.3
FB650-40	650 ± 8	40 ± 8	± 70%	88.71€	25.4 diameter/ 6.3
FBH650-40	650	40	90%	144€	25 diameter/ 3.5
FB700-10	700 ± 2	10 ± 2	± 65%	83.88€	25.4 diameter/ 6.3
FB700-40	700 ± 8	40 ± 8	± 75%	86.72€	25.4 diameter/ 6.3
FB750-10	750 ± 2	10 ± 2	± 60%	83.88€	25.4 diameter/ 6.3
FB750-40	750 ± 8	40 ± 8	± 80% (max)	86.72€	25.4 diameter/ 6.3

Information available at (access date – April, 2015):

https://www.thorlabs.com/newgrouppage9.cfm?objectgroup_id=1001&pn=FB350-10#5410

https://www.thorlabs.com/newgrouppage9.cfm?objectgroup_id=1860&pn=FBH405-10

Table II. 3 Commercial bandpass optical filters from *Newport*.

Newport reference	Transmittance peak (nm)	FWHM (nm)	Transmittance	Cost	Size / Thickness (mm)
10BPF10-350	350 ± 2	11 ± 2	± 30%	343€	25.4 diameter/ 7.62

Newport reference	Transmittance peak (nm)	FWHM (nm)	Transmittance	Cost	Size / Thickness (mm)
10BPF10-370	370 ± 2	12 ± 2	± 30%	343€	25.4 diameter/ 7.62
10BPF10-380	380 ± 2	12 ± 2	± 30%	333€	25.4 diameter/ 8.89
10BPF10-400	400 ± 2	10 ± 2	± 30%	129€	25.4 diameter/ 7.59
10BPF25-400	400 ± 3.5	25 ± 3.5	± 35%	161€	25.4 diameter/ 6.35
10BPF70-400	400 ± 10	70 ± 30	± 60%	109€	25.4 diameter/ 7.59
10BPF10-420	420 ± 2	10 ± 2	± 45%	148€	25.4 diameter/ 6.35
10BPF10-450	450 ± 2	10 ± 2	± 45%	129€	25.4 diameter/ 6.35
10BPF25-450	450 ± 3.5	25 ± 3.5	± 45%	161€	25.4 diameter/ 6.35
10BPF70-450	450 ± 10	70 ± 30	± 60%	109€	25.4 diameter/ 6.35
10BPF10-480	480 ± 2	10 ± 2	± 50%	113€	25.4 diameter/ 6.35
10BPF10-510	510 ± 2	10 ± 2	± 50%	109€	25.4 diameter/ 6.35
10BPF10-540	540 ± 2	10 ± 2	± 50%	109€	25.4 diameter/ 6.35
10BPF10-560	560 ± 2	10 ± 2	± 50%	109€	25.4 diameter/ 6.35
10BPF10-580	580 ± 2	10 ± 2	± 50%	109€	25.4 diameter/ 6.35
10BPF10-600	600 ± 2	10 ± 2	± 50%	109€	25.4 diameter/ 6.35
10BPF25-600	600 ± 3.5	25 ± 3.5	± 50%	141€	25.4 diameter/ 6.35
10BPF70-600	600 ± 10	70 ± 30	± 60%	109€	25.4 diameter/ 6.35
10BPF10-620	620 ± 2	10 ± 2	± 50%	109€	25.4 diameter/ 6.35
10BPF10-650	650 ± 2	10 ± 2	± 50%	109€	25.4 diameter/ 6.35
10BPF25-650	650 ± 3.5	25 ± 3.5	± 50%	141€	25.4 diameter/ 6.35
10BPF70-650	650 ± 10	70 ± 30	± 60%	109€	25.4 diameter/ 6.35
10BPF10-700	700 ± 2	12 ± 2	± 50%	120€	25.4 diameter/ 6.35
10BPF25-700	700 ± 3.5	25 ± 3.5	± 50%	141€	25.4 diameter/ 6.35
10BPF70-700	700 ± 10	70 ± 30	± 60%	109€	25.4 diameter/ 5.08
10BPF10-750	750 ± 2	13 ± 2	± 50%	120€	25.4 diameter/ 6.35

Newport reference	Transmittance peak (nm)	FWHM (nm)	Transmittance	Cost	Size / Thickness (mm)
10BPF25-750	750 ± 3.5	25 ± 3.5	± 50%	123€	25.4 diameter/ 6.35
10BPF70-750	750 ± 10	70 ± 30	± 60%	113€	25.4 diameter/ 6.35

Information available at (access date – April, 2015):

http://search.newport.com/i/1/q1/products/q2/Optical+Filters/x1/pageType/x2/section/q3/Bandpass+Filters/x2/section/x3/chapter/nav/1/

Appendix III – Commercial photodiode used for the characterization of the CMOS photodiodes

Hamamatsu S1336-5BQ responsivity:

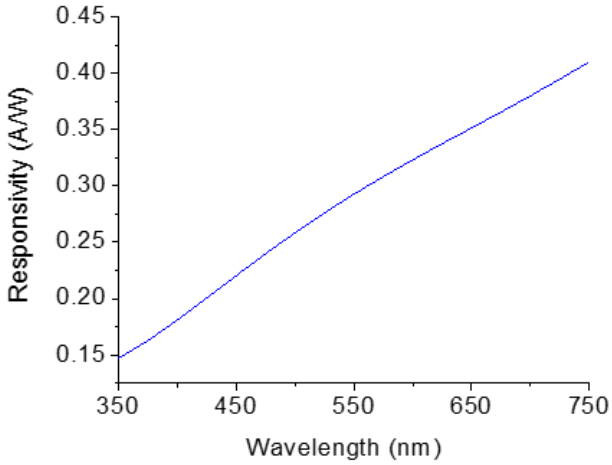

Figure III.1 Responsivity of the commercial photodiode *Hamamatsu S1336-5BQ* (data fitting at Excel using the spectral response curve presented at: www.hamamatsu.com/eu/en/product/category/3100/4001/4103/S1336-5BQ/index.html).

Appendix IV - Intensity curve of the light source used for the on-chip measurements

Normalized intensity curve:

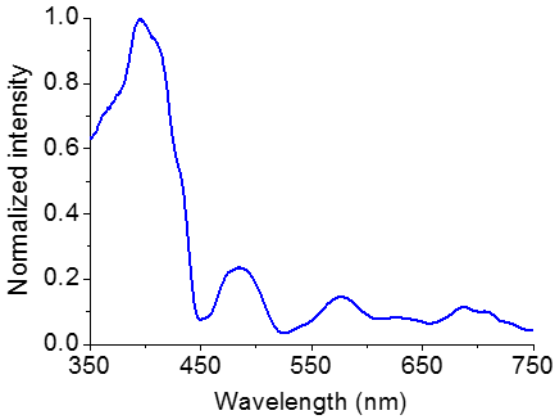

Figure IV.1 Normalized intensity curve of the light source used for the on-chip measurements.